Ultrashort laser pulse interaction with overdense plasmas

Inaugural-Dissertation

zur Erlangung des Doktorgrades
der Mathematisch-Naturwissenschaftichen Fakultät
der Heinrich-Heine-Universität Düsseldorf

vorgelegt von

Mirela Cerchez

aus Tecuci (RO)

Düsseldorf, Dezember 2008

Aus dem Institut für Laser- und Plasmaphysik
der Heinrich-Heine-Universität Düsseldorf

Gedruckt mit der Genehmigung der
Mathematisch-Naturwissenschaftlichen Fakultät der
Heinrich-Heine-Universität Düsseldorf

1. Gutachter: Prof. Dr. O. Willi

2. Gutachter: Prof. Dr. A. Pukhov

Tag der mündlichen Prüfung: 30.01.2009

Abstract

With the recent developments of intense, ultrashort laser pulses rapidly heated matter under extreme conditions can now be produced and investigated. These interaction processes are characterized by unique properties as the laser energy is absorbed on a femtosecond time scale before significant hydrodynamic expansion of the plasma can occur. Hence the laser energy is transferred to matter at densities close to solid. In this thesis, experimental studies concentrated on investigations of the physical properties of overdense plasmas characterized by steep density gradients. High-contrast, few-cycle laser pulses were focused onto solid target up to an average intensity of $\approx 5 \times 10^{16}\,\mathrm{W/cm^2}$. The fundamental process of the laser energy transfer was studied using laser absorption measurements and XUV plasma spectroscopy.

The experimental investigations of the laser energy absorption by solid targets represented an extensive study. Different physical parameters including laser intensity and polarization, incidence angle and target type (conductor or dielectric) were studied. The experimental results proved that the energy of these ultra-short laser pulses can be efficiently absorbed up to $\approx 77\%$ by a plasma characterized by a very steep profile. The level of absorption of the p-polarized laser pulses significantly exceeds the s-polarization absorption. The experimental results were compared with Particle-in-Cell simulations performed in *2-D* geometry. The simulation results indicate that the preponderance of the *p*- polarization absorption on *s*- polarization found in our experiments is of collisionless nature. A good agreement with the experiment was found for steep plasma profiles with a density scale length of $\approx 1\%$ of the laser wavelength.

Spectroscopic investigations of plasmas generated by ultrashort laser pulses on low Z massive and coated targets were performed. A high resolution spectrometer was built during this work in order to record the time-integrated K-shell emission. For the investigated materials (LiF, BN) specific effects of high density plasmas like series limit of the H-like ions and satellites lines were identified in the spectra. The lack of the higher series lines was explained by pressure ionization. Hydrodynamic simulations combined with atomic calculations reproduced the time integrated spectra and indicate that the plasma emission preponderantly originated from high densities close to solid in agreement with the absorption measurements.

Zusammenfassung

Durch jüngste Entwicklungen intensiver, ultrakurzer Laserpulse kann nun schnell erhitzte Materie unter extremen Bedingungen erzeugt und untersucht werden. Die zugrunde liegenden Interaktionsprozesse sind durch besondere Eigenschaften charakterisiert, da die Laserenergie auf einer Femtosekunden-Zeitskala absorbiert wird, bevor signifikant hydrodynamische Expansion des Plasmas auftreten kann. Demzufolge wird die Laserenergie auf Materie mit nahezu Festkörperdichte transferiert. In dieser Arbeit konzentrieren sich die experimentellen Studien auf die Erforschung der physikalischen Eigenschaften überdichter Plasmen, welche durch einen steilen Dichtegradienten charakterisiert sind. Hochkontrastige Laserpulse mit wenigen optischen Zyklen wurden auf Festkörpertargets fokussiert, was durchschnittliche Intensitäten von $\approx 5 \times 10^{16} W/cm^2$ erzielte. Die zugrunde liegenden Prozesse des Transfers der Laserenergie wurden über Laser-Absorptionsmessungen und XUV-Plasmaspektroskopie studiert.

Ausführliche experimentelle Untersuchungen der Laser-Energieabsorption von Festkörpertargets sind durchgeführt worden. Verschieden physikalische Parameter einschließlich der Laserintensität und Polarisation, dem Einfallswinkel und der Beschaffenheit des Targets (leitend bzw. dielektrisch) wurden untersucht. Die experimentellen Ergebnisse belegen, dass die Energie dieser ultrakurzen Laserpulse effizient bis zu $\approx 77\%$ von einem Plasma absorbiert werden kann, welches ein sehr steiles Profil aufweist. Der Grad der Absorption von p-polarisierten Laserpulsen übersteigt den der Absorption bei s-Polarisation dabei signifikant. Die Ergebnisse wurden mit Particle-in-Cell Simulationen verglichen, welche in einer 2-D-Geometrie durchgeführt wurden. Die Ergebnisse der Simulationen zeigen auf, dass das Überwiegen der Absorption bei p-Polarisation gegenüber der bei s-Polarisation, wie sie in den Experimenten beobachtet wurde, von kollisionsfreier Natur ist. Eine gute Übereinstimmung mit den Experimenten wurde für steile Plasmaprofile mit einer Dichte-Skalenlänge von $\approx 1\%$ der Laserwellenlänge gefunden.

Spektroskopische Untersuchungen von Plasmen, die unter Einfall ultrakurzer Laserpulse auf reine und beschichtete Nieder-Z-Targets generiert wurden, sind durchgeführt worden. Ein hochauflösendes Spektrometer wurde im Rahmen dieser Arbeit gebaut, um zeitintegrierte K-Schalen-Emission detektieren zu können. Für die untersuchten Materialien (LiF, BN) wurden spezifische Effekte von Plasmen hoher Dichte, wie die Liniengrenze wasserstoffartiger Ionen und Satelliten in den Spektren identifiziert. Das Fehlen von höheren Linien der Serie wurde durch Druckionisation erklärt. Hydrodynamische Simulationen in Kombination mit atomaren Berechnungen reproduzierten die zeitintegrierten Spektren und zeigen auf, dass die Plasmaemission überwiegend von hohen Dichten nahe der Festkörperdichte herrührt, was in Übereinstimmung mit den Absorptionsmessungen steht.

Contents

Chapter 1

Introduction

The subject of this thesis is the interaction of ultra-short, few-cycles laser pulses with solid matter. The work was aimed to produce and characterize dense plasmas and to investigate the laser energy transfer to matter found at densities close to the solid. The experimental investigations were performed in a new interaction regime benefiting from laser parameters of high contrast and very short pulse duration.

The physics of laser-matter interaction is one of the important topics of modern physics by the multiple opened research fields. Early after laser invention in 1960 [3], the interaction of the electromagnetic laser radiation with matter starts to exert a large interest for the understanding of the physical processes which accompany it. The interaction regime changed rapidly over the years with constantly increasing laser intensity. New opportunities for studying the high energy laser-plasma interaction regimes have been opened by the invention in 1985 of *chirped pulse amplification*(CPA) technique [117]. This revolutionary amplification method allows to generate ultrashort (femtosecond) laser pulses and to extract from the laser amplifier pulses with peak powers up to petawatt range [4]. In many laboratories worldwide, laser pulses delivered by CPA laser systems are focused within focal spots of few μm reaching, commonly, intensities in the range of $10^{16} - 10^{19}\,\mathrm{W/cm^2}$. Thus, the electric field strength of the laser radiation is comparable to or larger than the Coulombian field of the electrons in atoms ($E \geq 0.5\,\mathrm{TV/m}$). At these intensities, the laser pulses are able to ionize a material sample (gaseous or solid) and to transform it into plasma. The further interaction of the laser pulse with the heated matter induces a large variety of phenomena which depends on the laser intensity and the target. In a solid target irradiated by a laser pulse in a non-relativistic regime (electron quiver velocity is much smaller than the speed of light) processes like fast evaporation,

ablation, nonlinear ionization and absorption processes are expected [1].

Within the large variety of laser pulses parameters in terms of intensity and pulse duration, particularly interesting are the intense, ultrashort laser pulses operating in the few-cycles regime. The availability of femtosecond laser pulses opened opportunities for intens investigations of the rapidly heated matter in extreme conditions. In the center of these investigations it is found the fundamental process of the *laser energy transfer* to matter. These interactions are characterized by unique particularities as the laser energy is absorbed in a very short time scale before significant hydrodynamic plasma motion occurs and is deposited in the plasma at high densities, close to the solid matter. The mechanisms of the laser energy absorption by solid targets and its efficiency in certain interaction conditions are relevant for many research fields and applications such as fast ignition for inertial confinement fusion (ICF) [5], ultrafast x-ray generations and radiation sources [6] or highly energetic particle production [7]. The isochoric heating processes of plasmas at high densities ($n_e > 10^{22}\,\mathrm{cm}^{-3}$) is also interesting for astrophysics or material science investigating high-quality laser material processing [11, 12]. Laser produced plasmas are able to reproduce in certain conditions, at laboratory size, states similar to those found in stars interior [9]. Laser-plasma experiments and simulation codes have been designed for testing different astrophysical models regarding radiative and transport proprieties of high density plasma, compressed material equations of state or opacities effects of plasma radiation. Spectroscopic investigation of laboratory dense plasma allows to identify and analyze specific effects and spectral features like line shift, line profile, transitions of highly ionized ions, satellites lines (see for example [8, 36, 44, 48]).

An impressive amount of experimental investigations and theoretical studies have been reported and contribute consistently to a better understanding of the laser-matter interaction processes. A number of review papers (see e.g [1, 61, 84]) have addressed the subject and summarized the progresses of heating and energy transfer from the laser pulse to solid matter in particular. These processes are strongly dependent on the laser pulse intensities even at moderate intensities, up to $\sim 1\times10^{17}\,\mathrm{W/cm}^2$ and this dependence was proved experimentally [62, 108, 109, 136] and theoretically [89, 98]. Moreover, the structure of the laser pulse, namely the existence of pre- and postpulses and the contrast ratio to the peak pulse, can control the absorbed energy efficiency by the parameters of the preformed plasma. The scale length of the plasma interacting with the peak pulse plays a significant role

in the absorption efficiency by collisionless absorption mechanisms including *resonance absorption, vacuum heating* or different models of *skin effect*. In the presence of a large scale preplasma generated by long pulses, the resonance absorption of p-polarized laser beams is considered the most efficient collisionless process responsible for hot electron production with energies in the order of few tens of keV [138]. The shortening of the pulse duration and the recent transition from the picosecond and sub-picosecond regimes to few femtosecond pulses allow to deposit the pulse energy in shorter time scales. The availability of ultrashort laser pulses characterized by a good contrast, reduces significantly the expansion preformed plasma and the interaction time, and offers a very desired interaction regime where the laser pulse energy can be transfer basically to the matter close to solid density. A question asked over 10 years ago [87] "whether significant absorption is possible at all for intense, pedestal-free pulses on high-density step-like profiles" may get an answer benefiting of this new available interaction regime. Experimentally, efficient absorption, up to 70% was measured in steep preplasma profiles where the expansion represents only few percents of the laser wavelength [68, 108, 135]. Depending on the interaction conditions, theoretical approaches and computer simulations emphasize new energy transfer mechanisms for explaining the experimental results [72, 79, 93].

The experimental studies reported in this thesis are focused on investigating the physical properties of overdense plasmas and the mechanisms of the laser energy transfer to the close to solid density matter using laser absorption measurements and XUV spectroscopy. The CPA laser system available at ILPP Düsseldorf employed in these experiments delivered high-contrast, 8 fs laser pulses with an average intensity of $5 \times 10^{16}\,\mathrm{W/cm^2}$ onto the target. These particular laser parameters offer a novel interaction regime where the pulse energy is basically directly transferred to the matter at densities close to solid.

One of the main goals of the present work was to investigate some fundamental aspects regarding the energy laser coupling to the solid target. The first set of experimental investigations addresses the laser energy absorption by solid targets. The experimental results were compared with Particle-in-Cell simulations performed in 2-D geometry. A good agreement with the experiment was found for a steep plasma profile with 1% of the laser wavelength.

In the second part of this work, plasmas in an overdense state generated by ultrashort, 8 fs laser pulses were investigated using spectroscopic methods. For the

investigated materials (LiF, BN), XUV spectra show spectral characteristics specific to dense plasma states like series limit for the H-like ions and dielectronic satellites of the resonance lines. The spatial and temporal evolution of the plasma parameters was analyzed using hydrodynamic simulation and a collisional-radiative atomic code. The interaction of ultrashort laser pulses with coated targets leads to *isochoric heating* of the substrate layer and plasmas in high density state are generated. Matter in these extreme state is of particular interesting for astrophysics. Emission spectra of these targets were recorded and the energy penetration depth for some resonance lines was estimated.

The structure of this thesis is as follows:

- An introduction of the main physical parameters that describe the laser produced plasmas is given in the first section of the chapter 2. The effect of the laser prepulse in the interaction with a solid target is described and the plasma profile is defined. Further, the dynamics of the electrons, as main energy carriers, in the laser electric field is summarized.

- In the chapter 3 relevant physical processes which occurs during interaction of the laser pulse with the solid matter are reviewed. The surface of the target after being heated by the prepulse is of key importance for the main pulse interaction. The primary effects induced by the laser prepulse like vaporization, ablation and ionization depend on the laser pulse fluence and duration. Their main characteristics and validity domains are described. The collisional and collisionless absorption mechanisms relevant to non-relativistic laser-plasma interaction regime are discussed. The interaction regime of the present experiments is described and its novelty is emphasized in comparison to previous experimental conditions reported in the literature up to date. In the last section of this chapter, an overview of some important atomic processes and effects specific to dense plasmas is given and the validity of LTE in dense plasma is discussed.

- Chapter 4 presents the experimental arrangements used for measuring the absorbed laser energy fraction and for recording the XUV emission spectra. The experimental methods used in both cases are presented in detail. The experimental setup for the absorption measurements includes as main component an

integrating sphere and its technical performances are discussed. A high resolution spectrometer was built in order to record the time-integrated K shell emission spectra of low Z targets.

- In the chapter 5 the experimental results on the absorption measurements are presented. In order to interpret the data, PIC simulation have been performed employing the PSC code and the results have been compared with the experimental data. The energy transfer process from laser radiation to matter depends on a large number of physical parameters of both, laser and matter. Thus, in the experiments, the absorbed energy fraction was measured as a function of different parameters like: laser intensity and polarization (p and s), incidence angle and initial state of the target (conductive or dielectric). Finally, the experimental data and the simulation results are interpreted in the light of the absorption mechanisms relevant for the interaction regime of the experiments.

- Spectroscopic investigation results of dense plasmas created by ultrashort laser pulses are discussed in chapter 6. The experiments were performed using low Z materials and two types of targets: massive and coated targets. XUV emission spectra of low Z targets are analyzed and compared with the synthetic spectra provided by combined hydrodynamic-atomic codes simulations.

- In the chapter 7 the experimental and simulation results obtained during this work are summarized and an outlook for further investigations in fundamental research of dense plasmas is offered.

Chapter 2

Laser pulse interaction with solid matter

In the analysis of the laser-solid matter interaction, one has to consider a number of physical processes that occur into solid matter under the influence of the electromagnetic field of the laser pulse. The effect of the laser pulse on the solid surface depends strongly on its intensity. For low laser intensity, below the surface damage threshold, the electromagnetic field may induce reversible processes like phonons [115] or plasmons [76]. At high intensity regime, a more complex interaction picture is expected and the ionization processes become dominant. Consequently, a plasma can be created as an assembly of thermal particles with different ionization states. Additional processes like hydrodynamic expansion, heat or particles transport accompany the laser energy transfer and plasma creation. In the case of ultrashort, femtosecond laser pulses, the fast coupling of the laser field to the solid matter leads to rapid ionization of the surface within the first laser pulse cycles.

In this chapter, the main physical parameters which characterize the laser created plasma will be presented. Some of the nomenclature used in the next chapters will be defined. The effect of the laser pulse on the spatial distribution of plasma parameters, like electron temperature and density is analyzed by help of hydrodynamic simulation. In ultrashort laser pulse interactions, the electrons are the main energy carriers. Therefore, the dynamics of a free electron in the electromagnetic laser field will be discussed in the intensity range relevant for the present experiments.

2.1 Laser produced plasma - main physical parameters

A high intensity laser pulse incident onto cold, solid surface may lead to a fast transformation of the irradiated spot onto a dense, hot plasma. The laser pulse parameters play an important role in defining the plasma physical properties. Depending on the pulse intensity and rate of energy transfer, the ionization processes may occur, and a plasma with an *ionization degree* Z^* and an *electron density* $n_e = Z^* \cdot n_i$, will be created in front of the target which starts to expand hydrodynamically (here, n_i is the ion density). The velocity of the freely expanding plasma is approximated with the *ion sound velocity*,

$$c_{is} = \left(\frac{Z^* k_B T_e}{m_i}\right)^{1/2} \cong 1 \times 10^4 \cdot (T_e[eV])^{1/2} \cdot \left(\frac{Z^*}{A}\right)^{1/2} \quad [m/s] \tag{2.1}$$

where T_e is the electron temperature, m_i is the ion mass, A is the atomic and k_B is the Boltzmann constant. The expansion could result in large gradients of density and temperature, from dense and cold layers near to the target, up to rarefied and hot coronal region towards the vacuum or into the atmosphere where the expansion takes place. The electron density variation in the expansion direction (Oz) might be approximated with an exponential decay:

$$n_e(z) = n_{eo} exp\left(-\frac{z}{L}\right) \tag{2.2}$$

n_{eo} being the valence electron density in the solid target and L is the *scale length of the plasma* profile defined as:

$$L = |\nabla n_e(z)/n_{e0}|^{-1} \tag{2.3}$$

In the case of isothermal expansion of an exponential profile, the plasma scale length achieved during the laser pulse duration (τ_L) can be estimated using the formula [71]:

$$L = c_{is} \cdot \tau_L \cong (T_e[eV])^{1/2} \cdot \left(\frac{Z^*}{A}\right)^{1/2} \cdot \tau_L[fs] \quad [nm] \tag{2.4}$$

The propagation of the laser electromagnetic field of frequency ω_L through the plasma is described by the *dispersion relation* which can be derived in different

approximations accounting for the particular laser-plasma interaction conditions. Assuming the propagation of the laser pulse perpendicular to a cold, collisionless plasma, along the Oz axis, the dispersion relation reads [2]:

$$\omega_L^2 = \omega_p^2 + c^2 k^2 \tag{2.5}$$

where ω_p is the *plasma frequency*:

$$\omega_p = \left(\frac{e^2 n_e}{\varepsilon_0 m_e}\right)^{1/2} \cong 5.6 \times 10^4 \sqrt{n_e[cm^{-3}]} \quad [s^{-1}]. \tag{2.6}$$

The physical constants in the formula above are e - the electron charge, m_e - electron mass and ε_0 - the vacuum permittivity. Accordingly to the dispersion relation (2.5) in a profile characterized by an electron density distribution $n_e(z)$, the laser can propagate ($k > 0$) up to a density called *critical density* defined by the condition $\omega_L = \omega_p$ and given by the formula:

$$n_{cr} = \frac{\varepsilon_0 m_e}{e^2} \cdot \omega_L^2 \cong \frac{1.1 \times 10^{21}}{(\lambda_L[\mu m])^2} \quad [cm^{-3}] \tag{2.7}$$

where λ_L is the laser wavelength.

In a general approach, the temporal profile of the main laser pulse indicates the presence one or many pre- and postpulses. The more common kind of prepulse is *the amplified spontaneous emission* (ASE) having a typical duration of several nanoseconds. Thus, the incident main pulse does not interact with a cold solid target but rather with a preheated or even ionized plasma. Therefore, the state of the preplasma (characterized by mass density, temperature of electron/ions/neutrals/lattice, average charge, etc.) is of main importance due to influence on its further interaction process with the main pulse. The prepulse contrast ratio indicates the total amount of energy delivered to the solid target and the prepulse duration controls the expansion time of the preformed plasma prior to the main pulse.

In the following, the effect of the prepulse will be analyzed in terms of plasma parameters. Figure 2.1 shows schematically the regions of a preformed plasma as the effect of a long time scale laser pulse (picoseconds regime) onto a solid target. In the left hand side, one may see the significant plasma expansion regions and the electron density typical decay from the solid targets towards the vacuum. In right hand side, the simulation results of the *MULTI-fs* hydrodynamic code [140] of the spatial dis-

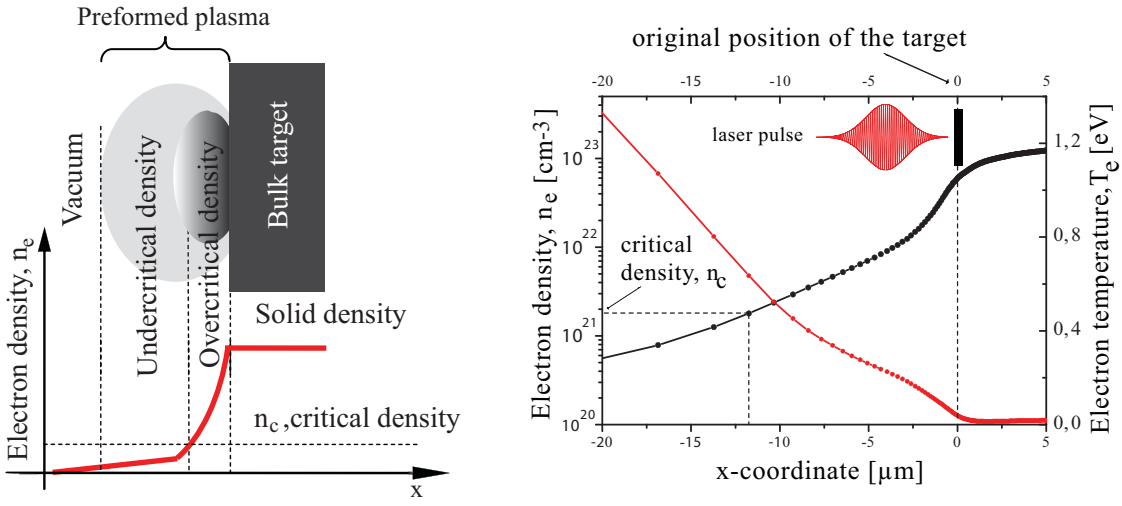

Figure 2.1: *Left*: Schematic representation of the preformed plasma as a prepulse effect onto a solid target. A typical spatial distribution of the electron density is attached. *Right*: The simulation results of 1-D hydrocode *MULTI-fs* indicating the spatial distribution of the electron density and electron temperature for an *Aluminum* plasma. The target was normally irradiated with 500 *ps* laser pulse, linearly polarized with peak intensity of $I \approx 1 \times 10^{11}\,\mathrm{W/cm^2}$.

tribution of the electron density and temperature in an *Aluminum* plasma expansion are shown (for the target geometry and simulation input parameters, see Appendix B.2). The laser pulse 500 ps in duration and 800 nm in wavelength was perpendicularly incident onto the target with a peak intensity of $I \approx 1 \times 10^{11}\,\mathrm{W/cm^2}$. The simulation results correspond to the laser peak and in the plot the expansion of the target layers in the vicinity of the original position of the cold target surface ($x = 0$) is shown. The plasma scale length determined from these simulations is about ~ 5 μm. At the critical surface, the electron density is $n_{cr} \approx 1.7 \times 10^{21}\,\mathrm{cm^{-3}}$ and the mass density is very low, $\rho_{cr} = 1\% \cdot \rho_{solid}$. Thus, plasmas generated by ns and ps laser prepulses at moderate intensities will be characterized by scale lengths in the order of microns. The example considered in this simulation corresponds to a contrast ratio of $\approx 10^5$ if the main pulse has an intensity of about $I_L \approx 1 \times 10^{16}\,\mathrm{W/cm^2}$. In this case, the main pulse, in the later interaction, will deposit its energy in low density matter, in the vicinity of the critical density which often corresponds to rarefied state of matter.

The effect of the prepulse is of crucial importance in the experiments reported in this thesis. In order to make possible the deposition of the laser energy onto

the dense layers of the targets and to investigate the direct interaction of the high intensity laser with the matter close to solid density, special conditions have to be considered. The steepening of the plasma profile can be controlled by the prepulse laser parameters. A high laser contrast associated with the ultrashort main pulse duration is one of the required conditions for achieving this interaction regime (refer to the paragraph 4.1.1). This novel regime will be analyzed in detail below, in paragraph 3.3.3.

2.2 Dynamics of a free electron in a non-relativistic laser field

In the interaction process of laser radiation with matter, the electrons are playing the most significant role, in general. They respond quickly to the laser electromagnetic field, are able to gain energy from the wave and to carry it further into matter. From classical electrodynamics is well known that the individual and the collective behavior of the electrons under the effect of laser electric and magnetic fields ($\vec{E}$, $\vec{B}$) govern or influence a large variety of laser-plasma physical processes like: energy absorption mechanisms and laser propagation through the matter [70, 71], optical [76, 162] and thermodynamic properties of matter [77] or atomic processes [32]. Considering the importance of the previously mentioned processes in connection with the topics addressed by this work, the present paragraph will summarize the main results of the electron motion in a laser field at non-relativistic intensities relevant to the interaction regime of the presented experiments.

Let us consider the motion of a free electron in a plasma under the influence of a monochromatic, plane, electromagnetic laser field which is described by its spatial- and time-dependent electric and magnetic fields components:

$$\vec{E}(\vec{r},t) = \vec{E}_0 \cdot \cos(\omega t - \vec{k}\cdot\vec{r}) \tag{2.8}$$

$$\vec{B}(\vec{r},t) = -\frac{1}{\omega}\cdot\nabla\times\vec{E}(\vec{r},t) = \vec{B}_0 \cdot \sin(\omega t - \vec{k}\cdot\vec{r}) \tag{2.9}$$

where ω is the angular laser frequency in the plasma and $\vec{k}$ is the propagation vector. Note that ω can be different from the laser angular frequency ω_L in vacuum according to the dispersion relation [71]. The motion of a free electron of mass m_e, velocity $\vec{v}_e$ and momentum $\vec{p}_e$, placed in this electromagnetic field, is governed by *Lorentz force*, $\vec{F} = -e\cdot(\vec{E} + \vec{v}_e \times \vec{B})$. According to the Newton's second law, the

equation of motion of the electron reads as:

$$\frac{d\vec{p}_e}{dt} = m_e \frac{d\vec{v}_e}{dt} = -e \cdot (\vec{E} + \vec{v}_e \times \vec{B}), \qquad \vec{v}_e = \frac{d\vec{r}}{dt} \tag{2.10}$$

For low and moderated laser intensities up to $\sim 10^{18}\,\mathrm{W/cm^2}$, the electron motion can be treated non-relativistically ($v_e \ll c$) and the magnetic term $\vec{v}_e \times \vec{B}$ can be neglected. Consequently, the equation 2.10 simplifies to:

$$\frac{d\vec{v}_e}{dt} = -\frac{e}{m_e} \cdot \vec{E}, \qquad \vec{v}_e = \frac{d\vec{r}}{dt} \tag{2.11}$$

Let us now consider the case of an electric laser field $\vec{E}(\vec{x}, t)$ linearly polarized along the Ox axis (Oz is the propagation axis, $\vec{k} = k\hat{z}$). Assuming that the initial electron velocity and position are $v_e(t = 0) = 0$ and $|\vec{x}(t = 0)| = 0$, the solutions of equation 2.11 reads as:

$$|\vec{v}_e| = v_q \sin(\omega t - k \cdot z), \qquad |\vec{x}_e| = x_q \cos(\omega t - k \cdot z) \tag{2.12}$$

where

$$v_q = \frac{eE_0}{m_e \omega}, \qquad x_q = \frac{eE_0}{m_e \omega^2}. \tag{2.13}$$

The *quiver velocity* v_q is the maximum velocity of the electron oscillation and the *quiver amplitude* x_q is the amplitude of the electron excursion in the laser field.

Commonly, the energy gained by the electron in the oscillatory motion is expressed in terms of the averaged kinetic energy over one laser cycle called the *ponderomotive potential*: $U_p =< \varepsilon_c >_T =< \frac{1}{2} m_e v_e^2 >_T$. The ponderomotive potential can be expressed in terms of the laser electric field E_0 or the laser intensity I_0 (see equation 4.3):

$$U_p = \frac{e^2}{4 m_e \omega^2} \cdot E_0^2 = \frac{e^2}{2 m_e c \varepsilon_0 \omega^2} \cdot I_0 \tag{2.14}$$

In practice, the laser electromagnetic wave is commonly described by its intensity and wavelength. Thus, the electric field strength amplitude and the laser frequency are given by:

$$E_0 = \left(\frac{2I_0}{\varepsilon_0 c}\right)^{(1/2)} \simeq 2.75 \times 10^{11} \cdot \sqrt{I_{16}} \quad [V/m] \tag{2.15}$$

$$\omega_L = \frac{2\pi c}{\lambda_L} \simeq \frac{1.88 \times 10^{15}}{\lambda_L[\mu m]} \quad [s^{-1}] \tag{2.16}$$

where I_{16} is the laser intensity in terms of $10^{16}\,\mathrm{W/cm^2}$. Accounting for these dependencies one may express in practical forms the ponderomotive potential, the quiver velocity and the quiver amplitude respectively, as follows:

$$U_p \approx 950 \cdot I_{16} \cdot (\lambda_L[\mu m])^2 \quad [eV] \tag{2.17}$$

$$\frac{v_q}{c} = 0.086 \cdot \sqrt{I_{16}} \cdot (\lambda_L[\mu m]) \tag{2.18}$$

$$x_q = 13.7 \cdot \sqrt{I_{16}} \cdot (\lambda_L[\mu m])^2 \quad [nm] \tag{2.19}$$

If the ponderomotive potential U_p becomes comparable to the rest energy of the electron, ($E_0 = m_e c^2 = 511\,\mathrm{keV}$), the relativistic approach of the electron motion should be considered. For laser radiation in the visible and near-infrared wavelength ranges, the relativistic regime for the electron starts at intensities larger than $\approx 10^{18}\,\mathrm{W/cm^2}$. In a plane wave of intensity of $I \approx 10^{16}\,\mathrm{W/cm^2}$ and wavelength $\lambda_L = 800\,\mathrm{nm}$, an electron has a ponderomotive potential of $U_p \approx 0.6\,\mathrm{keV}$. Within this approximation, the quiver velocity is $v_q \approx 0.07c$ and the quiver amplitude of the oscillatory motion is $x_q \approx 9\,\mathrm{nm}$. In steep plasma profiles, where the electric field has a component along the density gradient, for a scale length $L < x_q$, the electron can be pulled out from the plasma into the vacuum and then returned to the surface with the quiver velocity in about one cycle of the laser pulse. The laser energy can be absorbed in this process via so called *vacuum heating* (VH) absorption mechanism [79, 87].

The approximation of the plane wave is inappropriate for describing the electron dynamics in the electric field of a short, focused laser pulse. In this case, the laser intensity spatial distribution is characterized by strong radial gradients. The free electrons are undergoing oscillations in these gradients and the cycle average motion reveals the acceleration drift effect of a nonlinear force called *ponderomotive force*, F_p [2]. This force rises from the radial variation of the electric field and pushes the electrons on the transversal direction away from the laser axis towards to lower electric field region. Let us consider the non-relativistic motion of one electron in the linear polarized laser beam as considered above but now with a radial variation along the polarization direction for the amplitude ($E_0(y)$). One can solve the equation of motion 2.11 assuming the second-order approximation for velocity $v_y = v_{ey}^{(1)} + v_{ey}^{(2)}$, where $v_e^{(1)}$ is the solution of equation 2.11. For the electric field a Taylor expansion $E_y = E_0(y) \cdot \cos\varphi + y \cdot \partial E_0(y)/\partial y \cdot \cos\varphi + ...$ is considered, where $\varphi = \omega t - kz$ [112]. Cycle-averaging the electron dynamics one may identify the ponderomotive

force expression given by

$$F_P \equiv m_e \left\langle \frac{\partial v_{ey}^{(2)}}{\partial t} \right\rangle_T = -\frac{e^2}{4m_e\omega} \cdot \nabla E_0(y)^2 \quad \Rightarrow \quad F_P = -\nabla U_p \sim -\nabla I \tag{2.20}$$

and note that the ponderomotive force derives from the gradient of ponderomotive potential (equation 2.20). Moreover, the force occurs whenever the laser pulse presents spatial gradients. A similar ponderomotive force is expected to act on the ions but due to their inertia ($m_i \gg m_e$) the ponderomotive effects are negligible. The ponderomotive force density, defined as: $f_p = n_e F_p$ can be written as:

$$f_p = n_e F_p = -\frac{n_e m_e}{4} \nabla v_q^2 = -\nabla P_L \tag{2.21}$$

where P_L represents the *light pressure*. The ponderomotive force density may lead to a steepening of the electron density gradient around the critical density. The competition between the radiation pressure ($P_L = n_e m_e v_q^2/4$) and thermal pressure ($P_{th} = n_e K_B T_e$) may influence the energy transfer process from short laser pulse to the target. The ponderomotive pressure starts to exceed the thermal pressure (the quiver velocity becomes comparable with velocity of the thermal motion) at intensities $\gtrsim 10^{16}\,\mathrm{W/cm^2}$. The influence of the ponderomotive force in the absorption mechanisms of short (sub-picoseconds) laser pulses at moderate and high intensities ($\geq 10^{16}\,\mathrm{W/cm^2}$) has been investigated in different experiments and within different models [25, 26, 95]. In [25], the competition between the thermal and light pressures and their influence in the absorption processes using pump-probe Doppler shift measurements was analyzed. It was proved that a transition from sheath-inverse Bremsstrahlung (SIB)/anomalous skin effect (ASE) regime to the resonance absorption (RA)/vacuum heating (VH) is expected to occur when $P_L/P_{th} > 1$ (see also the paragraph 3.3).

Chapter 3

Physical processes in laser-overdense plasma interaction

During the laser-matter interaction, a large variety of phenomena occurs which lead to reciprocal transformations both of the matter physical properties and the laser propagation. In the case of solid targets, depending on the laser pulse parameters (energy, pulse duration, temporal profile) the laser induces on the front layers of the target processes like, *melting* and *surface evaporation*, *ablation* and *ionization*. Therefore, the matter modifies its physical parameters and influence the further interaction. Fundamentally, the physics of these processes bases on the transfer of the laser energy to the matter. In the case of expanded, underdense plasmas with a scale length $L/\lambda \geq 1$, the deposition of laser energy take place through electron collisions with the plasma constituents and by driving the plasma oscillations into the resonance with the laser field [63, 65, 82]. As soon as ultrashort, sub-picosecond lases pulses became available, experimental observations proved the steepening of the preplasma profile and indicated a deposition of laser energy in overdense regions of the solid target. New collisionless absorption mechanisms were proposed to explain the experimental observations.

As effect of laser radiation heating, dense, hot plasmas are created. At non-relativistic intensities ($I_L < 10^{18}\,\mathrm{W/cm^2}$), the temperature of the plasma is in the range of few hundreds of eV. At these temperatures, a great part of the atoms are found to be ionized. The emission spectra of plasmas may bring valuable information about the state of matter. In particular, specific effects of dense plasma are revealed by the experimental investigations in the field of plasma spectroscopy as *pressure ionization*, *continuum lowering*, *shift of the spectral lines* or *satellite lines*.

In this chapter, the physical processes specific to the laser-overdense plasma interaction interesting for this work will be discussed. In the interaction regime addressed by these experiments, the state of the target after the prepulse action and the overdense plasma parameters are of key importance. Consequently, the early interaction processes induced in general by the prepulse like solid heating, vaporization and ablation will be presented and the preplasma parameters will be estimated at the laser prepulse fluencies in the range of $0.5 - 2\,\mathrm{J/cm^2}$ in nanosecond and picosecond time scale, similar with the present experiment. In addition, the status of the absorption laser mechanisms will be summarized and discussed in the frame of high intensity ultrashort laser pulses interaction with overdense plasma. In the last paragraph, the atomic processes dominant in dense, collisional plasma will be presented in terms of characteristic rate coefficients. The specific effects of high density plasmas which can influence the radiation emission of these plasmas will be discussed together with statistical models for thermodynamic equilibrium in dense plasmas.

3.1 Solid surface heating, vaporization and ablation

The ultrashort, femtosecond laser pulses produced by the *CPA* technique are accompanied in general by pre-pulses with duration in the range of nanoseconds. The aim to deposit the main ultrashort laser pulse energy onto overdense plasma can be reached if the scale length L of the preformed plasma is very small, and/or the laser pulse propagates up to the dense region through unabsorbent vapour/rarefied plasma created by the prepulse effect and expanded in front of the target. The physical processes depend on the laser pulse parameters and on the thermo-physical properties of the targets. The laser ablation mechanisms were intensively investigated in the last decades over a large range of laser intensities, wavelengths (UV, visible and IR) and time scales, and different types of materials were studied [10, 11, 13, 17].

In principal, the laser prepulse interacts with cold matter with an abrupt profile. The primary *heating process* is determined by the optical properties of the target material and the absorption fraction can be determined employing the Fresnel equations 8.2. The spatial dependence of the laser electric field penetrating into a solid target is given by $E(z) = E(0)\exp(-z/l_s)$ and expresses the evanescently vanishing process into the overdense target known as *"normal skin effect"*. Here, $E(0)$ is the electric field strength at the vacuum-solid interface. The characteristic length of this

attenuation is the so-called *skin-depth* which, in the approximation of the overdense target, is given by [2]:

$$l_s \approx \frac{c}{\omega_p} \quad , \tag{3.1}$$

where c is the speed of light in vacuum and ω_p is the overdense plasma frequency (2.6). The spatial distribution of the absorbed energy flux [13] in the skin layer reads

$$Q_{abs}(z,t) = AI_0(t)\exp\left(-\frac{2z}{l_s}\right) \tag{3.2}$$

where I_0 is the incident laser intensity and $A = I/I_0 = 1 - R$ is the absorption coefficient given by the Fresnel formulas (8.2). The absorbed energy is further transferred into the target by the electrons through thermalization processes, energy transfer to the lattice and heat conduction. The thermalization processes take place via collisions and involve the electron and lattice subsystems characterized by the temperatures T_e and T_i, respectively. The energy transport into the solid is described by one-dimensional equation system within the so-called *"two-temperature diffusion model"* [15, 2]

$$C_e\frac{\partial T_e}{\partial t} = \frac{\partial}{\partial z}\left(k_e\frac{\partial T_e}{\partial z}\right) - \gamma(T_e - T_i) + S(z,t) \tag{3.3}$$

$$C_i\frac{\partial T_i}{\partial t} = \gamma(T_e - T_i) \tag{3.4}$$

$$S(z,t) = AI_0(t)\frac{2}{l_s}\exp\left(-\frac{2z}{l_s}\right) \tag{3.5}$$

where $C_{e,i}$ are the electron and lattice heat capacities per unit volume, γ is the electron-lattice coupling parameter, k_e is the electron thermal conductivity, while the laser source term is the energy deposition rate defined by $S(t) = \partial Q_{abs}(z,t)/\partial z$. For solving the equation system, an important approximation is offered by the relation between the specific time scale of the above mentioned processes of energy dissipation and the prepulse duration (nano-, pico- or femtosecond) which can define different interaction regimes. Three characteristic time scales can be defined: $\tau_e = C_e/\gamma$ is the electron cooling time, $\tau_i = C_i/\gamma$ is the lattice heating time and τ_L is the pulse duration. Note that $\tau_e \ll \tau_i$ for the temperature regime $T_e \ll T_F$, where T_F is the Fermi temperature [2] (e.g. for an *Aluminum* target $T_F = 11.7\,\mathrm{eV}$, $\tau_e \approx 100\,\mathrm{fs}$ and $\tau_i \approx 6\,\mathrm{ps}$).

In the following, the interaction regimes with short and long pulses will be discussed. The estimation of the target state and the induced effects as vaporization

and ablation surface after the prepulse heating phase is an important issue for the production of overdense plasmas. Accounting for the temporal profile of the laser pulse used in the present experiments (see figure 4.2) where the prepulses are in the range of pico- and nanoseconds, the most relevant case will be represented by the long pulses regime.

Short pulse regime

The low-fluence ablation process in the range of femtoseconds ($\tau_L \ll \tau_e \ll \tau_i$) and regimes ($\tau_e \ll \tau_L \ll \tau_i$) has been studied theoretically [13, 14] and experimentally [17, 19]. In a first approximation, for fast energy laser transfer, the thermal conduction into the target can be neglected in this case and the ablation process can be considered as a rapid solid-vapor transition [11, 15]. In a simplified scenario [13] regarding the evaporation onset, the ions are extracted from the target surface by the electric fields built in the separation charge created in front of the target. A strong vaporization starts when the ion energy ε_i overcomes the binding energy of ions in the lattice ε_b. Accounting for different sort of targets (conductors or insulators) one may determine the laser fluence threshold for the ablation of metals (m) and dielectrics (d)[13]:

$$F_{th}^{m} \approx \frac{3}{4}(\varepsilon_b + \varepsilon_w)\frac{l_s \cdot n_e}{A}; \qquad F_{th}^{d} \approx \frac{3}{4}(\varepsilon_b + J_i)\frac{l_s \cdot n_e}{A} \tag{3.6}$$

where n_e is the free electron density, ε_w is the work function and J_i is the first ionization potential. Note that at this short interaction time scale, the ablation threshold depends only on the target physical constants. This statement was experimentally proved for laser pulses of 800 nm wavelength, shorter than 100 fs and the inferred threshold value of $F_{th}^{m} \approx 0.5\,\mathrm{J/cm^2}$ for metals (Au, Ag, Al) and $F_{th}^{Si} \approx 2\,\mathrm{J/cm^2}$ for different sort of glasses [13, 16]. The threshold value depends weakly on the laser intensity and duration.

Long pulse regime

A different scenario is expected in the case of heating and ablation processes induced by longer laser prepulses on a pico- and nanoseconds time scale [13, 15, 17]. Depending on the laser fluence, the heated target spot may undergo melting, boiling or strong evaporation. One may determine the characteristic scaling laws of the energy density deposited onto the target surface U_{surf} and the threshold laser fluence

F_{th} for the evaporation. These quantities accounts for the target material constants and laser parameters and show a $\tau_L^{1/2}$ dependence:

$$U_{surf} = A\overline{I}\sqrt{\frac{\tau_L}{\alpha}} \tag{3.7}$$

$$F_{th} \approx \frac{\varepsilon_b n_a}{A} \cdot \sqrt{\alpha \tau_L} \tag{3.8}$$

where α is the target thermal diffusivity, $\overline{I}$ is the average intensity incident onto the target and n_a is the atomic density. In the table 3.1 the relevant physical constants of the materials investigated in the experiments reported in this thesis are listed. The threshold ablation fluence F_{th} is estimated from the equation 3.8.

Table 3.1: Physical constants at room temperature of different material targets investigated in the experiments and the corresponding ablation threshold fluence (equation 3.8). [13, 17, 20, 59]

Material	Atomic density $n_a[cm^{-3}]$	Binding energy $\varepsilon_b[eV]$	Absorption fraction, A	Thermal diffusity $\alpha[cm^2/s]$	Fluence ablation threshold $F_{th}[J/cm^2]$
Aluminum	6×10^{22}	3.05	0.15	0.5	$F_{th} \approx 0.14 \times (\tau_p[ps])^{1/2}$
Gold	5.9×10^{22}	3.37	0.05	1.3	$F_{th} \approx 0.72 \times (\tau_p[ps])^{1/2}$
BK7 Glass	$\sim 6 \times 10^{22}$	3.7	0.003	$\sim 5.5 \times 10^{-3}$	$F_{th} \approx 0.8 \times (\tau_p[ps])^{1/2}$
Boron nitride	5.3×10^{22}	~ 3	0.03	$\sim 8.5 \times 10^{-2}$	$F_{th} \approx 0.25 \times (\tau_p[ps])^{1/2}$
Lithium fluoride	6.1×10^{22}	~ 5	< 0.007	$\sim 2.7 \times 10^{-2}$	$F_{th} \approx 0.72 \times (\tau_p[ps])^{1/2}$

On a nanosecond time scale, the ablation threshold for these targets is in range of $5-100\,\mathrm{J/cm^2}$. For example, lets consider the case of an *Aluminium* target irradiated by a prepulse of duration $\tau_p = 5\,\mathrm{ns}$ and a fluence $F \approx 2\,\mathrm{J/cm^2}$, parameters similar with *ASE* laser prepulse characteristics used in the experiments (refer to paragraph 4.1.1). The fluence threshold is $F_{th}^{Al} \approx 10\,\mathrm{J/cm^2}$, which is above the laser prepulse fluence. In addition, the energy density deposited onto the target up to the laser peak is $U_{surf} \approx 10\,\mathrm{kJ/cm^3}$. The surface temperature is about $1000 - 1500\,\mathrm{K}$, value above the melting temperature and below the evaporation point. Consequently, these estimations indicate that one might expect locally heating/melting of the irradiated spot but not significant evaporation. The pulse duration is much longer ($\tau_L \gg \{\tau_{heat}, \tau_{e-i}\}$) than the characteristic times of the heat conduction τ_{heat} and electron-ion energy transfer τ_{e-i}, which are in the order of picoseconds. The electrons and the lattice reach the thermal equilibrium at the beginning of the laser pulse. For the transparent targets (*Glass*, *LiF*), the ablation threshold is approximatively

one order of magnitude larger due to the small absorption coefficient A of these materials. For the ns laser prepulse considered above, no evaporation is expected in the case of a glass target as the laser fluence is well below the target ablation threshold (estimated as $F_{th}^{BK7} \approx 60\,\mathrm{J/cm^2}$) and energy density accumulated onto the target is $U_{surf} \approx 10\,\mathrm{J/cm^3}$. In the experiment, a prepulse of fluence $F \approx 0.5\,\mathrm{J/cm^2}$ in the picoseconds time scale was measured. This fluence has the same order of magnitude with the ablation threshold for the investigated materials, calculated in the range of $0.1 - 1\,\mathrm{J/cm^2}$. Consequently, energy delivered by this prepulse on the skin layer of the target could be enough to overcome the atomic binding energy but the prepulse duration ($\approx 1ps$) is smaller than the heating time for the analyzed materials [13]. In this regime, the ions remain cold and a hydrodynamic expansion of target front layers can be neglected for all materials investigated.

3.2 Ionization processes in overdense plasmas

One of the main physical characteristic of the irradiated target that may influence the energy transfer efficiency from the laser pulse to the matter is the degree of ionization defined as $Z^* = n_e/n_i$, where n_e and n_i are the electron and ion densities, respectively. High intensity laser pulses are characterized by large peak values of the electric field (equation 2.15). At intensities in the order of $\sim 10^{16}\,\mathrm{W/cm^2}$, the laser electric field is strong enough to approach the Coulomb binding field of the electron on the first orbit in the hydrogen atom ($E_H = 5 \times 10^{11}\,\mathrm{V/m}$) [112]. Spatial and temporal distribution of the laser pulse electric field $\vec{E}(\vec{r}, t)$ leads to a corresponding variation of the ionization profiles, $n_e(\vec{r}, t)$. As direct consequence, the laser propagation is accompanied by temporal and spatial changes of the refractive index $n = \sqrt{1 - n_e/n_c}$ (n_c, plasma critical density) which are responsible for a number of specific phenomena like *ionization defocusing*, *spectral laser pulse blue shift* or, at relativistic intensities, *self focusing* of the laser pulse [2, 112]. With increased intensity of the laser pulse focused onto the target, different ionization mechanisms have been identified and investigated theoretically and experimentally (for a review, see [29, 30]).

As discussed in the previous paragraph, depending on the physical parameters, the effect of the prepulse may lead to a large variety of physical processes, from reversible heating, shock waves and no thermal damage of the surface up to evaporated and already partially ionized, long scale preplasmas. Regarding the dominant

ionization processes produced by the high intensity, main pulse, one has to distinguish between two process categories: (1) ionization caused by the laser electric field (dominant in gaseous targets and in rarefied preformed plasmas of the heated target) and (2) ionization due to the collision of the electrons with the lattice/ions for cold, solid/overdense plasmas. The ionization mechanisms in solid targets can be similar to those of gaseous targets if a vapor plume or underdense plasma lies in front of the solid target.

Photo-ionization and field ionization in intense laser fields

Under the laser field influence, the bound electrons will experience the combined field formed by the Coulombian atomic field and the laser field. In this context, the associated potentials are the ionization potential I_p and the ponderomotive potential U_p (equation 2.14). The laser field can induce a bound-free transition via different ionization processes [30]. An important scaling parameter introduced by Keldysh [24]

$$\gamma = \sqrt{\frac{I_p}{2U_p}} \tag{3.9}$$

separates between the regimes of photo-ionization and strong field ionization. For $\gamma \gg 1$, in low and moderate laser intensities, the photo-ionization processes are dominant, while in strong laser fields ($\gamma \ll 1$) ionization takes place via tunneling or over the barrier ionization. Further, will be summarized the relevant ionization processes induced by the laser field in underdense and in solid matter/overdense plasmas.

The photon energy of the laser pulses in the visible and near-infrared is in the order of a few eV (for $\lambda = 800\,\text{nm}$, $h\nu \simeq 1.54\,\text{eV}$), smaller than the first ionization potential value of most elements, and therefore, the photoelectric, single-photon ionization process is not possible. According to the perturbation theory, at high photon flux (as is available in the focused laser pulses) more than one photon is possible to be absorbed [30, 31]. The phenomenon is called *Multi-Photon Ionization (MPI)* [50] and can be synthetically described by the energy balance equation:

$$\varepsilon_{el}^{kin} = N \cdot \hbar\omega - I_p \tag{3.10}$$

where ε_{el}^{kin} is the kinetic energy of the released electron and N is the number of the absorbed photons of energy $\hbar\omega$. The electron is emitted with minimum kinetic

energy if the number of the absorbed photons is sufficiently large to outrun the ionization potential, $N = N_{min}$, where N_{min} is the minimum required number of photons for the *MPI* process, i.e to excite the electron from the bound level right above the ionization threshold. If there are more photons absorbed, $N > N_{min}$, the freed electron leaves the atom with an excess kinetic energy. The effect is known as *Above the Threshold Ionization (ATI)* [52] and was experimentally identified by the presence of multiple peaks in the emitted photoelectron spectrum, separated by the energy interval $\hbar\omega$.

With increased laser intensity, the perturbative regime is no longer valid and the ionization process is dominated by the laser field. In this case, the laser driver field is strong enough to distort the atomic binding potential and the outer shell electrons may escape from this combined potential via *Tunneling Ionization (TI)* [53] or *Over-the-Barrier Ionization (OBI)*. In the quasi-static approximation, where the laser oscillation cycle is larger than the electron orbit period, one may assume that the bound electron in an atom is experiencing an effective potential expressed by:

$$V(x) = -\frac{Ze^2}{x} - eEx \tag{3.11}$$

Here, E is the laser electric field assumed linearly polarized along the x-axis and Z is the charge of the ion that will be created. As a consequence, the Coulomb barrier is lowered and the electron can tunnel quantum mechanically this barrier into the continuum and the corresponding process is known as *Tunneling Ionization (TI)*. This process is characterized by a finite probability estimated by the ionization rates $\mathcal{R}_{TI}$, deduced by Keldysh [24] for H-like ions and is given by:

$$\mathcal{R}_{TI} = 4\omega_a \cdot \left(\frac{I_p}{\varepsilon_H}\right)^{5/2} \cdot \frac{E_a}{E(t)} \cdot exp\left[-\frac{2}{3}\left(\frac{I_p}{\varepsilon_H}\right)^{3/2} \cdot \frac{E_a}{E(t)}\right] \tag{3.12}$$

where ε_H is the ionization potential of the hydrogen atom (13.6 eV), $\omega_a = me^4/\hbar^3 \approx 4.1 \cdot 10^{16}$ Hz is the orbital frequency of the bound electron in the hydrogen atom, $E_a = e/4\pi\varepsilon_0 r_H^2$ is the electric field on the first orbit and r_H is the electron Bohr radius in the hydrogen atom. These ionization rates were further developed in the ADK-theory for complex atoms and ions by Ammosov, Delone and Krainov [54] and later on by Penetrante and Bardsley [29]. Their validity was confirmed by experimental investigation on gaseous targets (e.g. in [53], for 1-ps, 1-μm laser pulses with intensities of $10^{14} - 5 \times 10^{16}$ W/cm^2).

For higher laser intensities, the suppression of the barrier will be stronger and can fall below the ionization potential and the electrons can escape freely over the barrier (OBI). This process is characterized by a laser intensity threshold for onset, called *appearance intensity* I_{app}. This intensity corresponds to a critical laser electric field E_c able to compensate the Coulombian field and given by $E_c = I_p^2/4Ze^3$. Thus, the threshold intensity can be estimated as (compare the equation 4.3):

$$I_{app} = \frac{\varepsilon_0 c}{2} \cdot E_c^2 = \frac{c\pi^2\varepsilon_0^3}{2e^6} \cdot \frac{I_p^4}{Z^2} \approx 4 \times 10^9 \cdot \frac{I_p[eV]^4}{Z^2} \ \mathrm{W/cm^2} \tag{3.13}$$

For a hydrogen atom ($Z = 1$ and $I_p = 13.6\,\mathrm{eV}$), the appearance intensity is $I_{app}^H \approx 1.37 \times 10^{14}\,\mathrm{W/cm^2}$.

It is important to analyze the role of short and ultrashort pulse duration (τ_L) in connection with the contribution of the ionization processes discussed above, in strong laser field [30]. Accounting for the temporal distribution of the short laser pulse intensity $I_L(t)$, the early interaction with matter starts with low laser intensity where the perturbative regime dominates. At later interaction stages, the strong field regime of the ionization comes into play. For laser pulses on the *ps*-time scale at intensities in the range of $10^{14} - 10^{15}\,\mathrm{W/cm^2}$ (visible/near-infrared range), the *MPI* produces a significant ionization level before the laser peak interaction. Even for shorter pulses of $\tau_L = 100\,\mathrm{fs}$ the *MPI* still dominates at low intensity while around the laser peak an intermediate regime between *MPI* and *TI* is mentioned. In the few-cycle regime, of ultrashort laser pulses ($\tau_L = 10\,\mathrm{fs}$), the rapidly rising laser electric field makes the contributions of *MPI* negligible and the main ionization mechanism is the optical field ionization.

Collisional ionization (Electron impact ionization)

In higher density targets, the number of collisions between the particles is larger, which plays an important role in the ionization rates [32]. An energetic electron is hitting an atom or an ion and one of the bound electrons is released into continuum. This ionization effect called *Electron Impact Ionization* (EI) is one of the most important ionization process in dense plasmas and, in short, is expressed by the reaction: $A^\zeta + \vec{e} \Longrightarrow A^{\zeta+1} + e + e$, where by ζ and $\zeta + 1$ are denoted the ionization states of an atomic system A before and after the electron impact. The process is strongly depending on the parameters of the electron population (density n_e and velocity v_e) and its contribution can be estimated determining the ionization rates

of the process. In a general form, the ionization rate can be written as [55, 56]:

$$\mathcal{R}_{EI} = n_e \overline{v_e \sigma_i} \tag{3.14}$$

where,

$$\sigma_i = \alpha_i q_i \cdot \frac{ln(\varepsilon/I_p)}{\varepsilon I_p} \tag{3.15}$$

is the empirical Lotz ionization cross section, $\alpha_i = 2.17$ is an empirical parameter, q_i is the number of valence electrons of the ion involved in the collision, I_p is the ionization potential and $\varepsilon = m_e v_e^2/2$ is the electron kinetic energy. Both electron populations, thermal and laser accelerated, contribute at the impact ionization. Assuming a Maxwellian velocity distribution for the thermal electrons and a quiver velocity (equation 2.12) for the laser driven electrons, the corresponding ionization rates, $\mathcal{R}_{EI}^T$ and $\mathcal{R}_{EI}^L$ are given by [56, 163]:

$$\mathcal{R}_{EI}^T = 2\sqrt{2}\alpha_i q_i n_e \int_{I_p}^{\infty} \frac{ln(\varepsilon/I_p)}{\pi (kT_e)^{3/2} I_p} \exp(-\varepsilon/kT_e)\, d\varepsilon \tag{3.16}$$

$$\mathcal{R}_{EI}^L = \frac{n_e \alpha_i q_i}{\pi I_p \sqrt{U_p}} \int_{I_p}^{2U_p} \frac{ln(\varepsilon/I_p)}{\varepsilon I_p \sqrt{1 - \varepsilon/2U_p}}\, d\varepsilon \tag{3.17}$$

Here, U_p denotes the ponderomotive potential (equation 2.14). Both rates are dependent on the laser intensity via T_e and U_p, respectively and both, after reaching a maximum value, decrease while the laser intensity increases. For example, the ionization cross section for the thermal electrons, reaches its maximum at an electron temperature T_e of about 100 eV for most of the low-Z elements.

The ionization dynamics of solid target under the influence of short and high-intensity laser pulses can be summarized in the following physical scenario [57, 58]. In the early laser cycles, the dominant ionization process is the *strong field ionization SFI* (photon, multiphoton or tunneling ionization) which populates the conduction band with electrons. As soon as the density of the seed energetic electrons is high enough, the contribution of the impact ionization becomes significant and produces an ionization avalanche. An important parameter in the interplay of the ionization processes is the laser pulse duration. In [57], an analysis of characteristic times of the relevant ionization processes in SiO_2 is performed for a laser electric field of 1.5×10^{10} V/m. The rise time of the *SFI* is compared with the one for impact ionization within the different time duration. For pulses longer than 100 fs, the first 50 fs are dominated by *SFI* while the impact ionization starts to contribute later,

having a rise time larger than 50 fs. Therefore, in this analysis, for pulses shorter than 100 fs the contribution of the impact ionization is negligible. The empirical formulas of Lotz can be corrected accounting for some effects specific for solid/cold and high density plasmas [32]. Nevertheless, some corrections can be included in the estimations. For example, in these states, the electrons are degenerated and more accurately described by a Fermi-Dirac distribution. In addition, the ionization potential of the atomic systems in the high density state is lowered by the effect of the surrounding ions. In particular for the metals, due to the electronic reservoir electrons in the conduction band, the contribution of impact ionization is supposed to come into play earlier [59], as soon as the free electrons become energetic enough, i.e. ε is larger than I_p of the first bound electron.

3.3 Absorption of laser radiation by plasmas

Important progresses registered in the ultrashort, high intensity pulses generation open the possibility to investigate high density, hot plasmas in laboratory scale. The energy coupling to dense plasma becomes one of the main research topics due the important role played by the energy absorption efficiency in a large number of effects and application: highly energetic particles production, ignition methods for ICF, ultrafast radiation emission or isochoric heating. During the last decades, important theoretical and experimental progresses were registered on the route of understanding and modeling the absorption mechanisms of ps and sub-ps laser pulses at intensities between $10^{12}\,\mathrm{W/cm^2}$ and $10^{16}\,\mathrm{W/cm^2}$ [62, 65, 66, 67]. For these longer pulses and rather moderate intensities, collective, classical *resonance absorption* [70, 71] and the collisional *inverse bremsstrahlung* [71, 75] processes have been identified as main absorption mechanisms. In the frame of ultrashort, high intensity laser pulses interactions with overdense targets, a couple of new collisionless processes were found being responsible for the coupling of the laser pulse energy to the targets: *Brunel effect* [79], $\vec{j} \times \vec{B}$ heating [81], different *skin effects* [83, 93, 97] or *vacuum heating* [86]. In the new interaction regime addressed by the experiments reported in this thesis, when a few cycles high intensity pulses are focused onto close to solid density targets, high collisionless absorption has been experimentally observed. Besides the collisionless processes mentioned above, new models are suggested aiming to explain the physical mechanisms responsible for the fraction of high collisionless absorption [72].

The energy transfer process from the laser radiation to matter should obey to the Poynting's theorem [162] independently on the particular absorption mechanisms [71, 84]. The theorem is expressing the electromagnetic energy conservation and, in a general form, is given by:

$$\frac{\partial \mathcal{U}}{\partial t} + \nabla \cdot \vec{S} = -\vec{J} \cdot \vec{E}. \tag{3.18}$$

Here, $\mathcal{U} = (\varepsilon_0 \vec{E}^2 + \vec{B}^2/\mu_0)/2$ represents the energy density of the laser electromagnetic fields ($\vec{E}$, $\vec{B}$), $\vec{S}$ is the Poynting vector defined as $\vec{S} = c^2 \epsilon_0 \cdot \vec{E} \times \vec{B}$ and $\vec{J}$ is the electric current density. The rate of energy density is due to the energy flow expressed by the Poynting's vector divergence and due to the work done by the electromagnetic field onto matter. In steady-state conditions, averaging over the laser period T, the integral $\int_0^T \left(\varepsilon_0 E \cdot \frac{\partial E}{\partial t} + \frac{B}{\mu_0} \cdot \frac{\partial B}{\partial t} \right) dt = 0$ and theorem 3.18 reads:

$$\overline{\nabla \cdot \vec{S}} = \overline{\vec{J} \cdot \vec{E}} \tag{3.19}$$

If the electrons are moving freely in the electromagnetic field and their density is constant, the phase difference between $\vec{E}$ and $\vec{J}$ is $\varphi = \pi/2$ and consequently, no energy transfer from the laser to the matter takes place. The condition for a net absorption irrespective of the mechanism involved in the energy transfer derives from $\overline{\vec{J} \cdot \vec{E}} \neq 0$ namely, a dephasing $\varphi \neq \pi/2$ is required. This condition is fulfilled either (1) if collisional processes are present or (2) a resonance coupling of the electromagnetic field with the plasma waves takes place. A detailed analysis of this general characteristic of the absorption processes can be found in [84].

3.3.1 Collisional heating

Collisional heating is one of the fundamental physical process which leads to a net transfer of laser energy to matter by means of electrons who take energy from the laser and distribute it to the lattice/ions via collisions. The electrons are mobile and sensitive to the laser field acceleration so they are the main energy carriers in laser-matter interaction. Assuming that the electrons' motion in a hot plasma with heavy and immobile ions of density n_i is dominated by the Coulombian interaction then the *electron-ion collision frequency* is given by [71, 75]:

$$\nu_{ei} = \frac{4\sqrt{2\pi}}{3} \cdot \frac{\mathcal{Z} n_e e^4}{(4\pi\varepsilon_0)^2 \sqrt{m_e} (k_B T_e)^{3/2}} \cdot \ln\Lambda \simeq 2.9 \times 10^{-6} \cdot \frac{\mathcal{Z} n_e[cm^{-3}]}{T_e[eV]^{3/2}} \cdot \ln\Lambda \ \ [s^{-1}] \tag{3.20}$$

where $\mathcal{Z}$ is the ionization charge of the ions, n_e is the electron density ($n_e = \mathcal{Z}n_i$), T_e is the electron temperature. The factor $\ln\Lambda$ represents the Coulomb logarithm defined as $\ln\Lambda = \ln(b_{max}/b_{min})$ and results from the integration over the whole range of scattering angles [2, 71]. The distribution of the electrons' velocity is considered Maxwellian. The impact parameter b is defined by using characteristic lengths in the plasma and, in the classical approximation, $b_{max} = \lambda_D$ (*Debye length*) and $b_{min} = l_a$ (*interatomic distance*). In dense, cold plasmas, the large angle scattering can be more probable than the small angles one and the values of b_{min} and b_{max} become comparable. To avoid the unphysical result of a negative value for $\ln\Lambda$, a more precise value for the collisional cross-section is calculated according to quantum mechanics and the minimum value of the impact parameter is considered the *electron de Broglie wavelength* [2, 112].

The equation of motion of the electron fluid of density n_e in a high-frequency laser field ($\vec{E}e^{-i\omega_L t}$) in the presence of collisions reads as :

$$m_e\frac{\partial\vec{u}_e}{\partial t} = -e\cdot(\vec{E}+\vec{u}_e\times\vec{B}) - m_e\nu_{ei}\vec{u_e}, \tag{3.21}$$

where $\vec{u}_e$ represents the velocity of the electron fluid. Consequently, accounting for the harmonic variation of the fields, one may determine the plasma current density, $\vec{J}$ as follows:

$$\vec{J} = -n_e e\vec{u}_e = i\varepsilon_0\frac{\omega_p^2}{\omega_L + i\nu_{ei}}\cdot\vec{E}. \tag{3.22}$$

where ω_L and ω_p are the laser frequency and, respectively, the plasma frequency (2.6). Accounting for Ohm's law, $\vec{J} = \sigma\vec{E}$, the plasma complex conductivity reads as:

$$\sigma = i\varepsilon_0\frac{\omega_p^2}{\omega_L + i\nu_{ei}} \tag{3.23}$$

The propagation of the laser electromagnetic field through the plasma is described by the Helmholtz wave equations:

$$\nabla^2\vec{E} - \frac{1}{c^2}\cdot\frac{\partial^2\vec{E}}{\partial t^2} = \mu_0\cdot\frac{\partial\vec{J}}{\partial t} + \nabla(\nabla\cdot\vec{E}) \tag{3.24}$$

$$\nabla^2\vec{B} - \frac{1}{c^2}\cdot\frac{\partial^2\vec{B}}{\partial t^2} = \mu_0\cdot\nabla\times\vec{J} \tag{3.25}$$

Solving the wave equation for an electromagnetic, planar wave propagating though a plasma of conductivity σ (equation 3.23) one gets the linear *dispersion relation* with collisions as:

$$k^2 = \frac{\omega_L^2}{c^2}\left[1 - \frac{\omega_p^2}{w_L^2(1 + i\nu_{ei}^*)}\right] \tag{3.26}$$

Accounting for the identity $\varepsilon \equiv k^2c^2/\omega_L^2$, the complex reflective index of the plasma in the collisional approximation is given by: $\widetilde{n}^2 \equiv \varepsilon = 1 - \omega_p^2/[\omega^2(1 + i\nu_{ei}^*)]$ (compare with 8.5). Here $\nu_{ei}^* = \nu_{ei}/\omega_L$ is the normalized collision frequency. In the case of a sharp vacuum-homogeneous plasma interface ($L/\lambda = 0$), the fraction of the reflected energy can be determined by Fresnel equations (see Appendix A) [62, 112]. This simple model is satisfactory reproducing the experimental observations of absorption processes of the laser pulses at low intensity ($I_L \lesssim \times 10^{14}\,\mathrm{W/cm^2}$) [63, 68]. At higher intensities, the electron quiver energy becomes comparable to the thermal energy and consequently, the collisions are less efficient (see below).

A more general approach is required when the vacuum-matter interface is not a step function but represents an expanded profile with a spatial and temporal variation of the electron density. In a simplified picture, one can consider a 1D spatial gradient of the electron density, n_e, described by a scale length of $L = |\nabla n_e(z)/n_{e0}|^{-1}$ which corresponds to a local distribution of the collision frequency ν_{ei}. Consequently, the complex refractive index $\widetilde{n}^2(z)$ becomes a local parameter. The absorption coefficient of laser radiation with an incident intensity I_{in} ($\sim E^2$) due the collisions contribution, is defined as [2]:

$$f_c = \frac{I_{in} - I_{out}}{I_{in}} = 1 - exp\left(1 - \int_0^L 2Im \mid k \mid dz\right) \tag{3.27}$$

In order to estimate the absorption fraction, one has to solve numerically the Helmholtz wave equations (equations 3.24) accounting for a particular plasma profile [62, 112]. The interaction geometry is shown schematically in figure 3.3. For an electric field incident under an angle θ, in s-polarization geometry $\vec{E} = (E_x, 0, 0)e^{iky\sin\theta}$ the wave equation reads as:

$$\frac{\partial^2 E_x}{\partial x^2} + k^2(\varepsilon - sin^2\theta)E_x = 0 \tag{3.28}$$

and in p-polarization geometry where the components of electric and magnetic fields are $\vec{E} = (0, E_y, E_z)$ and $\vec{B} = (B_x, 0, 0)e^{iky\sin\theta}$, the wave equation reduces to:

$$\frac{\partial^2 B_x}{\partial x^2} - \frac{1}{\varepsilon}\frac{\partial \varepsilon}{\partial z}\frac{\partial B_x}{\partial z} + k^2(\varepsilon - sin^2\theta)B_x = 0 \tag{3.29}$$

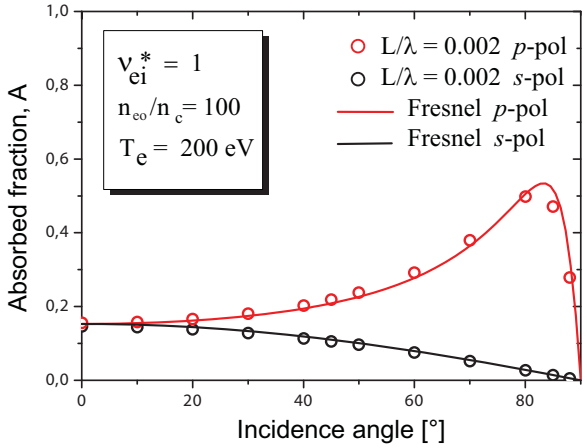

Figure 3.1: Comparison between the angular dependence of the absorbed fraction for p- and s- polarized laser beam calculated using the Helmholtz equations (open symbols) and Fresnel equations (solid line). The wave equation was solved for a target of profile $L/\lambda = 0.002$

For a long, slowly varying plasma profile $kL \gg 1$ these equations are solved using *Wentzel-Kramers-Brillouin (WKB)* approximation [70, 71]. The absorption coefficient obtained within this approximation depends on the particular plasma profile considered. For example, for laser pulse obliquely incident onto an exponential plasma profile (see equation 2.2), the absorbed laser energy fraction with collisional contribution is given by:

$$A_{coll} = 1 - exp\left(-\frac{8\nu_{ei}(n_{cr})}{3c} L \cos^3\theta\right) \tag{3.30}$$

where $\nu_{ei}(n_{cr})$ is the electron-ion collision frequency at the plasma critical density (see equation 2.7). In the s-polarization geometry, the component $k_y = k\sin\theta$ of the wavevector is perpendicular onto the density gradient $\nabla n_e(z)$ and constant during the laser propagation (compare to the dispersion relation 3.26). The parallel component k_z vanishes at the point $\varepsilon(z) = \sin^2\theta$ and defines the reflection plane of the laser radiation. The coordinate of the turning point corresponds to $n_e = n_{cr} \cdot \cos^2\theta$. For p-polarized light, the solution of the wave equation for long plasma profile shows, in addition, a resonant behavior of the absorption process (see paragraph 3.3.2).

In the case of interactions of the high intensity, ultrashort laser pulses a much steeper plasma profile $L/\lambda \ll 1$ is expected and the *WKB* approximation is not valid. For solving the wave equations in steep plasma gradients we used the *Wave-Solver (HS)* code developed by P. Gibbon [112] which is available as an open source [78]. The code calculations return the numerical solution of 1-D steady-state Helmholtz equations for both polarization geometry and for a particular plasma profile. When the plasma scale length becomes very small ($L/\lambda = 0.002$), the calculation results of the absorption fraction are similar to those obtained using Fresnel equations as

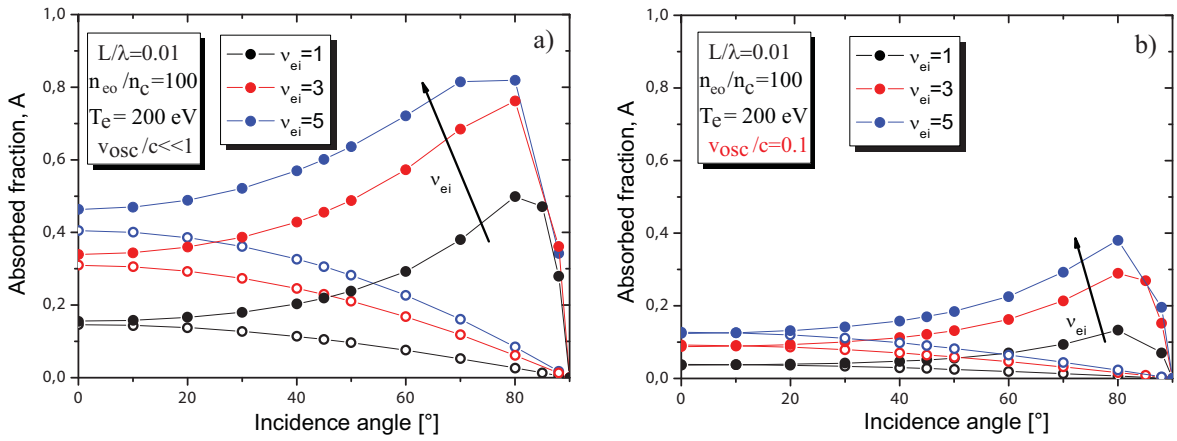

Figure 3.2: The effect of the electron-ion collision frequency value on the angular dependence of the absorbed energy fraction calculated in two approximations: *a)* the electron energy is dominantly thermal ($kT_e = 200\,\mathrm{eV}$) and *b)* accounting in addition for the electron quiver energy in an electric field of $E \sim 3 \times 10^{11}\,\mathrm{V/m}$. An exponential plasma profile was considered. The results for *p*-polarization and *s*-polarization cases are shown with open and filled symbols, respectively.

shown in figure 3.1. Both calculations have been performed with the same relevant collisional parameters of an overdense target ($\omega_p^2/\omega_L^2 = n_{e0}/n_{cr} = 100$ for a laser wavelength $\lambda_L = 800\,\mathrm{nm}$) and a normalized collision frequency $\nu_{ei}^* = 1$. Only the electron thermal energy was taken into account and consequently, the results are relevant for the low intensity regime. At higher intensities ($I > 10^{15}\,\mathrm{W/cm^2}$), the quiver velocity v_q (equation 2.13) becomes comparable to the thermal velocity $v_{th} = \sqrt{kT_e/m_e}$. An effective temperature $T_{eff} \propto v_q^2 + v_{th}^2$ can be defined which accounts for the total energy of the electron, thermal and oscillatory [2, 61]. Thus, the collision frequency scales as $\nu_{ei} \propto T_{eff}^{-3/2} \propto \left[T_e \cdot (1 + v_q^2/v_{th}^2)\right]^{-3/2}$. The effect of the quiver motion of electrons in high intensity fields on the efficiency of the collisional absorption is shown in figure 3.2. The angular dependence of the absorption coefficient of a low intensity laser pulse ($v_q/c \ll 1$) by an overdense plasma with an exponential, steep profile ($L/\lambda = 0.02$) is shown in figure 3.2 a). Different collision frequency have been considered in the calculations. For a certain geometry (polarization and incidence angle), the absorption fraction increases while the collision frequency becomes larger. Similar calculations were performed accounting in addition for the electron quiver energy and the results are shown in figure 3.2 *b)*. The total electron energy includes the electron quiver energy in a laser field of

intensity $I = 2 \times 10^{16}\,\mathrm{W/cm^2}$ (which corresponds to $v_q/c \approx 0.1$) and the thermal energy ($kT_e = 200\,\mathrm{eV}$). The absorption fraction decreases significantly to $\sim 50\%$. Moreover, another effect that has to be considered in the high-intensity regime is the anisotropy induced by the laser electric field in the electron energy distribution function [113]. The calculation including a non-Maxwellian contribution in the electron velocity distribution reveals a decrease by a factor of two (*Langdon factor*) of the collisional absorption coefficient. The strongest deviation from the Maxwellian distribution is expected to take place within the skin-layer and is characterized by time scales in the order of tens of femtoseconds [114].

3.3.2 Collisionless absorption

As previously shown, with increased laser intensities ($I > 10^{15}\,\mathrm{W/cm^2}$), the collisions become less effective and the collisional absorption model alone fails to explain the level of absorbed laser energy experimentally observed [106, 107, 108, 109, 111]. At these intensities the energy transfer from the laser to matter becomes dominated by the collective effects and was explained by a number of absorption models.

Resonance absorption

When a linearly, p-polarized laser wave is obliquely incident under an angle θ at an inhomogeneous plasma sheath, the electric field has a component parallel with the plasma gradient (i.e. $\vec{E} \cdot \nabla n_e \neq 0$) (see figure 3.3) and induces oscillations of the electrons along this direction. Accordingly to the wave equation 3.29, the electromagnetic wave will propagates up to the plane corresponding to $\varepsilon(z) = \sin^2\theta$ (equivalent with $n_e = n_{cr} \cdot \cos^2\theta$) and is partially reflected. This condition corresponds to the singularity in the second term of the wave equation (3.29), in the limit of low collisional plasmas ($\nu_{ei} \to 0$). The remainder of the wave will tunnel up to the critical surface $n_e = n_{cr}$ where the field frequency matches the plasma frequency. At this point, the laser field drives resonantly oscillations of the plasma electrons and leads to an irreversible conversion of laser energy to electrostatic waves. Thus, an efficient coupling between the laser electromagnetic wave and electron plasma wave occurs and this collective, non-collisional absorption process is called *resonance absorption* [69, 70]. The excited electrostatic plasma waves undergo Landau damping processes. Hereby the waves' energy is transferred to the electrons which transport it into the the denser target layers via collisional process. The integration of the wave equation accounts for the particular profile of the plasma (via plasma permittivity $\varepsilon(z)$)

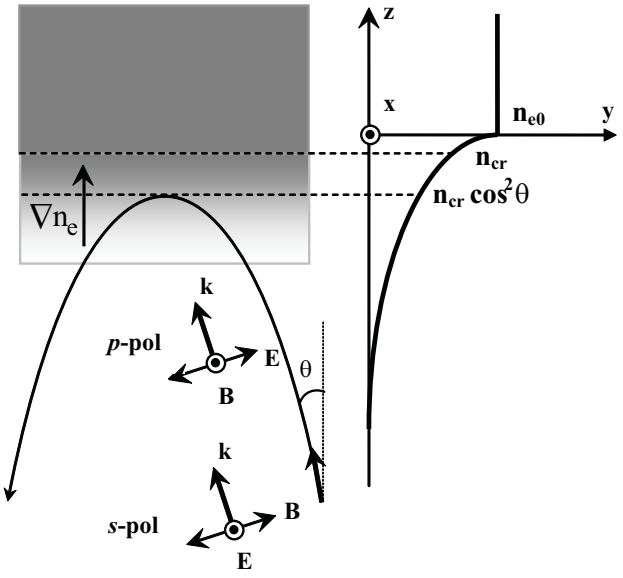

Figure 3.3: The geometry of the incident electromagnetic laser field for p- and s- polarized radiation onto a rarefied exponential plasma profile. The incident plane is Oyz.

and angular geometry and thus, the driver resonance field can be calculated [81]. In particular, in the limit of the *WKB* approximation (valid for profiles $kL \gg 1$), for a linear density profile, the absorption fraction is $f_{RA} \approx \phi^2(\tau)/2$. The function ϕ reads as: $\phi(\tau) \approx 2.3\tau \exp(-2\tau^3/3)$, where the parameter $\tau = (kL)^{1/3} \sin\theta$. The main particularities of the angular absorption behavior can be summarized as follows: (i) at angles close to normal incidence ($\tau \to 0$), the laser field has no component along the plasma gradient and no resonant energy transfer takes place; (ii) at grazing incidence, the parallel component of the laser field has to tunnel though a longer distance up to the critical point and the driver field becomes very small; (iii) the optimum absorption (estimated as 0.5) occurs at an intermediate angle $\theta_{opt} = \arcsin[0.8(kL)^{-1/3}]$, value which scales with the plasma profile, L; in steeper plasma profiles the optimum angle is shifted towards higher incidence angle. Numerical integration of the wave equation, performed by Landen [63] infers the optimum angle of the absorption fraction about 60% in the low collisional regime and long density profile ($\nu_{ei} \to 0$, $kL \gg 1$). These results regarding the angular profile of the absorption profiles are confirmed by *PIC* simulations performed in similar conditions.

In the case of a collisional plasma (for finite values of ν_{ei}) the absorption fraction decreases as the profile becomes larger due to the laser pulse depletion via collisions while propagating through the underdense plasma up to the turning point. In figure 3.4 the spatial distribution of the laser electric field and the electron density from *PIC* simulation results of the resonance absorption process are shown. An enhance-

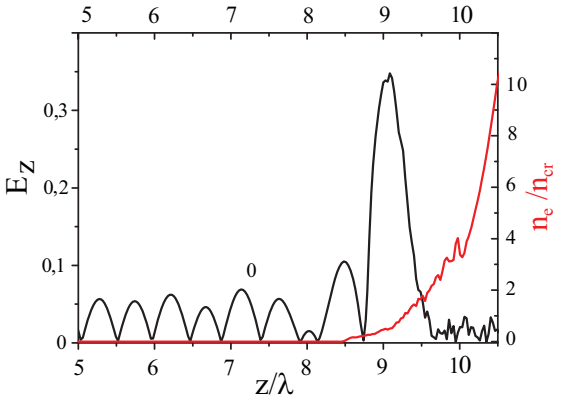

Figure 3.4: 2-D *PIC* simulation results of the resonance absorption process: the laser electric field and the density profile along the laser propagation axis, at the laser maximum intensity onto the target (simulation parameters: $\theta = 30°$, $I = 2 \times 10^{16}\,\mathrm{W/cm^2}$, $kL = 4$ and $\tau_L = 50\,\mathrm{fs}$).

ment of the electric field at the critical density by a factor of ≈ 6 was calculated. In the simulations, a laser pulse of intensity $I = 2 \times 10^{16}\,\mathrm{W/cm^2}$ and 50 fs (FWHM) duration was incident under 30° onto a long plasma profile ($kL = 4$). Details regarding the simulation set-up are presented in the Appendix B.2.

Analytical [71] and numerical [63] calculations prove the existence of an asymptotic limit for the validity of the linear resonance absorption described above. In very steep plasma gradients ($kL \ll 0.5$), the model for the linear resonance absorption process is not valid. In such profiles, where the scale length represents a few percent of the laser wavelength, the plasma is mainly overdense ($\omega_p > \omega_L$) and highly collisional. Therefore, a resonance coupling in the linear regime described above cannot occur as long as the resonance width ($\propto \nu^*_{ei}$) becomes finite and larger than the plasma profile [71, 135].

Recently, an important progress in the understanding of the efficient deposition of the laser pulse energy into the dense matter was achieved by the proposal of a alternative model for collisionless absorption in overdense target called *anharmonic resonance absorption* [72]. The new model aims to describe the collisionless absorption process of high intensity laser pulses by overdense plasmas ($\omega_p > \omega_L$) and extend the concept of the resonant coupling of the laser to the plasma beyond the linear regime. The absorption mechanism is effective when the laser intensity is high enough to induce nonlinear effects onto the plasma oscillations.

The absorption process can be described in a simplified picture assuming a plane wave electric field linearly p- polarized of frequency ω_L obliquely incident onto an overdense, cold and fully ionized target [72]. The plasma is characterized by an equal electron n_{e0} and ion density n_{i0} and by its frequency, ω_{p0}. The interaction region is divided into a high number of plasma layers of thickness d, oriented parallel to

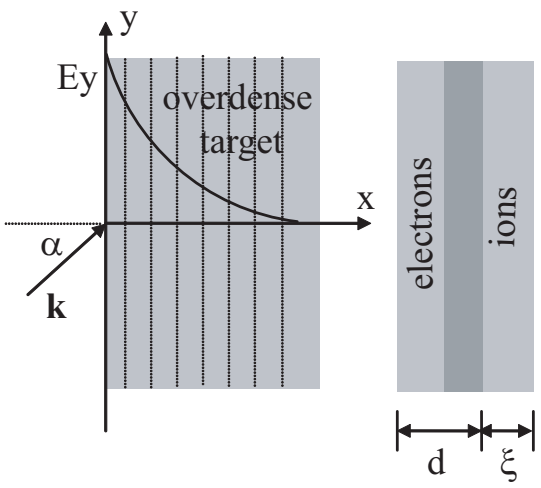

Figure 3.5: The geometry of laser-target interaction region in the *anharmonic resonance* model. The overdense target is cut in oscillating layers which are driven into resonance by a *p*-polarized laser field.

the surface (figure 3.5). In each layer of thickness d, the electrons are oscillating with the eigenfrequency ω_0 against the Coulombian attraction of the ions assumed immobile. The oscillation displacement is denoted by ξ and the amplitude by ξ_0. In the linear regime, of small displacement ($\xi \ll d$) corresponding to a weak electric field influence, the electron fluid oscillates in an well-known manner and their eigenfrequency represents the plasma frequency ($\omega_0 = \omega_{p0}$) in the overdense state. With the increased electric field, the oscillator is driven into the nonlinear regime and the restoring Coulombian force becomes weaker. In this regime, the eigenfrequency of the oscillating layer shows a dependence on amplitude given by the formula:

$$\omega_o = \frac{\pi}{4}\omega_{po}\sqrt{\frac{d}{\xi_0}}, \tag{3.31}$$

Under the influence of a strong laser field, the increased amplitude oscillations lead to a smaller eigenfrequency and the resonance occurs when the equality $\omega_o = \omega_L$ is fulfilled. The net energy transfer is irreversible due to a phase shift of π between the electron oscillations and the laser field and consequently, the cycle-average product $\vec{j} \cdot \vec{E} \neq 0$ (refer to equation 3.19 and to the analysis in the introduction of this paragraph). Within the theoretical model of the *anharmonic resonance absorption* an electric field threshold for the process onset was predicted. For one oscillator this field reads as:

$$E = m_e\omega_{po}^2 d/(4e), \tag{3.32}$$

where e and m_e are the electron charge and mass, respectively. Not such a simple scenario is expected in the analysis of multi-layer oscillations and their reciprocal

interaction. Although an analytic form of the main physical parameters accessible experimentally are not available, the *PIC* code simulations indicate the resonance coupling of the laser to the overdense plasma.

Brunel mechanism (*vacuum heating*)

The model proposed by Brunel in 1987 [79] anticipated a possible explanation of the laser absorption process in abrupt density gradients, as a complementary process to the resonance absorption. The *Brunel mechanism* is valid for high intensity laser pulses which interact with a steep plasma interface with a scale length L smaller than the quiver electron amplitude ($L < x_q = eE_0/m_e\omega^2$). The thermal electrons undergo oscillations in the laser electric field and, within a laser cycle, they can be dragged out of the target into the vacuum, turned around and return into the plasma at the quiver velocity v_q (equation 2.13). While the electric field is able to penetrate the overdense plasma only over the skin layer with a thickness l_s (equation 3.1), the electrons can travel deeper into the matter and depose collisionally their energy.

In a simple physical scenario based on the *capacitor approximation* one may consider an intense, p-polarized laser pulse of electric field $E = E_L \sin\omega t$ which is obliquely incident on a mirror-flat solid-vacuum interface. In the approximation of small absorption and in low laser intensity regime, the perpendicular component of the incident and reflected field leads to a driver field in front of the target of amplitude $E_d = 2E_L \sin\theta$, where θ is the incidence angle. The laser energy fraction irreversibly absorbed by the returned electrons is given by [79]:

$$A_B = \frac{\eta}{2\pi} \cdot \frac{v_d^3}{v_q^2 c \cos\theta} \tag{3.33}$$

where η is an efficiency factor which measure the fraction of the oscillatory energy converted in the plasma heating and $v_d = eE_d/m_e\omega$. Brunel estimated initially $\eta \approx 1.75$ and detailed calculations [80] led to the formula $\eta \approx 1/(1 - \omega^2/\omega_p^2)$ emphasizing the effect of the plasma density in the absorption. Absorption fraction (equation 3.33) estimated by the Brunel model shows an angular dependence of the absorption peaking at high incidence angle ($\theta \gtrsim 80^\circ$) and the dependence on the laser irradiance follows $A_B \propto \sqrt{I_L\lambda^2}$. Additional calculations [112] emphasize the effect of the collisions onto the pump laser in limiting the absorption to become unphysically large.

The simple model proposed by Brunel is extended by different theoretical approaches and analyzed by numerical simulation [86, 87, 88, 89]. In an approach closer to the real experimental conditions, P. Gibbon and A. R. Bell [86] analyzed the Brunel effect (addressed as *"vacuum heating"*) by help of $1\frac{1}{2}D$ *PIC* simulations and considered the effect of finite density gradients of the plasma-vacuum interface on the absorption fraction. The studies cover the transition regime from the resonance absorption to the vacuum heating for density scales lengths $L/\lambda = 0.01 \div 2$ and laser irradiances from $I_L\lambda^2 = 10^{14}\,\mathrm{W/cm^2}\mu\mathrm{m}^{-2}$ to $10^{18}\,\mathrm{W/cm^2}\mu\mathrm{m}^{-2}$. The results indicate that the optimum absorption angle is about 45° and reveal a complex dependence of the absorption fraction on the laser intensity due to the interplay between the laser driver intensity and the plasma profile. For example, at a laser intensity of about $10^{16}\,\mathrm{W/cm^2}$, the absorbed fraction becomes larger with the increased scale length due to the longer penetration depth of the laser into the matter and consequently, the possibility to extract more electrons able to absorb energy from the laser. At the optimum absorption angle, the absorption decreases from about 70% for $L/\lambda = 0.1$ to only 10% for steeper plasma profiles of $L/\lambda = 0.01$.

Experimentally, the interaction regime where the condition $L < x_q$ is fulfilled was achieved by a good control of the laser prepulse-main pulse contrast or by the effect of the radiation pressure ($P_L = 2I_L/c$) which steepens the plasma profile during the interaction. Therefore, the vacuum heating model was identified as dominant collisionless mechanism of the laser absorption in different experiments (e.g. [89, 108, 111]) for p-polarized laser beams in the low intensity regime in the range of $I = 10^{13} - 10^{15}\,\mathrm{W/cm^2}$. In the relativistic regime $I \geq 10^{17}\,\mathrm{W/cm^2}$, additional effects are considered like ion shelf expansion during the interaction or the steepening of the electron density profile by the radiation pressure, P_L of the ultraintense laser which overcome the plasma thermal pressure, P_{th} [87, 90],

$$\frac{P_L}{P_{th}} = \frac{2I_L/c}{n_e k_B T_e} \simeq 0.4 \frac{I[10^{16}\,\mathrm{W/cm^2}]}{n_e[10^{23}\,\mathrm{cm^{-3}}] \cdot T_e[eV]} > 1. \tag{3.34}$$

Considered as one of the important absorption and electron acceleration mechanisms in modern experiments of high laser intensity with solid matter, the vacuum heating still has not answered all the questions. Recently, topics like electron dynamics acceleration or transition regimes from vacuum heating to other competing collisionless mechanism were analyzed by help of numerical methods [91, 92].

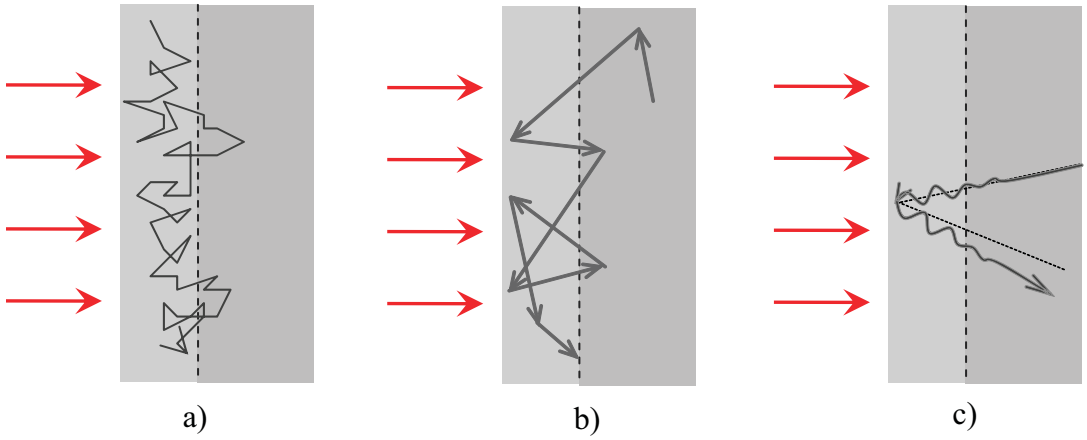

Figure 3.6: The electron trajectories in the region of the skin layer (l_s) in different skin absorption mechanisms. Collisional regime in a) the *normal skin effect*, $l_s > \lambda_e$ and $l_s > v_e/\omega_L$. Collisionless regime: b) *anomalous skin effect* $l_s < \lambda_e$ and $l_s < v_e/\omega_L$ and c) *sheath inverse bremsstrahlung* $v_e/\omega_L < l_s < \lambda_e$. The skin layer is marked by dashed vertical lines and the electron trajectories by full lines. (after *F. Wotten* [76] and *P.J. Catto and R. M. More* [93])

Collisionless skin effects

Beside resonance absorption and vacuum heating, additional collisionless mechanisms were proposed, like *sheath inverse bremsstrahlung (SIB)* [93] and *anomalous skin effect (ASE)* [96, 97] which aimed to explain the laser energy transfer to the steep plasma profile where the previous mechanisms were found not to be effective. In the case of the *normal skin effect (NSE)* (see paragraph 3.1) the electrons oscillate in the laser field and transfer the gained energy to matter mostly via collisions within the skin layer ($l_s \approx c/\omega_p$). In contrast, the *SIB* and *ASE* processes account for the thermal effects within a collisionless skin layer when the electron mean-free-path is larger than the skin depth ($\lambda_e > l_s$). The interaction regime of the skin effects corresponds to the highly ionized, heated front plasma expanded under the plasma pressure when $P_L/P_{th} < 1$ [61] (compare with the formula 3.34). In the figure 3.6 the electron trajectories within the skin layer for all three mentioned skin effects are schematically represented indicating the reciprocal relation between the electron's characteristic lengths and skin depth.

In the case of the *anomalous skin effect*, the skin depth is smaller than the mean thermal excursion length $v_e/\omega_L > l_s$ during the laser period (condition equivalent with $\omega_L^2 c^2 \ll \omega_p^2 v_e^2$) and thus, the thermal electrons travel through the skin layer and absorb energy from the field while getting reflected by the sheath potential.

In a quasilinear approach, Rozmus *et al.* [97] derived the solution for the electron kinetic equation for *ASE* assuming a low intensity regime (the oscillatory velocity is smaller than the thermal velocity, $v_q \ll v_{te}$) and a Maxwellian distribution for the electrons. The absorption fraction for a normal incident laser pulse is given by:

$$A_{ASE} \approx 0.6 \cdot \left[\frac{\omega_L}{\omega_p}\right]^{2/3} \cdot \left[\frac{v_e}{c}\right]^{1/3} \tag{3.35}$$

In addition, scaling laws for different physical parameters and interaction regimes were derived emphasizing that *ASE* starts to dominate over the *NSE* at a laser intensity of about $10^{17}\,\mathrm{W/cm^2}$. The absorption fraction shows a weak dependence on the laser intensity and is smaller than 10%. A detailed analysis was performed by Andreev *et al.* [99] studying the absorption in *ASE* conditions as a function of incidence angle and laser polarization. Assuming an anisotropic distribution function for the electrons in the direction of the heat flux, an enhanced absorption fraction in *p*-polarized geometry at grazing incidence can be obtained. Starting from $\approx 67\%$ at an incidence of about 85°, in the case of a Maxwellian distribution, the maximum value of the absorption increased with the degree of anisotropy. Experimentally, the contribution of the *ASE* mechanism is difficult to isolate from other competing mechanisms, but by help of numerical methods [92, 105], one can estimate the contribution of the anomalous skin effect in different interaction regimes.

When the transit time of the electrons through the skin layer is larger than the laser oscillation period, $c/\omega_p v_e > 1/\omega_L$, the laser energy can be absorbed by another collisionless mechanism known as *sheath inverse bremsstrahlung (SIB)*. The electron may gain energy from the laser during the oscillations within the skin layer and in the presence of the layer potential being finally reflected at the plasma-vacuum interface. In a detailed study, Yang *et.al* [94] estimate the absorption coefficient modifying the linear theory [93] by including the term $\vec{v} \times \vec{B}$ in the electron equation of motion within the skin layer. In this approach, an analytical expression for the absorption coefficient was found:

$$A_{SIB} = \frac{8}{\sqrt{2\pi}} \frac{v_e}{c} \frac{a[(a+1)\exp(a)E_1(a) - 1]}{[1 + \sqrt{\pi a}\exp(a) erfc(\sqrt{a})]/2} \tag{3.36}$$

where $a = \omega_L^2 l_s^2 / 2v_e^2$, $E_1(a) = \int_a^\infty \exp(-t)/t dt$ and *erfc* represents the complementary error function. The estimated absorption fraction for $v_e/c = 0.1$ case of a normally incident laser pulse onto an overdense plasma in the range of $n_e/n_c = 20 \div 100$

was found of about 10% or less. Comparing the results with *PIC* simulations, it was shown that the physical processes are similar for both models, *ASE* and *SIB* and they represent the two limits of the same collisionless process.

These collisionless absorption processes are effective in the presence of a thermal electron population of high energy, interacting with low/moderate intensity laser pulses. Most likely, this condition is fulfilled during the interaction of low intensity tail of the pulse after a significant heating produced by the main part. In the non- or weakly relativistic regime, the contributions of these processes do not exceed $5\% - 10\%$ [92].

3.3.3 Ultrashort high intensity laser pulses and overdense plasmas

The nomenclatures of *"ultrashort"* and *"high-intensity"* laser pulses were several times reconsidered over the last decades as soon as pulses with shorter duration and higher intensities became available. Nowadays, the ultrashort regime refers to pulses with duration in the range of femtosecond. Even in the non-relativistic regime, GW laser systems are able to provide laser pulses in high-intensity regime covering a range from $\sim 10^{15}\,\mathrm{W/cm^2}$ up to $\sim 10^{18}\,\mathrm{W/cm^2}$. As was previously mentioned, the high-intensity, ultrashort laser pulses are usually accompanied by long prepulses of *ps* or *ns* duration. The energy carried by these prepulses could be enough to produce the ionization of the targets and, at the same time, long enough for the created plasma to expand. Consequently, the laser pulse is not able to penetrate in the dense plasma layers due to its reflection at the critical density. For example, in case of an *Aluminum* plasma, the critical density represents only 1% from the solid density. In order to deposit the laser energy at higher matter densities experimentally there are in principle, two possibilities (i) one can reduce the energy of the prepulse improving the main pulse-prepulse intensity contrast ratio, defined as $r = I_L/I_p$ thus, reducing the ionizing properties of the prepulse and/or (ii) shortening the main laser pulse duration reducing the expansion time of the preplasma during the main interaction.

A constant steepening of the spatial expansion of the preplasma expressed by the normalized scale length L/λ was registered during time. Some relevant experimental results are chronologically presented in the table 3.2 where the main characteristics of the interaction regimes (main pulse and prepulse parameters) and the plasma profile estimation are summarized. The experiments addressed in this thesis represent an

Table 3.2: Interaction regimes in some relevant experimental investigations on the topic of the ultrashort, high-intensity laser pulses absorption processes by solid targets. For comparison, the interaction regime of the present experiments.

Experimental work	Main laser intensity, I_L [W/cm^2]	Main pulse duration, τ_L [fs]	Intensity contrast, $r = I_L/I_p$	Prepulse duration, τ_p [ns]	Plasma profile, L/λ
Kieffer *et al.* (1989) [65]	$\lesssim 10^{15}$	1000	10^3	0.03	$\leqslant 0.2$
Fedosejevs *et al.* (1990) [68]	$\sim 10^{15}$	250	$\sim 10^7$	7	0.1
Borghesi *et al.* (1999) [139]	5×10^{17}	500	10^6	10	0.4-0.9
Eidmann *et al.* (2001) [135]	3×10^{16}	150	10^{10}	2	0.05-0.06
Present experiments [143, 144]	5×10^{16}	~ 8	10^8	5	0.01

important step further towards the aim to deposit the laser energy in overdense plasmas [143, 144]. The high contrast (10^8) on a nanosecond time scale of the prepulse (see paragraph 4.1.1) in combination with the extremely short duration of the main pulse ($\tau_L = 8\,\text{fs}$) lead to a novel interaction regime of the high intensity laser pulse with overdense plasma. Computer simulations offer an estimation of the plasma profile of $L/\lambda \approx 0.01$ as discussed in paragraph 5.2.2.

3.4 Atomic physics in dense plasmas

The laser energy fraction absorbed by the plasma is converted in principal in electron energy (thermal or highly energetic). The interactions of the electrons and photons with the other plasma constituents (ions, atoms) determine a large variety of atomic processes like ionization, excitations, recombination. Thus, the created plasma becomes a radiation source and the emission spectra contain important information about local plasma parameters like density, temperature, microfields strength. In particular, for highly transient plasmas produced by ultrashort laser pulses, spectroscopic investigations proved to be one of the most suited method for studying the plasma spatial and temporal evolution.

3.4.1 Atomic processes

In this paragraph, the main atomic processes which determine the radiative transitions or the changes in the ionization or excitation state of the atomic systems will be listed. The direct processes will be analyzed together with their inverse processes. The rate coefficients of the processes dominant in dense plasmas will be discussed due their importance in the balance rate equations within different radiative plasma models (*Local Thermodynamical Equilibrium (LTE), non-LTE, corona equilibrium*) [32].

Excitation and deexcitation processes

Electron impact excitation and deexcitation
The transition of a bound electron from a lower (m) to a higher (n) level is induced by an inelastic collision of an atomic system (ion, atom) with an electron (m, n are the quantum numbers of the levels involved in the transition). The collisional excitation rates can be deduced for each specific ion charge but, in general, have the form $X_{mn} \propto f_{mn} \cdot \exp(-E_{mn}/kT_e)/(E_{mn}\sqrt{T_e})$, where f_{mn} is the oscillator strength, $E_{mn} = E_n - E_m$ is the energy of the transition and T_e is the electron temperature [47]. The excitation process has the maximum probability when the electron temperature $T_e \approx E_{mn}$ (in order of few hundreds of eV for low Z-materials). The inverse process, collisional deexcitation, occurs when a free electron collides with an excited ion and induces the transition $n \rightarrow m$. The coefficient rates of these processes are connected by the detailed balance equation: $D_{nm}/X_{mn} = (g_m/g_n) \cdot \exp(-E_{mn}/T_e)$, where D_{nm} is the coefficient rate of the deexcitation process and $g_{m,n}$ are the statistical weights of the states.
Photoabsorption, spontaneous and induced radiative decay
A bound-bound transition $m \rightarrow n$ occurs when a photon of energy $h\nu = E_{mn}$ is absorbed. The radiative decays are inverse processes and can occur spontaneous or induced by a photon. These processes are governed by the well-known Einstein coefficients which measure the probability of the spontaneous (A_{nm}) and induced decay (B_{nm}) and of the resonant absorption (B_{mn}). At the thermal equilibrium, the transitions between two levels are balanced: $N_n \cdot B_{mn} = N_m \cdot (A_{nm} + B_{nm})$, where $N_{n,m}$ are the population densities in the levels n and m [108].

Ionization and recombination processes

Electron impact ionization (EI) and three-body recombination

The ionization process induced by the impact of a free electron with an atomic system is one of the important processes in hot, dense plasmas. Three-body recombination of an ion occurs in the presence of two electrons when one is captured in a bound state while the other takes the released energy. The electron impact ionization was analyzed in the paragraph 3.2. A good approximation for the rate coefficients of *EI* for different electron populations are given by Lotz's formulas 3.2. The rates for the inverse process can be estimated from the balance equations. For both processes, the coefficient rates are proportional with the electron density showing an increased probability for these events in the case of dense plasmas and attain a maximum when the electron temperature is few times the binding energy [32].

Photoionization and radiative recombination

The photoionization (PI) is a threshold process which occurs when a photon with an energy larger than the binding energy is absorbed by a bound electron. In an inverse process of radiative recombination, an electron is captured in a bound state releasing radiatively its kinetic energy. The photoionization process becomes important for a high photon density in optically thick plasmas where the photon is reabsorbed in the plasma. In optically thin plasmas, the photons easily escape from the plasma volume and the photoionization rate decreases significantly. If the radiation field is represented by Planck's law and characterized by a temperature T_r, the PI coefficient rate is proportional to $P_n \propto I_{p,n}^{5/2}/T_r^3$, where $I_{p,n}$ is the ionization potential of a bound electron in a quantum state n [47]. For example, in the case of photoionization of K-shell electrons, the process is more efficient for high-Z elements with higher ionization potentials than for low-Z materials [32]. The nonlinear effects induced by the high density flux of the photons in a laser pulse have been discussed in the paragraph 3.2.

Autoionization and dielectronic recombination

In these processes, two excited levels are involved. In an autoionizing process, the energy released by a bound electron in a radiative decay is taken by an other bound electron which becomes free. The dielectronic recombination is a two-step process and occurs when a free electron is captured in an excitated state. The extra energy is absorbed by a bound electron and is excitated to a higher state. From this configuration, an auto-ionizing process or radiative decay may occur. These atomic processes lead to the emission of satellites lines which are important spectral features

in the emission spectra and used for diagnosis of the plasma temporal and spatial evolution (e.g. [36, 38, 39]).

3.4.2 Atomic effects in high density plasmas

Inside of a plasma, the electronic energy states of an emitting ion or atom are perturbed by the micro-fields of its own bound electrons and of the nearby ions and free electrons. The combination between the nuclear Coulomb potential and the plasma potential influences atomic parameters like, binding energy, rate coefficients or oscillator strengths. The effect of the plasma environment on the atomic processes increases with the plasma density [48] and, in particular cases of dense plasmas, lead to specific phenomena like: *pressure ionization*, *continuum lowering*, *satellites line emission*, *atomic level shifts* or *line pressure broadening*.

The bound electrons of an ion immersed in a plasma are affected by the plasma potential which reduces the electrons' ionization potential. The effect is known as *continuum lowering* or *ionization potential lowering* [32] and the reduction of the ionization potential (IP) has, in general the form : $\Delta E_{CL} = Ze^2/R^*$, where Z is the ion charge and R^* is a characteristic radius. In the case of dense plasmas, for ion density $n_i > 10^{21}\,\mathrm{cm}^{-3}$, this radius is estimated as the ion radius $R^* = R_i = (4\pi n_i/3)^{-1/3}$ [35]. This approximation indicates a similar lowering for all bound levels and shows a stronger effect with the increased plasma density. At higher density, for electrons on the upper atomic level, the binding energy can be compensated by the electrostatic potential for nearby ions and their bound states are shifted into the continuum. The effect is called *pressure ionization* and a schematic representation of this effect is shown in figure 3.7. The pressure ionization occurs due the reciprocal potential modifications of neighbor ions where the wavefunctions of the electrons found in higher atomic states overlaps. In this case, the ionization potential depression is expressed as [34, 35]:

$$\Delta E = 2.16 \times 10^{-7} \frac{Z}{R_i} \left\{ \left[1 + \left(\frac{R_D}{R_i} \right)^3 \right]^{2/3} - \left(\frac{R_D}{R_i} \right)^2 \right\} \ (eV) \tag{3.37}$$

where $R_D = \sqrt{\varepsilon_0 k T_e / n_e e^2}$ is the Debye radius.

In the emission spectra of dense plasmas, beside resonance lines of multiple ionized ions, low intensity spectral features are detected in the vicinity of the resonance lines, in lower energy side. These structures are called *satellite lines* and their emis-

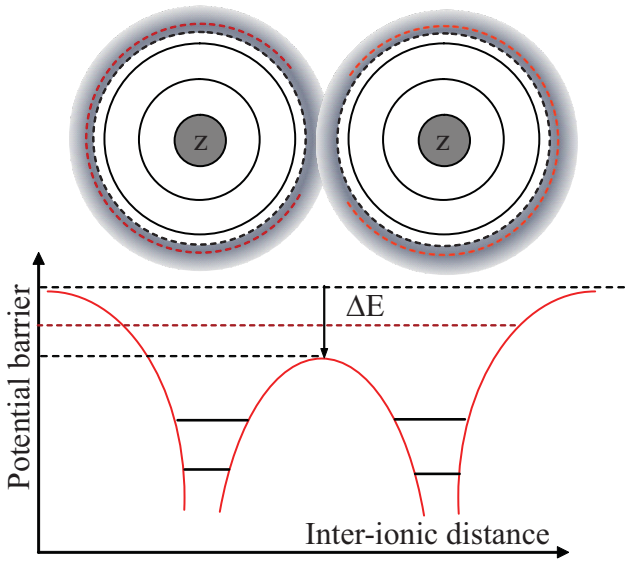

Figure 3.7: Schematic representation of the high density effect on the electronic energy level. As an effect of *pressure ionization*, the potential barrier between two ions is lowered and the outer bound electronic states are shifted into continuum. *After Salzmann [32].*

sion originates from the dielectronic recombination processes followed by a radiative decay in the presence of one or many electrons in an excited state (often called *spectator electrons*). These electrons reduce slightly the ionization potential of the atomic states and consequently, the emitted photon energy. Thus, the satellites lines have wavelengths on the red side, close to the resonance line, the so-called *parent line*. In figure 3.8 the electronic configurations at the emission of a resonance line (He_α, $1s^2 - 1s2p$) and of the associated satellites ($1s^2n'l' - 1s2pn'l'$) are schematically represented. In this configuration, the satellites correspond to a *Li*-like ion and consequently, they are called *Li*-like satellites of a *He*-like resonance line. The spectator electron can occupy a large number of atomic states (in the presented example, $n \geq 2$) which lead to the emission of an equally number of satellites. Their wavelength does not differ to much and often appears in the spectra as overlapped structures. At high plasma densities, the rates of dielectronic recombination processes increase and conditions for emission of satellite lines is enhanced. The ratio intensities of the satellites lines and the parent lines is used in plasma diagnostic due to its dependence on the electron temperature, plasma density and ionization degree (see e.g. [40]).

Another effect which can be identified in the spectral response of dense plasmas is the *shift of spectral lines* (known also as *polarization shift (PS)*) [37]. The effect is generated by the modification of ionization potential by the free electrons of the plasma environment. While the continuum lowering is a first order effect, the polarization shift is a second order effect where the radial distribution of the electrostatic potential created by the free electrons around the ion nucleus perturbs

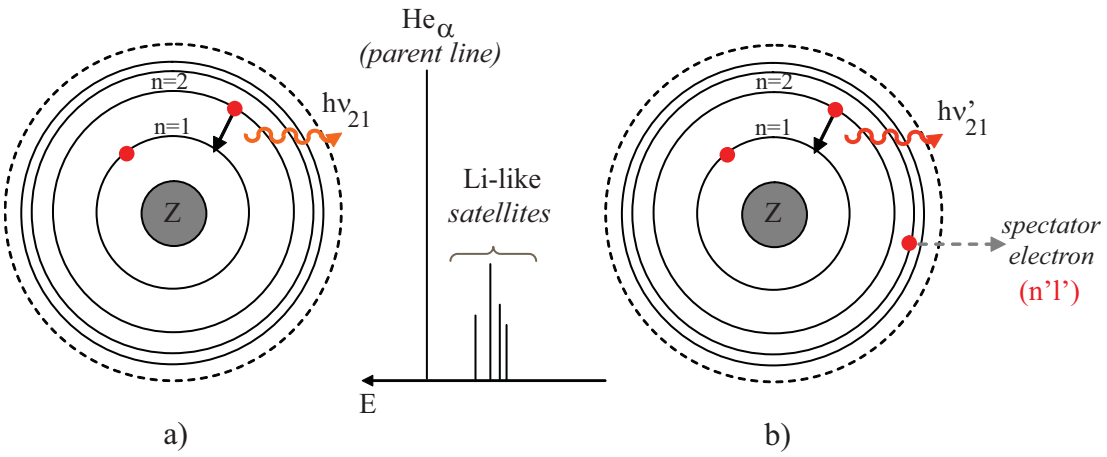

Figure 3.8: Schematic drawing of the electronic configuration at the emission of a K-shell resonance line (*parent line*) and of its satellites lines. In figure (a) the emission of the α line ($1s^2 - 1s2p$) of a *He*-like ion is represented. In figure (b) the electronic configuration at the emission of *Li*-like satellites ($1s^2n'l' - 1s2pn'l'$) in the presence of one *spectator electron* is drawn.

slightly different the energy of the ionic states [32]. Thus, the energy $h\nu$ of an emitted photon at the transition between two levels of an ion in a plasma is smaller than the energy $h\nu_0$ of a photon in the same transition of an isolated ion. The difference $\Delta h\nu = h\nu - h\nu_0$ is negative and represents a red shift of the spectral line induced by the plasma.

Summarizing, the effects induced by the high density plasma in the atomic processes can be recognized in spectral structures and features of the emission spectra and represent "signatures" of the dense plasma state.

3.4.3 Thermodynamic equilibrium in dense plasmas

An important parameter in describing the plasma state is the ionization degree Z^* which determines other plasma properties like electron density, transport coefficients or the equation of state [112]. The rates of ionization and recombination processes determine the abundance of different charge state of the plasma ions. In a similar manner, the populations of different excited state are induced by the balance between the excitation-deexcitation rates. In laser produced plasmas which have in general a small volume, the radiation can partially escape freely at the plasma boundaries and cannot reach the complete thermodynamic equilibrium (TE) with the plasma particles. Therefore, a more often used model is the *local thermodynamic equilib-*

rium (LTE) where only the particles are in equilibrium and the radiative/ionization processes are balanced by their inverse processes. *LTE* approximation is applicable mainly for dense, optically thick plasmas where the balance between the collisional processes (electron impact ionization) and the three-body recombination processes occurs. Optically thick plasmas denote plasmas where a significant part of the emitted radiation is reabsorbed within the plasma volume. The charged particles (electrons and ions) reach the equilibrium via collisional processes on a time scale $\tau_{ei} = 1/\nu_{ei}$ much shorter than the plasma living τ_p time (for a dense plasma of density $n_e = 1 \times 10^{23}\,\mathrm{cm}^{-3}$ and temperature $T_e = 100\,\mathrm{eV}$, the relaxation time τ_{ei} is about 10 fs while τ_p is in order of ns). The velocity distribution of electrons and ions is described by the Maxwell-Boltzmann distribution (for hot plasmas) or by Fermi-Dirac distribution (for cold plasmas). Also, the densities of successive ionization stages are calculated as solution of Saha equation while densities of excited states for each ion are given by the Boltzmann equation.

In optically thin plasmas, the radiation with broader band frequency can escape almost completely through the plasma boundaries and the radiative processes cannot be compensated by collisional and photon excitations. This situation is known as *non-LTE*. In this case, for determining the population of each charge state, the coupled set of atomic rate equations have to be solved time-dependently [41]. Accounting for the large number of possible excited states, specially for high-Z elements, a corresponding large set of equation results and different models are used for simplifying the calculations [112].

The plasmas produced by ultrashort laser pulses are, in general, transient, optically thin and have large gradients of physical parameters (n_e, T_e, mass density) during the heating process. The validity of the LTE steady-state in modeling these plasmas was analyzed and limits of this validity were estimated [46]. In principal, is considered that a plasma is near to *LTE* state for densities

$$n_e \geq 9 \times 10^{17} \left(\frac{\Delta E}{E_H}\right)^3 \left(\frac{T_e}{E_H}\right)^{1/2} cm^{-3} \tag{3.38}$$

when the deviation from the Boltzmann distribution is smaller than 10%. Here, ΔE is the energy of the first excitated state from the ground level and E_H is hydrogen atom ground state energy. A similar condition was estimated for the validity of the

Saha equation if the plasma density is:

$$n_e \geq 1 \times 10^{14} T_e^3 \left(\frac{E_z}{T_e}\right)^{(5/2)} cm^{-3} eV^{-3} \tag{3.39}$$

where E_z is the ionization energy of the charge state Z. Accounting for these criteria, in a Lithium plasma at 100 eV temperature, the Saha equation is satisfied for $n_e \geq 1 \times 10^{20}\,\mathrm{cm}^{-3}$ and the Boltzmann distribution is valid for $n_e \geq 1 \times 10^{21}\,\mathrm{cm}^{-3}$ while for an Aluminium plasma at the same temperature these conditions are fulfilled at $n_e \geq 3 \times 10^{23}\,\mathrm{cm}^{-3}$ and $n_e \geq 5 \times 10^{24}\,\mathrm{cm}^{-3}$, respectively. The near LTE state was already applied for modeling transient plasmas [51, 140].

Chapter 4

Laser set-up and plasma diagnostics

In this chapter, experimental arrangements used for the investigations of the overdense plasmas produced by sub-10 fs laser pulses are described. In the framework of this thesis, two experimental set-ups were developed for performing the absorption measurements and the XUV plasma spectroscopy. The GW laser system used in both experiments is described and the diagnosis of the laser focus parameters is presented. The experimental set-up developed for the absorption measurements includes an integrating (Ulbricht) sphere for measuring the energy of the incident and reflected laser pulse. The sphere performances like reflectivity, transmission and linearity are discussed in the radiation intensity range relevant for the experiment. The absorption process is strongly depending on laser-plasma physical parameters. Consequently, the experimental set-up was designed to allow the variation during the measurements to different parameters like incidence angle, laser polarization and laser intensity. The recording and data analysis techniques are detailed in a separate paragraph.

For the spectroscopic investigation of overdense plasmas in the XUV range a high resolution spectrometer was constructed. The diffractive element was a varied-line spacing toroidal grating with a flat field focal plane. Gratings with 380, 960 and 2400 lines/mm can be used in the same spectrometer geometry and they cover a spectral range from 16 Å up to 250 Å. Two types of detectors can be mounted at the spectrometer focal plan: a CCD Proscan camera and Fuji image plates. The spectral resolution of the spectrometer was limited by the detector resolution and, for the spectra recorded with the CCD camera a resolution better than $\lambda/\Delta\lambda = 600$ at 2.5 nm was found.

4.1 Sub-10 fs laser pulse

4.1.1 The *GW*-laser system

The interaction regime where the laser pulse energy is deposited onto plasma with a density close to solid can be achieved with laser pulses of ultrashort duration and good contrast ratio which prevent the preplasma formation and significant expansion during the interaction. In present experiments, 8 fs laser pulses were generated and amplified by a commercial Femtopower *GW*-laser system operating in CPA [117, 118] mode. The laser pulses delivered $100 - 120\,\mu$J energy at 790 nm (central wavelength) onto the target.

For the production of ultrashort, high intensity laser pulses one benefits for the specific properties of the *Ti:Sa* crystal as gain medium. It represents a Titanium doped Sapphire crystal ($Ti^{+3} : Al_2O_3$) with broad spectral band of the laser transition centered around $\lambda_0 \approx 800\,\text{nm}$ [119]. The large lasing bandwidth $\Delta\lambda_l$ allows the emission of ultrashort laser pulses, according with the relation $\Delta\lambda_l \cdot \tau_l \geq 2\ln 2\lambda_0^2/(\pi c)$, where τ_l is the pulse duration and c, speed of light [122, 125]. For operating in pulsed mode, the coupling and the modulation of the longitudinal modes supported by the laser cavity is required. The process is known as *mode-locking*. In case of the *Ti:Sa* lasers, this modulation in amplitude is achieved by the Kerr mechanism [121]. Due to this effect, the dependence of refractive index with the intensity ($n = n_0 + n_2 I$, where n_2 is the nonlinear coefficient of the refractive index) induces the self-focusing of the pulse on the crystal. The reduced diameter of the pulse leads to a increased gain profile for higher intensities and consequently, to a favorable energetic condition for the laser to run in pulsed mode over the continuous mode. This technique is known as *self-mode-locking* or *Kerr-lens mode locking (KLM)* [123, 125].

According to the CPA (*Chirped-Pulse Amplification*) technique [117], the main components of the laser system consists of a oscillator-stretcher combination, a 9-pass Ti:Sa amplification stage and a hollow fiber-compression combination as pulse compression stage. A simplified layout of the *Femtopower* laser system is presented in the figure 4.1. Ultrashort laser pulses are primarily generated by a self-mode-locked *Ti:Sa* oscillator (*Femtosource Scientific Pro*). The optical pumping of the crystal is realized by a frequency-doubled Nd:YAG laser beam focused in continuous-wave (cw) mode onto the sapphire crystal. Special designed chirped multi-layer mirrors are used to compensate the large intra-cavity dispersion [126, 127]. Thus, at

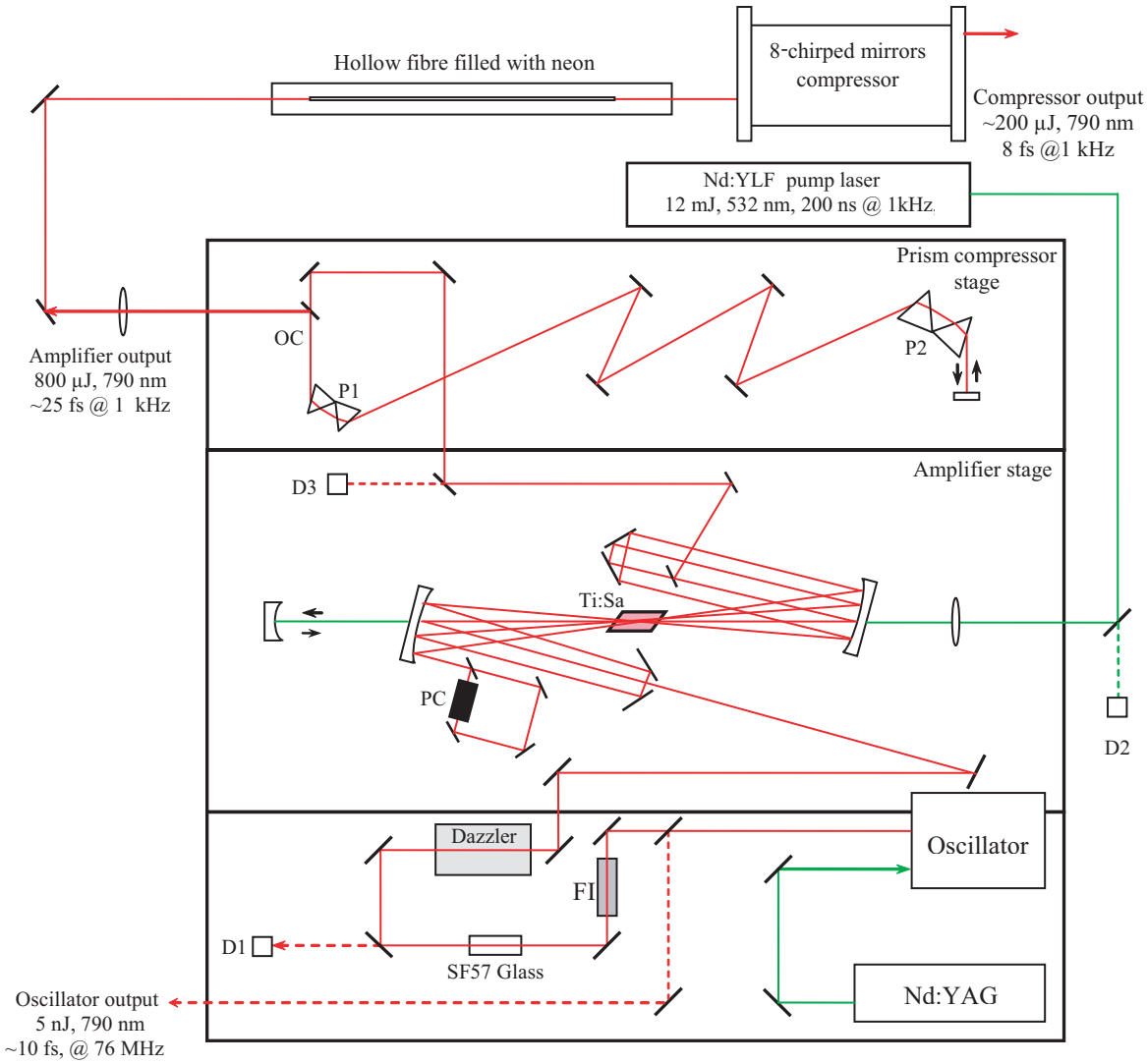

Figure 4.1: A simplified overview of the laser system. The laser pulse path through the system and main components are presented in block stages. It includes, from the bottom to the top: (1) the Ti:Sa oscillator and the optical set-up of the pulse stretcher, (2) the Ti:Sa multi-pass amplifier, (3) the optical layout of the prism compressor and (4) the last compression stage as a combination of hollow fibre-chirped mirrors. Detailed description of the optical components and their functionality are given in the text. A number of diodes (D) are used for the alignment and pulse monitoring.

the oscillator output are delivered laser pulses of about 10 fs duration and a spectral bandwidth of ≈ 95 nm. The pulses are emitted with ≈ 76 MHz repetition rate and each pulse carries 5 nJ energy. This energy focused by common optical elements leads to intensities too low for most of the research interest in nowadays. An ampli-

fication of the laser pulse is required. The pulse propagation in the amplifier medium might lead to strong nonlinearities in the amplifier medium or even damages of the optical components at high peak intensities. Consequently, the laser power at the oscillator output will be first lowered by stretching the pulse in time, then the pulse is amplified and finally will be re-compressed. After the oscillator stage, the laser pulse propagates through 5 cm of SF57 glass and it is temporally stretched by a factor of $\approx 10^3$. A Faraday isolator (FI) assures the optical separation of the oscillator from the other laser stages. Before entering in the amplifier, the pulse is shaped in phase and amplitude by help of an acousto-optic dispersive filter (Dazzler) [128].

The amplification stage includes a *Ti:Sa* crystal optically pumped by a pulsed *Nd:YLF* laser frequency-doubled (532 nm). The pumping laser delivers pulses of 200 ns duration and $\approx$ 12 mJ energy in a repetition rate (1 kHz). The seed pulses undergo 9 round trips inside of the crystal and are amplified by a factor of $2 \cdot 10^5$. The optimal time synchronization between the oscillator pulses and the pumping laser is realized by a combination of a Pockels cell with two cross-polarizers. Thus, the repetition rate of the amplified pulses is lowered to that of the pumping laser of 1 kHz. After the amplification stage, due to the large dispersion experienced in the crystal and other optical components, the amplified pulses have a duration of about 10 ps. The re-compression of the pulse is performed in two stages. In the first one, a double-pass prism compressor reduces the pulse duration to about 25 fs. Spectral bandwidth of the pulse is $\approx$ 50 nm and the energy per pulse at the amplifier output is about 800 μJ.

Due to the bandwidth limitation, further compression requires additional spectral broadening of the pulse. The solution adopted in the present laser system for increasing the pulse bandwidth was suggested by the nonlinear effect of self phase modulation (SFM) experienced by the pulse propagating in a hollow fibre filled with noble gas [129, 130]. The SFM process occurs as a consequence of the time-dependent phase shift induced by Kerr effect accounting for the temporal variation of the laser intensity. The laser pulse was focused onto a hollow fibre of 1 m length and 250 μm filled with neon. Propagation through the fibre leads to a pulse spectrum is about 135 nm at the expense of 50% transmission fraction. The latter compression stage consists in 8 chirped mirrors enclosed in vacuum which allow a reduction of the pulse duration to less than 10 fs and, in the same time, compensate the pulse dispersion induced by the propagation of the pulse in air and by different coupling optical elements. Experimental measurements of the temporal pulse profile using

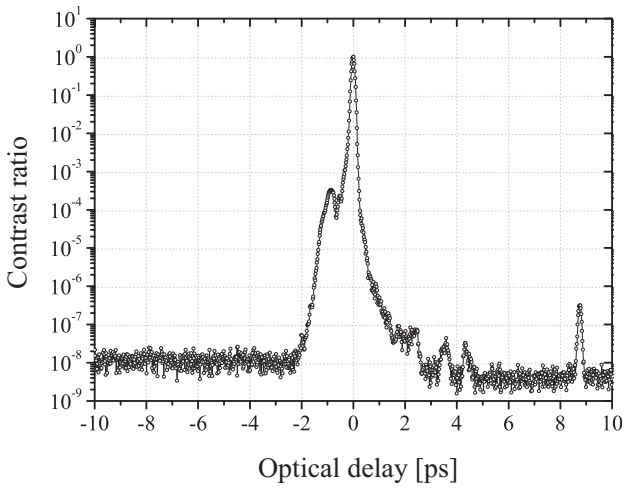

Figure 4.2: Contrast ratio measurements of the amplified pulses on the *Ti:Sa* laser system recorded after the prism-compressor.

the 2^{nd} order autocorrelation technique [125] revealed a pulse duration of $\approx$ 8 fs ($FWHM$) [133]. After leaving the compressor, the pulse propagated only in the vacuum through the beam line up to the interaction chamber to avoid further pulse distortion.

The temporal profile of the laser pulse and the energy fraction deposit on the pulse pedestal or prepulses is of key importance in the production of overdense plasmas. Within the high intensity pulse generation as well as during the spectral and temporal shaping, a number of physical processes and/or technical conditions may affect the temporal shape of the main pulse. For example, in the amplification stage, the stimulated emission is accompanied by the spontaneous emission which undergoes as well amplification (Amplified Spontaneous Emission-ASE). In the present set-up, the Pockels cell acts as a pulse picker after the 4^{th} round trip through the amplifier with an opening window of about 10 ns. Consequently, within this time interval, the spontaneous emission background is reinjected together with the picked pulse in the crystal and is further amplified in the next 5 rounds. Moreover, the inherent leakage of the Pockels cell-polarizers combination may release in the amplification trip parasitic pulses from the oscillator. The temporal distribution of the laser intensity can be experimentally measured using the third-order autocorrelation technique [131]. In the figure 4.2 the correlation trace of pulse at the entrance of the hollow fibre recorded by help of a high dynamic range 3^{rd} order cross-correlator (*Sequoia*, Amplitude Technologies) is presented. The diagnosis reveals a contrast ratio of about $3 \cdot 10^5$ for times larger than 1.3 ps before the main pulse and better than $\approx 10^8$ for the ASE prepulse. After the last compression stage it is expected that the contrast improves by a factor of about 3 on the *ps* time scale. This estimation

accounts to the selective process of the self modulation on the hollow fibre which is effective for the high intensity part of the pulse (the main pulse) but not for the low intensity prepulse. The main pulse is efficiently compressed in the 8-chirped mirrors set-up by a factor of ≈ 3 and thus, the intensity of the main pulse and the contrast is increased by the same factor.

4.1.2 Spatial and temporal characteristics of laser focus

Previous experimental and theoretical work demonstrated that the energy transfer process of the high intensity laser pulse to the solid target may depend on the intensity and energy density of the incident laser radiation. Therefore, a careful characterization of the laser propagation in vacuum and the focus parameters are required. After leaving the compressor, the laser beam is guided along the beam line by a number of high-reflectivity (HR) dielectric and silver mirrors into the target chamber. The laser pulse path through the beam line and the coupling set-up in the target chamber is schematically drawn in figure 4.3. In the beam line and target chamber the vacuum was better than 10^{-5} mbar. The last turning HR mirror optimized for 22.5° installed in the top of the chamber leads the laser beam to a gold coated 45° off-axis parabola (OAP) with an f-number of f/2.5 and an effective focal length of 108 mm. The laser beam was focused onto the target to a spot diameter of $\approx 3.2\,\mu$m ($FWHM$) and was linearly polarized along the axis Ox.

The focus parameters and quality were checked prior to every experimental session. For this purpose, two separate set-ups were integrated in the main experimental set-up. In figure 4.3 these arrangements are presented in case of absorption measurements. The first set-up included a remotely controlled motorized microscope objective (with a standard magnification of 40x and an f-number $f/\# = 2$) mounted coaxially to the laser beam optical axis. The objective allowed the imaging of the laser focus onto an 8 bit *CCD* camera or 12 bit beam profiler. A Helium-Neon laser ($\lambda_{HeNe} = 633$ nm) was coupled along the Ti:Sa laser beam path for pre-alignment purposes. The magnification of the focus diagnostic arrangement was determined using a 0.5 cm spaced transmission grating placed in the expanded collimated He-Ne laser beam. The estimated value of the magnification was of about 35. The best focal position and the focus parameters were experimentally investigated for He-Ne laser beam and for the *Amplified Spontaneous Emission (ASE)* of the Ti:Sa laser. A typical 2D image of the focal spot recorded with the beam profiler is presented in figure 4.4 b). The evaluations of the measurements will be discussed later on in

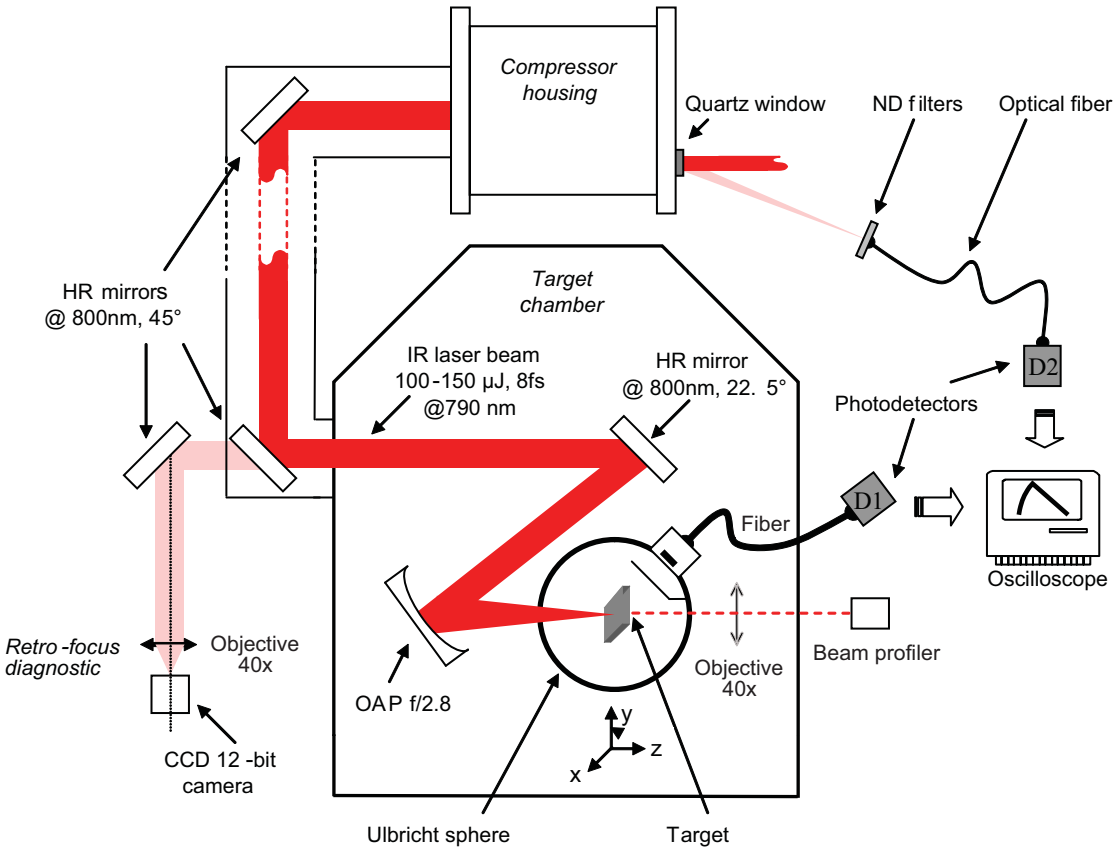

Figure 4.3: Schematic of the set-up for the absorption experimental investigations

this paragraph.

The second additional set-up was a retro-focus diagnostic (see figure 4.3) with the purpose to monitor the focus quality during the shots. The system was able to image the focal spot benefiting from the metallic target reflectivity and using the small fraction of the back reflected laser beam which leaked from the last dielectric turning mirror mounted in the beam line before entering the target chamber. This radiation fraction passes through an optical system including an achromat lens ($f_a = 20\,\mathrm{cm}$) and a microscope objective ($f/5$) and was relied onto a 12-bit *CCD* camera. In the case of absorption measurements, the retro-focus diagnostic allowed the visual control of target position in the focal plane at each shot, as long as the number of the open ports of the Ulbricht sphere was kept at a minimum and a direct sight of the target in the interaction zone was not available during the experiments.

In the following, the main physical properties of an ideal Gaussian laser pulse propagating in free space will be summarized considering the analysis and results

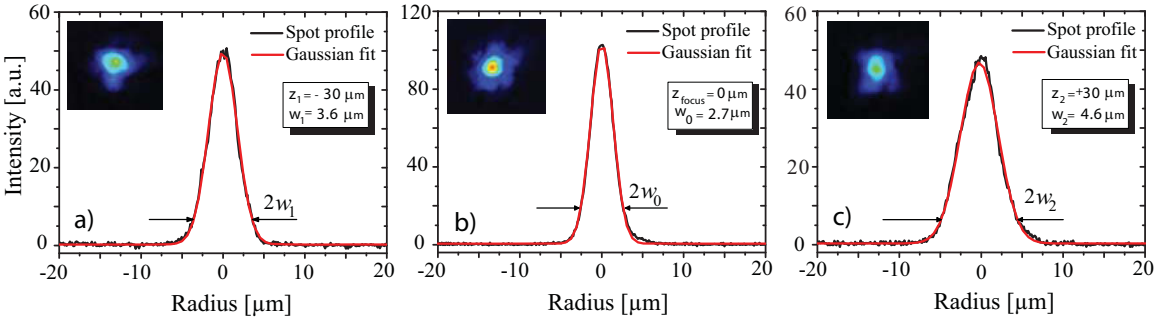

Figure 4.4: Beam profile and the gaussian fit a) at the position $z_1 = -30\mu m$ before the focus, b) at the focal position and, c) at the position $z_2 = +30\mu m$ after the focus along the optical axis of the laser beam. For each profile, the insets represent the 2D image of the beam spot recorded with the beam profiler.

described in [120, 121, 122, 132]. The relevant results from the experimental interest point of view of the focus characteristics and energy density delivered to the targets will presented.

A monochromatic, linearly polarized optical wave with a frequency ω_0 can be described, in the most general way, by the temporal evolution of the electric field as

$$\vec{E}(t) = \vec{E}_A(t) \cdot \cos[\omega_0 t + \varphi(t)] \ , \tag{4.1}$$

where $E_A(t)$ is the envelope pulse and $\varphi(t)$ is the time-dependent phase. The flux of energy carried by the electromagnetic wave ($\vec{E}(t)$, $\vec{B}(t)$) in the vacuum (free-space) is expressed by the Poynting vector:

$$\vec{S}(t) = c^2 \varepsilon_0 \cdot \vec{E}(t) \times \vec{B}(t) \ , \tag{4.2}$$

where c is the speed of light in vacuum and ε_0 denotes the electric permittivity of free space. At optical frequencies, $\vec{S}(t)$ has a very rapid variation in time and, in practical measurements, a more accessible quantity is intensity, I, defined as the time-average value of the Poyting vector

$$I(t) \equiv \left\langle \left| \vec{S}(t) \right| \right\rangle = \varepsilon_0 \cdot c \cdot \left\langle E^2(t) \right\rangle = \frac{\varepsilon_0 \cdot c}{2} \cdot E_a^2(t) \ . \tag{4.3}$$

In particular, the propagation of the lowest-order mode (termed TEM_{00}) of a Gaussian pulse will be analyzed as it is a very good approximation of the laser beam produced by stable laser resonators with finite diameter mirrors. The electric field

of a transversal Gaussian pulse is spatially described by a pulse envelope

$$E(r) = E_0 \cdot e^{-(r/w)^2} \ , \tag{4.4}$$

where r is the distance to the optical axis Oz and w is the Gaussian beam radius which represents the position where the electric field decreases by a factor of e, namely $E(w) = E_0/e$. The beam radius, w, and the *full width at half maximum* of the electric field, $FWHM_E$, are connected by the formula $FWHM_E = 2 \cdot \sqrt{ln2} \cdot w$. Accounting for the formula 4.3, one may express the radial distribution of the beam intensity as

$$I(r) = \frac{\epsilon_0 \cdot c}{2} \cdot E_0^2 \cdot e^{-2(r/w)^2} = I_0 \cdot e^{-2(r/w)^2} \tag{4.5}$$

and, at the Gaussian radius w, the beam intensity drops to $1/e^2$ from its peak value, I_0 onto the axis. The *full width at half maximum* of the intensity $FWHM_I$ can be determined from the relation $FWHM_I = FWHM_E/\sqrt{2}$ and can be connected with the Gaussian beam radius as $FWHM_I = \sqrt{2 \cdot ln2} \cdot w$.

Besides the radial distribution of the beam intensity, one has to consider the dependence of the beam intensity on the z coordinate while the beam is propagating along the optical axis Oz and is focused. Analogous with the experimental conditions, the propagation of a gaussian laser beam after a focusing element with a focal length, f and an aperture of diameter D is schematically represented in the figure 4.5. The position of the focal plane is at $z = 0$. One of the most important beam parameters is the *minimum radius of the Gaussian beam* at the beam waist w_0 where the wave front is planar. The propagation of the beam in vacuum is fully characterized by w_0 and λ, the radiation wavelength. For the geometry considered in figure 4.5, where the minimum radius is placed at $z = 0$, the dependence of beam radius $w(z)$ on the z coordinate follows

$$w(z) = w_0 \cdot \left[1 + \left(\frac{\lambda \cdot z}{\pi \cdot w_0^2}\right)^2\right]^{1/2} . \tag{4.6}$$

The radius of curvature of the wave fronts at any plane z is given by

$$R(z) = z \cdot \left[1 + \left(\frac{\pi \cdot w_0^2}{\lambda \cdot z}\right)^2\right] . \tag{4.7}$$

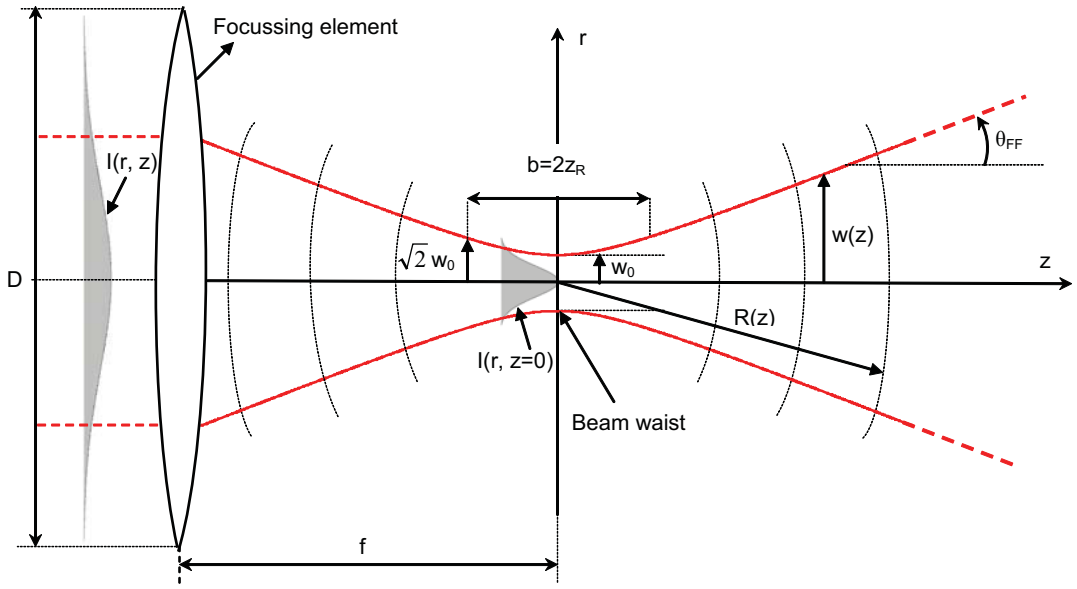

Figure 4.5: Geometry of a spherical Gaussian beam propagation after a focusing element. The $1/e^2$ beam profile for the intensity together with the significant laser beam parameters and their nomenclature are represented. The origin $z = 0$ is at the beam waist.

The variation described by formula 4.6 expresses the influence of the minimum beam radius in defining the propagation of the Gaussian laser beam: for smaller w_0, the beam remains collimated over a shorter distance in *the near field* and expands more rapidly due to diffraction in *the far field*. The near field is extended over a distance from the beam waist up to a beam radius of $w_0\sqrt{2}$ (corresponding to a double beam area) called *Rayleigh length*

$$z_R \equiv \frac{\pi \cdot w_0^2}{\lambda} \ . \tag{4.8}$$

In particular, the full distance $b = 2z_R$ between the planes corresponding to $w_0\sqrt{2}$ is termed as *the confocal parameter* and defines the volume of the beam where the diffraction effects are minimized. In the far field ($|z| >> z_R$) the beam propagation

is characterized by the beam radius $w(z)$

$$w(z) \approx \frac{\lambda \cdot z}{\pi \cdot w_0} \tag{4.9}$$

and the half-angle of divergence

$$\theta_{FF} = \lim_{z \to \infty} \left(\frac{w(z)}{z} \right) = \frac{1}{\pi} \cdot \frac{\lambda}{w_0} \quad . \tag{4.10}$$

Considering the geometry in figure 4.5, formula 4.9 allows to estimate the minimum spot size, diffracted limited, focused in ideal conditions by a focussing element of focal length f when the incoming beam radius is known:

$$w(z = f) \cdot w_0 \approx \frac{\lambda \cdot f}{\pi} \quad . \tag{4.11}$$

In the present experimental conditions, considering the radius of incident laser beam onto the off-axis parabola $w \approx 14\ mm$ [133], the minimum diffracted limited radius of the beam in the focal position is $w_{Gauss0} \approx 1.96\ \mu m$. From the Gaussian fit of the experimentally measured laser beam radial profile in the focus (see figure 4.4 b)), it was inferred a beam radius of $w_0 \approx 2.7\ \mu m$. Consequently, the quality of the laser beam focusability is in range of ≈ 1.4 times diffraction limited, in good agreement with previously reported measurements in [133, 134]. As mentioned above, knowing the minimum radius and using the formula 4.8, one may determine the Rayleigh length as $z_R \approx 28 \mu m$. In figure 4.4 a) and c) the radial laser beam profiles in the neighborhood of Rayleigh plans (at the coordinates $z_{1,2} = \pm 30\,\mu$m) are shown.

Note that the aperture of the off-axis parabola used in these experiments was $D = 76.5\ mm$ and so called *"99% criterion"* [121] is fulfilled. This criterion gives the diameter D_0 of an aperture which transmits 99% of the gaussian beam power as $D_0 = \pi \cdot w$. Moreover, the parabola aperture D is even larger than $D_m = 4.6 \cdot w$, the recommended minimum diameter of the aperture which assures that, by cutting at the aperture edge, the beam intensity pattern distortion will lead to an intensity variation $\Delta I/I$ less than 1% [121].

In practical terms, one may determine useful formulas which connect the measured quantities like spot diameter ($FWHM_I$), pulse duration (τ_L) or pulse energy ($\mathcal{E}$) with important laser parameters like peak and average intensity or fluence of the laser. The intensity of a Gaussian beam is rapidly changing after the focussing

element due to the beam radius variation along the laser propagation axis (equation (4.6)). For a laser pulse characterized by the optical power, $\mathcal{P} = \mathcal{E}/\tau_L$, one may derive a practical formula for the peak intensity I_0 along the optical axis integrating the radial profile of the laser beam over the beam spot area as follows

$$\mathcal{P} = \int_0^\infty I(r) \cdot 2\pi r dr = \int_0^\infty \frac{\epsilon_0 \cdot c}{2} \cdot E_0^2 \cdot e^{-2(r/w_0)^2} \cdot 2\pi r dr = \frac{\pi I_0 w^2}{2} \tag{4.12}$$

and then,

$$I_0(z) = \frac{2 \cdot \mathcal{P}}{\pi \cdot w(z)^2} \quad . \tag{4.13}$$

Consequently, the laser peak intensity depends on the measurable laser parameters as follows

$$I_0(z) = 4 \cdot ln2 \cdot \frac{\mathcal{E}}{\tau_L \cdot \pi \cdot FWHM_I^2} \quad . \tag{4.14}$$

Note that at the Rayleigh length from the beam focus, corresponding to the coordinates $\pm z_R$, the laser peak intensity drops by a factor of 2 from the value in the focus (experimentally proved with an accuracy of 6% by the beam profiles in the figure 4.4 a) and c)).

It is important to mention the relevance of the experimentally measured quantities, taking into account that the response of the detectors is a result of a spatial and temporal averages of the measured values. For example, the average intensity of the laser beam can be expressed as

$$\overline{I} = \frac{4 \cdot ln2 \cdot < \mathcal{E} >}{\tau_L \cdot \pi \cdot FWHM_I^2} \quad , \tag{4.15}$$

where $< \mathcal{E} >$ represents the average energy of one pulse deposited onto a detector integrated over the pulse duration τ_L (as the full width at the intensity half maximum in the time domain) and the spatial $FWHM_I$ of the beam. One can express the average energy as

$$< \mathcal{E} > = I_0 \cdot \int_{\psi=0}^{\psi=2\pi} \int_{r=0}^{r=FWHM_I/2} e^{-4 \cdot ln2\,(r/FWHM_I)^2} \cdot 2\pi\, r\, dr\, d\psi \int_{t=-\tau/2}^{t=\tau/2} e^{-4 \cdot ln2\,(t/\tau)^2} dt. \tag{4.16}$$

and thus, comparing the equations 4.15 and 4.16, the average intensity is given by $\overline{I} \approx 0.4 \cdot I_0$. For example, considering the measured parameters of the laser beam incident onto the target in the focal position as follows:

$$\mathcal{E} = 100\ \mu J,\ \tau = 8\ fs \text{ and } FWHM_I = 3{,}2\ \mu m$$

then the peak value of the laser intensity is $I_0 \approx 10^{17}\ W/cm^2$ and accordingly, the corresponding average intensity is $\overline{I} \approx 4 \cdot 10^{16}\ W/cm^2$.

4.2 Experimental set-up for the absorption measurements

The experimental investigations of the absorbed laser energy fraction by solid targets were performed with an experimental arrangement depicted in figure 4.3. The main component was an Ulbricht sphere which enclosed the target placed in the sphere center. The laser beam was coupled in to the sphere through an open port centered on the laser propagation axis.

In these experiments different types of targets were used including (1) mirror-flat metallic (*Aluminum* and *Gold*) layers with a thickness of $\approx 300\,\text{nm}$ thermally evaporated on planar silicon substrates, (2) *Boron Nitride (BN)* ceramic and (3) bulk *BK7 Glass*. The dimensions of these targets were $(20 \times 20 \times 2\,\text{mm}^3)$. The roughness of the metallic layers surface was estimated of about 2.5 nm and 500 nm for the BN target (see figure 5.10). The xyz-translation movement of the target was allowed by the target holder equipped with three motorized remotely controlled translation stages. The position of the target was controlled with an accuracy of $1\,\mu\text{m}$. The laser was operating in a single shot mode and the target was moved after each shot along the Oy axis in order to expose a fresh surface to the laser beam. The integrating (Ulbricht) sphere of 10 cm in diameter which had a number of open ports for the coupling of the incident pulse and of the diagnostics. The amount of laser light collected by the sphere was measured with a high-speed photodiode coupled to the sphere via an optical fiber bundle.

The experiments investigated the absorption process dependence on the laser incidence angle and on the laser polarization. For these purposes, two rotation stages were mounted at the target holder allowing the independent target rotation around the axis Ox and Oy with an accuracy of 1°. When the target was rotated around Oy axis, the laser pulse was focused on the target under different angles in p-polarization geometry, while the target's rotation around Ox axis allowed the laser beam incidence on the s-polarization geometry.

4.2.1 Integrating sphere and detectors

In order to determine the amount of absorbed energy fraction, the experimental set-up included the combination of an Ulbricht sphere and photodetector D_1 for measuring the reflected fraction of laser energy R (specular and scattered) by the target. The absorbed fraction A was determined from the formula: $A = 1 - R$. The inner walls of the integrating sphere were covered by a diffusive and high reflectivity Barium Sulfate ($BaSO_4$) paint and able to spatially integrate the reflected radiation flux. The important properties for a reflecting material to be used in an integrating sphere are a high reflectivity, long term stability and a Lambertian angular scattering distribution. The coating paint has a reflectivity $\rho_0 \gtrsim 95\%$ over a large wavelength range ($400 - 1200\,\mathrm{nm}$). The sphere geometry includes a number of $n = 3$ open ports of area S_i needed to admit the incoming laser beam and to provide access to the target holder and the diagnostics. The total area of the ports represents a fraction $f = \sum_{i=1}^{n} f_i = \sum_{i=1}^{n} S_i/S_s = 0.04$ from the sphere area, S_s. Considering the multiple reflections and losses through the opening ports, one may determine the average reflectivity by

$$\overline{\rho} = \rho_0 \left(1 - \sum_{i=1}^{n} f_i\right) + \sum_{i=1}^{n} \rho_i f_i \tag{4.17}$$

where ρ_0 is the sphere paint reflectivity, ρ_i is the reflectivity of the opening port i and f_i represents the fractional area of port opening i. Accounting for the particular geometry of the Ulbricht sphere used in these experiments, the average reflectivity is $\overline{\rho} \gtrsim 90\%$. The output radiation field is a convolution of the input radiation field with the time response of the sphere which is of the form e^{-t/τ_s}. The time constant τ_s is expressed by

$$\tau_s = -\frac{2}{3} \cdot \frac{d_s}{c} \cdot \frac{1}{\ln \overline{\rho}}, \tag{4.18}$$

where c is the speed of light and d_s is the sphere diameter. The estimated time constant is of the order of 2 ns. After several reflections on the inner surface of the sphere, the reflected radiation reaches the active surface optical bundle coupled to the sphere. In order to prevent high energy plasma radiation to reach the active head of the optical bundle, we used a 2 mm thick Schott OG550 glass filter with a window of transmission factor $T > 90\%$ for wavelengths larger than 600 nm.

The linearity of the sphere reflectivity was checked as a function of the incident laser fluence and found better then 3% for fluences up to $\approx 0.3\,\mathrm{mJ/cm^2}$. Accounting

for a maximum value of the average incident laser intensity of $5\times10^{16}\,\mathrm{W/cm^2}$, it was expected that the specularly reflected beam may reach an intensity $\lesssim 2\times10^{10}\,\mathrm{W/cm^2}$ at the sphere walls which corresponds to a laser fluence $\lesssim 0.2\,\mathrm{mJ/cm^2}$. This value is in the range of the linear response and, according to previous experimental studies [68], is below the damaging threshold of the coating paint estimated to be $\approx 0.8\,\mathrm{mJ/cm^2}$. The signal at the photodetector was proportional to the fraction R of the laser energy reflected from the target, specular and scattered. Previous experimental works (see, for example, [135, 136]) proved that the contribution of the diffusely scattered light is very small. The experimental investigations presented in this thesis do not include the measurement of the backscattered laser energy, as it represents less than 1% for incidence angles larger than 10° and thus, is negligible (see, for example, [139]).

The experimental set-up included also two photodetectors with 2 GHz bandwidth and internally biased for a rise time of 150 ps. The first one was used to measure the energy reflected by the target. It was mounted at the end of the optical bundle and gave signals in the range of $0 \div 1100\,\mathrm{mV}$. The second photodiode was collecting via an optical fiber a fraction of the light reflected by a 1 mm thick AR-coated quartz window (the transparent entrance for the laser beam into the compressor) and the signal was in range of $0 \div 1500\ mV$. This photodiode was needed in order to monitor the shot-by-shot laser energy fluctuations and showed less than 5% variation around the averaged value over tens of shots. The linearity of both photodetectors has been checked up to 2 V output signals and was found to be better than ±4%. In order to keep the incident radiation level within the linear response of the photodetector, a number of ND filters were used.

4.2.2 Data recording procedure

Although a large number of physical and geometrical parameters were monitored in these experiments, the recording data procedure was similar for all the configurations. The signal recorded by the photodiode (D_1) coupled by an optical bundle to the Ulbricht sphere (figure 4.3) is proportional with the energy reflected by the target at different z-positions of the target. The experimental results of a typical z-scan are shown in the figure 4.6 a) for an *Aluminum* target in p-polarization geometry at 30° incidence angle. The variation is symmetric around the focal position within the error bars and this behavior was observed essentially for all investigated incidence angles and target materials. The experimental data points were inferred averaging

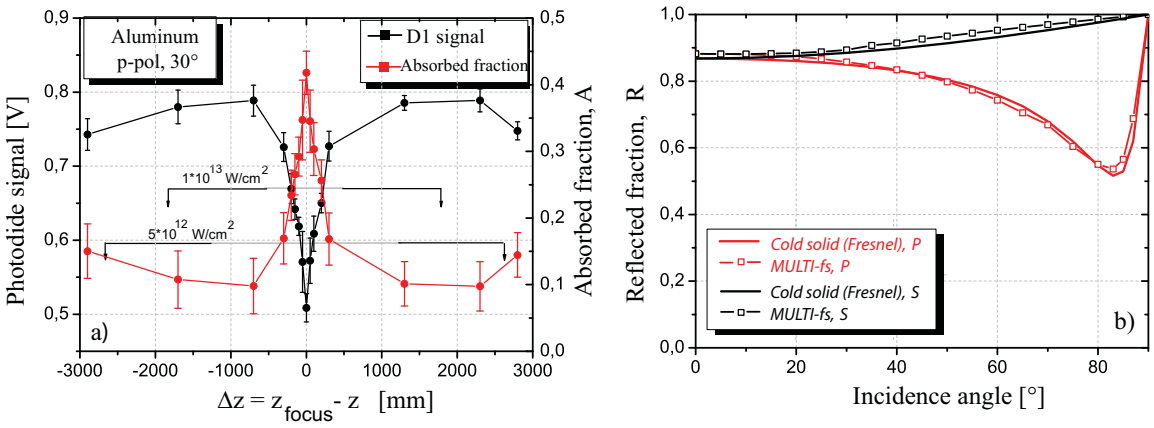

Figure 4.6: a) Typical photodiode signal and the corresponding absorbed energy fraction as a function of target position along the laser propagation axis Oz. The plots correspond to an *Aluminum* target irradiated by p-polarized laser beam under 30° incidence. The focal position corresponds to an average laser intensity of $5 \times 10^{16}\,\mathrm{W/cm^2}$; b) The reflected energy fraction calculated with MULTI-fs hydrocode and using Fresnel coefficients for *Aluminum* at room temperature.

the peak values of the photodiode signal over 10-20 shots. The variation of the z position of the target corresponds to different laser intensity at the targets. In the figure 4.6 a) a few average intensity values are specified (note that they correspond to the normal incidence).

In order to determine the absolute reflected fraction at different laser intensities, a reference value of the target reflectivity was required. In the case of the experiments presented in this chapter, an absolute calibration of the Ulbricht sphere was not possible *in situ*. The level of the energy transmitted through the optical bundle was lower than the detection level of the available energy meter (EPM1000 by Coherent, Inc.). Therefore, the photodetector signals were recorded, in general, at distances $z_{ref} \gtrsim 3000\,\mu\mathrm{m}$ (in the particular case presented in figure 4.6, $z_{ref} \approx 3300\,\mu\mathrm{m}$) where the laser pulse is characterized by intensities $I_{ref} \approx 4 \times 10^{12}\,\mathrm{W/cm^2}$, fluences $F_{ref} \approx 40\,\mathrm{mJ/cm^2}$ and with a diameter $FWHM_I \approx 400\ \mu m$. All the parameters have been estimated in a plane perpendicular to the propagation axis. The laser fluence $F_{ref} \approx 30\,\mathrm{mJ/cm^2}$ is below the damage threshold of the surface in sub-picoseconds regime for both kind of target materials investigated: conductors [13, 14, 21] and dielectrics [22] (see the analysis on the paragraph 3.1 for short pulses regime). Moreover, the laser-target interaction process (on a femtosecond time scale)

is faster than the energy transfer characteristic time $\tau_{e-i} = 1/\nu_{e-i}$ from electrons to ions and found to be in the order of ps [13]; ν_{e-i} represents the electron-ion collision frequency. Therefore, ions can be considered cold during the ultrashort laser pulse interaction and the target profile can be considered step-like. The microscope analysis of the target surface confirms the hypothesis of the non-damaged surface.

Although the ablation process is not possible at this laser fluence, one has to consider the changes induced by the laser heating process in the target parameters like electron temperature T_e and electron density n_e. These parameters influence the complex medium permittivity $\widetilde{\varepsilon}_r$ (see the Drude model described in [162] and the considerations in Appendix A) and consequently, the reflected fraction, R.

For determining the target reflectivity at the reference laser fluence corresponding to the coordinate z_{ref}, hydrodynamic simulations were carried out using the 1-D MULTI-fs code (for details of the physical model see [140] and Appendix B.2). These simulations were motivated by the fact that MULTI-fs can account for collisional ionization and heat transfer over a wide range of temperatures from cold solid to hot plasmas. In the simulations the input value of the laser intensity was $I_{ref} \approx 3 \times 10^{12}\,\mathrm{W/cm^2}$ similar to the experimental value at z_{ref}. At the laser peak, the temperature target on the surface was found to be $T_e \approx 30\,\mathrm{eV}$ and the electron density reached a maximum value of $n_e \approx 1,7 \times 10^{23}\,\mathrm{cm^{-3}}$. The reflected energy fraction R_{ref} calculated using the $MULTI-fs$ code was compared with the Fresnel coefficients R_{cold} for the reflectivity of a cold target at room temperature (refer to in Appendix A). Substantially the same reflectivity for all angles of incidence and for both polarization with an accuracy of 3% is found and the results are shown in the figure 4.6 b) for an *Aluminum* target. These results are in agreement with a similar analysis reported in [14].

Therefore, the photodiode signal recorded at z_{ref} was considered proportional to the reflected light energy by the target $S(z_{ref}) \sim E_{reflected}(z_{ref}) = R_{cold} \cdot E_{incident}$, where R_{cold} represents the reflectivity (Fresnel) coefficient of the cold target. For any position z of the target along the propagation axis, the reflected (R) and respectively, the absorbed (A) energy fractions were calculated as:

$$R(z) = \frac{E_{reflected}(z)}{E_{incident}} = \frac{S(z)}{S(z_{ref})/R_{cold}} \quad , \quad A(z) = 1 - R(z). \tag{4.19}$$

The recorded photodiode signal was evaluated using the peak value and the integration of the temporal signal profile and similar results were found for the inferred

absorption with an precision of 3%. The peak values of the photodetector signal were used in the evaluation of the data.

4.3 High resolution XUV spectrometer

A second experimental set-up was build for recording the spectra in the extreme ultraviolet (XUV) range emitted by plasmas produced by ultrashort laser pulses. The main part of this set-up consists in a high resolution, flat field spectrometer. The block view of the spectrometer and the geometrical layout are presented in figure 4.7. The photo of the spectrometer attached to the target chamber and a detailed view inside the target chamber are presented in figures 4.9 a) and b).

For a better collection of the radiation, the plasma emission was firstly imaged by a focussing system containing two spherical, identical mirrors arranged in Kirkpatrick-Baez design [100]. The mirror surfaces were coated with a gold layer of 300 nm thickness. The mirrors have a diameter of $\Phi = 7.6\,\text{cm}$ and a radius of curvature of $R = 8\,\text{m}$ and they are placed at $\approx 8\,\text{cm}$ distance between their centers. The reflectivity of metallic surface is enhanced in the soft X-ray spectral range if the radiation is incident onto angles smaller than so-called *critical angle* θ_c. The critical angle depends on the real part of the metal refractive index n as follows: $\cos\theta_c = 2 - n$, where $n = 1 - \sqrt{n_e e^2 \lambda^2 / 8\pi^2 \varepsilon_0 m_e c^2}$ (compare with formula 8.5) [101]. Here, n_e is the metal free electron density and λ is the X-ray wavelength. Consequently, the gold coated mirrors were mounted at grazing incidence of $i = 1.8°$, value below the critical angle for all the radiations in the spectral range of $1 - 20\,\text{nm}$

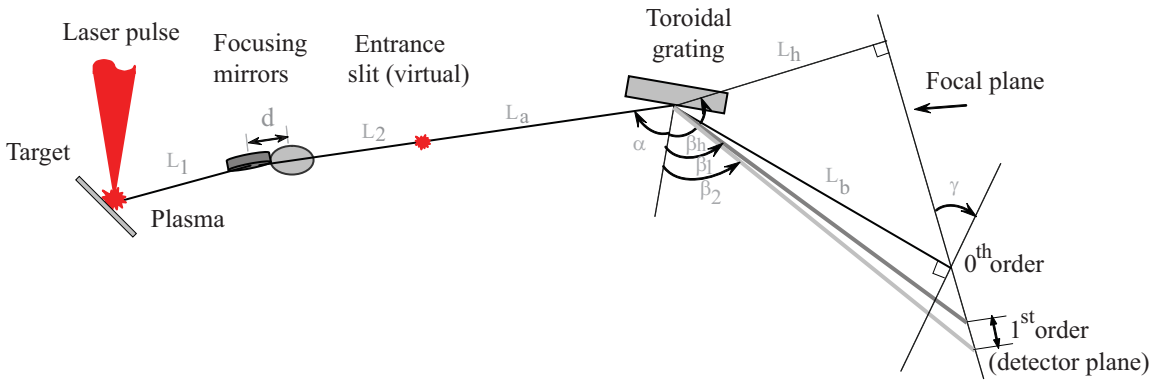

Figure 4.7: Optical layout of the flat field XUV spectrometer

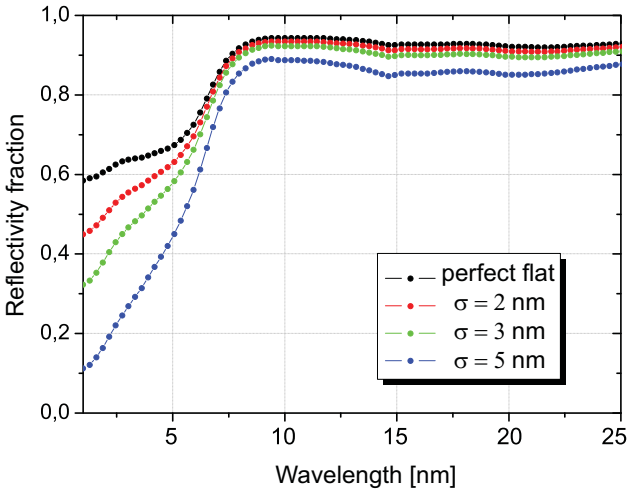

Figure 4.8: Reflectivity of 300 nm gold layer in XUV range. The calculations account for an incidence angle of 1.8° of the soft X ray radiation onto a perfect flat surface and with different roughnesses.

of interest for the present experiments. An important parameter which can affect the reflectivity and thus, the efficiency of the radiation collection is the mirror surface roughness σ [101]. In figure 4.8, the influence of the roughness on the mirrors' reflectivity is presented for radiation with wavelength in the range $(1-25)$ nm. The calculations account for an unpolarized radiation at grazing incidence angle $i = 2°$ (from http://www-cxro.lbl.gov/). For a perfect flat surface ($\sigma = 0$), the reflectivity decreases significantly in the small wavelength range ($\lambda = (1-5)$ nm). If the effect of the surface roughness is included in the calculation, the reflectivity of a rough surface R_σ is reduced compared to that of a perfect flat one $R_{\sigma=0}$ according to formula [101]:

$$R_\sigma = R_{\sigma=0} \cdot \exp\left[-\left(\frac{4\pi\sigma \sin i}{\lambda}\right)^2\right]. \tag{4.20}$$

The mirror surface was analyzed by an AFM technique (refer to paragraph 5.6 and figure 5.10) and the roughness of mirror surfaces were estimated to be about 2 nm. At this roughness value, in the small wavelength range, the mirror reflectivity decreases by a factor of 2. Altogether, the 2-mirrors focusing system increases the collecting efficiency by increasing the solid angle for the collected radiation by a factor of ≈ 4. The meridian focal length of the spherical mirror is given by $f = R \cdot \sin i/2$ and, within the spectrometer set-up, the mirrors were positioned ($L_1 = L_2 = 230$ mm, $d = 80$ mm) in such a way that both meridian focal plans were found on the same coordinate along the optical axis. Each mirror images the emitting plasma in the focal plane which coincides with the spectrometer entrance plane (no additional slit has been included). The magnification of the focussing system is $M \approx 1$.

The diffractive element used in the spectrometer is the aberration-corrected

toroidal flat-field grating with a varied line spacing manufactured by Horiba Jobin Yvon GmbH. The toroidal grating combines the properties of an off-axis focusing toroidal reflective surface with the dispersive properties of a grating. The toroidal grating images the spectrum of the 1^{st} diffractive order onto a plane [102]. This feature enables the spectrum to be recorded onto planar detectors (CCD cameras, MCP plates or films). The variable line spacing is defined by a polynomial function and results in an enhanced efficiency of the first order of diffraction and strong suppression of higher orders. In the present experiments two gratings have been used: the first (1), with an effective groove spacing of $n_1 = 384\,\text{lines/mm}$ for the $(100 - 250)$ Å spectral range, and the second (2) one, with $n_2 = 2400\,\text{lines/mm}$ covering the spectral interval $(16 - 40)$ Å. The gratings' geometry is identical allowing the same set-up of the spectrometer for both diffraction gratings. According with the notations in the figure 4.7, the optical geometry is defined by the following parameters: incidence angle $\alpha = -86.2°$, detection angle $\beta_h = 135.5°$, entrance length $L_a = 586\,\text{mm}$, perpendicular distance to the spectral plane $L_h = 685\,\text{mm}$, effective exit focal length $L_b = 1105\,\text{mm}$ and inclination of the spectral plane $\gamma = 51.7°$.

The linear dispersion for the k^{th} diffraction order at the central wavelength λ_0 is defined as $d\lambda_0/dx = (\cos\beta_0 \cos^2\gamma)/(knL_h)$, where β_0 is the diffraction angle of wavelength λ_0 and n is the groove density [103]. In the first order, the linear dispersions of the gratings were estimated of about $(d\lambda_0/dx)_1 \approx 0.2\,\text{nm/mm}$ and $(d\lambda_0/dx)_2 \approx 0.03\,\text{nm/mm}$, respectively. Another important grating parameter is its resolving power $R = \lambda/\Delta\lambda$ which can be theoretically defined by $R = D \cdot (\sin\alpha + \sin\beta)/\lambda$, where D is the width of the grating [101, 103]. For the gratings used in the experiment, the theoretical revolving power was estimated at the central wavelength of the corresponding spectral range of about $(\lambda/\Delta\lambda)_1 = 4 \cdot 10^4$ and $(\lambda/\Delta\lambda)_2 = 3 \cdot 10^5$, respectively. The spectral resolution achieved in the experiment was smaller than the theoretical estimations and was limited by the resolution of the detectors used for spectral recording (see below).

In these experiments XUV emission spectra were recorded employing two types of detectors accounting for their particular advantages: an intensified X-ray CCD camera (Proscan GmbH) and Imaging Plates (Fuji). In figure 4.9 c), examples of LiF emission spectra recorded with both detectors are shown. The X-ray camera consists of a phosphor (P47) screen as X-ray convertor coated with an 100 nm aluminium layer. The screen is coupled by an optic fiber bundle to a 40 mm microchannel plate as light intensifier. The CCD camera chip has a total number of 2048×2048 pixels

and the pixel size is $14 \times 14\,\mu m^2$. In recording spectra, one can benefit for the high sensitivity and intensification capabilities of CCD camera but one of its disadvantages is the reduced recording area. Moreover, the strict geometry of the toroidal grating imposes a well defined detector position and therefore, is not possible to scan online larger spectral ranges than the camera allows. The spectral resolution of the spectra recorded with the CCD camera was estimated of $\lambda/\Delta\lambda = 300$ at 17 nm for the 384 lines/mm grating. The Imaging Plates (IPs) are flexible radiation sensors containing specifically designed phosphors that trap and store the radiation energy [104]. IPs have been designed for the detection of accelerated particles (electron, protons, ions) and radiation in X-ray range but were also used with success in XUV range. Compared with the CCD X-ray camera, the IPs present the advantage of a large recording area but reading out is required after each detection procedure. The resolution of the IPs is limited by the dimension of the phosphor crystals (in the experiment IPs with granulation of $50\,\mu m$ were used). Thus, the spectral resolutions archived in the experiments with this detector were $\lambda/\Delta\lambda = 100$ at 17 nm and $\lambda/\Delta\lambda = 200$ at 2.5 nm for the grating of 384 lines/mm and 2400 lines/mm, respectively.

The target was mounted on a holder and its position was controlled and monitored in way similar to that described in paragraph 4.2. The laser pulses were focused at an angle of 45° incidence in *p*-polarization geometry with a 1 kHz repetition rate (if not stated otherwise). The target was constantly moved during the spectra recording. The optical axis of the spectrometer corresponds to the direction of the specularly reflected laser beam. All spectra recorded in these experiments have been time integrated over a large number of shots which depends on the target type and detector sensitivity. For example, at 1 kHz laser repetition rate, the spectra recorded on the CCD camera are time integrated for about 200 seconds while for spectra recorded on IPs the integration time was larger by a factor of 10.

Prior to each experimental session, the optical alignment of the spectrometer was checked using a *He-Ne* laser. The alignment laser is focused onto a high reflectivity target and its optical path was similar with that of the sub-10 fs laser pulses . Although the spectrometer alignment can be demanding due the particular characteristics of the optical components (focusing mirrors and toroidal grating) like grazing incidence and precise optical geometry, there are two important checking points along the optical path which can prove the correctness of the optical adjustment. Firstly, the correct position and orientation of the focusing mirrors were

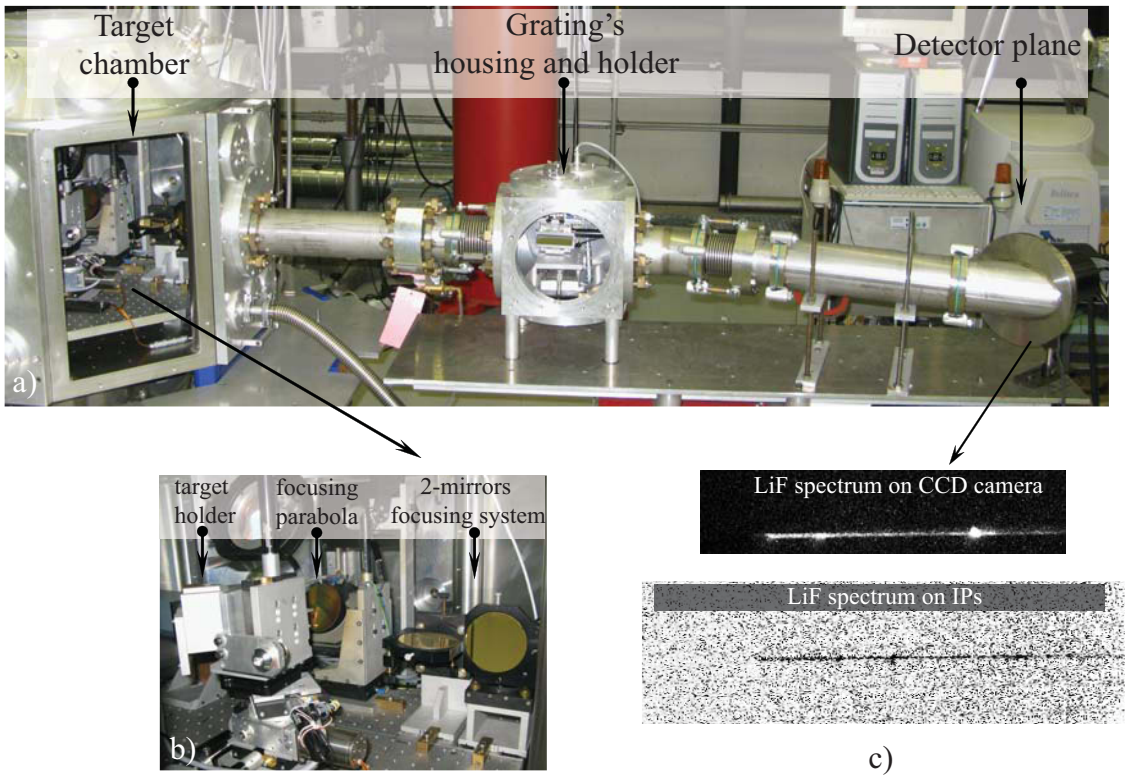

Figure 4.9: Photo *a)* present the XUV spectrometer mounted at the target chamber. The main components are indicated. Details of the experimental arrangement inside of the target chamber are shown in photo *b)* including the focusing parabola, target holder and focusing mirrors system. The images of the LiF recorded spectra on CCD camera chip and on Imaging Plates are presented in photos *c)*.

determined analyzing the image quality of the focal spot (focalization and magnification) at the entrance plane on the spectrometer. Secondly, the toroidal grating's alignment can be checked by the focused 0^{th} of the He-Ne laser beam on the detector plane. In both cases, 12-bit CCD camera placed at the required position and perpendicular on the optical axis was employed for these purposes.

Chapter 5

Absorption measurements and numerical simulations

As discussed in section 3.3.3, a new interaction regime is opened by the availability of sub-femtosecond, high contrast laser pulses as used in the experiments reported in this thesis. The experimental investigations reported in this chapter are motivated by the need of understanding the physical phenomena involved in the laser energy transfer to overdense plasma with insignificant hydrodynamic expansion.

In this chapter, the measurements of the absorption fraction of 8 fs laser pulses by different types of solid targets, in different geometries are reported. The dependence of the absorbed fraction on different parameters like, laser intensity and polarization, incidence angle is in detail investigated. For targets with an initial flat mirror surface, an efficient absorption up to 80% in the *Aluminum* case was observed. The absorption of the p-polarized laser pulses has an impressive preponderance on s-absorption. Computer simulations were performed modeling the interaction of the ultrashort laser pulses with an overdense plasma state with various steep profiles. The simulation results are consistent with the experimental observations for a plasma profile of $L/\lambda \approx 0.01$. The influence of the target surface roughness in the absorption process was investigated for a BN target and the results are in agreement with previous experiments on X-ray emission and hot electrons production.

5.1 Dependence of the absorbed energy fraction on physical parameters

The theoretical models presented in chapter 3.3 emphasize a number of specific dependencies of the absorbed energy fraction on different parameters according to the interaction regime (preformed plasma, laser intensity or pulse duration). For example, in the intensity range similar to the present experiment, in the presence of an expanded preplasma, the resonance absorption process shows a characteristic dependence on laser polarization, s and p, and on the preplasma scale length [70, 71]. As a general practice in the laser energy absorption measurements, the dependencies of the absorption onto various parameters were investigated and consequently, to identify the dominant absorption process in the specific experimental conditions (see for example [68, 108, 116]).

The experimental measurements reported in this chapter represent an extensive study of the absorption process of sub-10 fs laser pulses on solid targets. We investigated the dependencies of the absorbed energy fraction on the following parameters:

• *Incidence angle.* The angular dependence of the absorption was analyzed in the range of (10°-70°) for all investigated target materials.

• *Laser intensity.* For each incidence angle and for all targets materials, the influence of the laser intensity on the absorption process was experimentally investigated. The intensity scan covered a range of values from $5 \times 10^{12}\,\mathrm{W/cm^2}$ up to $5 \times 10^{16}\,\mathrm{W/cm^2}$.

• *Laser beam polarization.* The laser pulses were focused onto the targets in both polarizations geometry, p and s.

• *Target material.* We studied the energy transfer efficiency from the laser pulse to different types of target materials: conductors (*Aluminum*, Z_{Al}=13 and *Gold*, Z_{Au}=79) and insulators (*Boronsilicate Glass (BK7)* and *Boron Nitride*, $Z_{BN} = 13$).

• *Target surface roughness.* The role of the target surface flatness in the absorption process was analyzed and a comparison between the experimental results representing of the absorbed energy fraction by flat-mirror targets (*Gold*) and rough targets (*BN*) was performed.

5.2 Angular and polarization dependence

5.2.1 Experimental results

In figure 5.1 *a*) - *c*) the experimental results of the angular dependence of the absorbed energy fraction of laser pulses in both polarization geometry, *s*- and *p*-, incident onto three distinct target materials are presented. The target surface had a roughness of about 2.5 nm. The measurements were performed at an average laser intensity of $3 - 5 \times 10^{16}\,\mathrm{W/cm^2}$ corresponding to the target position in the laser focus. The experimental points have been determined as an average over more than 20 shots and the standard deviation of the calculated absorption fraction was $15 - 20\%$.

For *Aluminum*, *Gold* and *BK7* one may identify a similar angular dependence of the absorption fraction. For example, for the *Aluminum* target, in the case of s-polarized laser beam, while the angle of incidence θ is increasing, the absorption drops from $\approx 20\%$ at $\theta = 15^\circ$ to $\approx 5\%$ at $\theta = 70^\circ$. Absorption of the p-polarized laser light increases for larger angles from approximately the same values as in s-polarization at small angles, reaching its maximum value of $\approx 77\%$ at 80°. For *Gold* and *BK7* targets a similar difference between the angular behavior for $s-$ and $p-$ polarization was identified and the same significant preponderance of absorption of the *p*-polarized pulses on the *s*-polarized case. Furthermore, for these two types of targets, the absorption percentage peaks also at higher incidence angles, in the *p*-polarized geometry, reaching at 70° an absorption fraction of 64% and 62%, respectively. Due to the experimental difficulty at grazing incidence (lateral partialy beam distortion by the finite target dimension), a maximum angle θ_{max} in the *p*-polarization case, was not distinctly observed but it can be assumed as being larger that 70°.

5.2.2 Simulations results for the angular dependence of the collisionless absorption process

In order to identify the physical processes responsible for the laser energy transfer and to interpret the experimental results reported in this chapter, the interaction process was simulated by the help of *Plasma Simulation Code PSC* [105]. Details regarding the simulation geometry and initial parameters are presented in Appendix B.1. In the simulations, the interaction of a 10 fs laser pulse obliquely incident onto a plasma slab of a steep vacuum-matter interface was modeled. The simulation set-up

geometry, as the evaluation data technique were following closely to the experimental configuration and measurement procedures described in paragraph 4.2. The laser energy absorption fraction was determined by reading out the Poynting flux of the electromagnetic laser field before and after reflection on the target surface. The contribution of the target micro-fields was avoided in the post-processing procedure of the simulation results. The numerical simulation have been concentrated on investigating the absorption fraction dependence on different parameters like angular dependence, laser intensity or target material, similar to the experiment.

As was previously discussed (paragraphs 3.3.1 and 3.3.2), the laser energy trans-

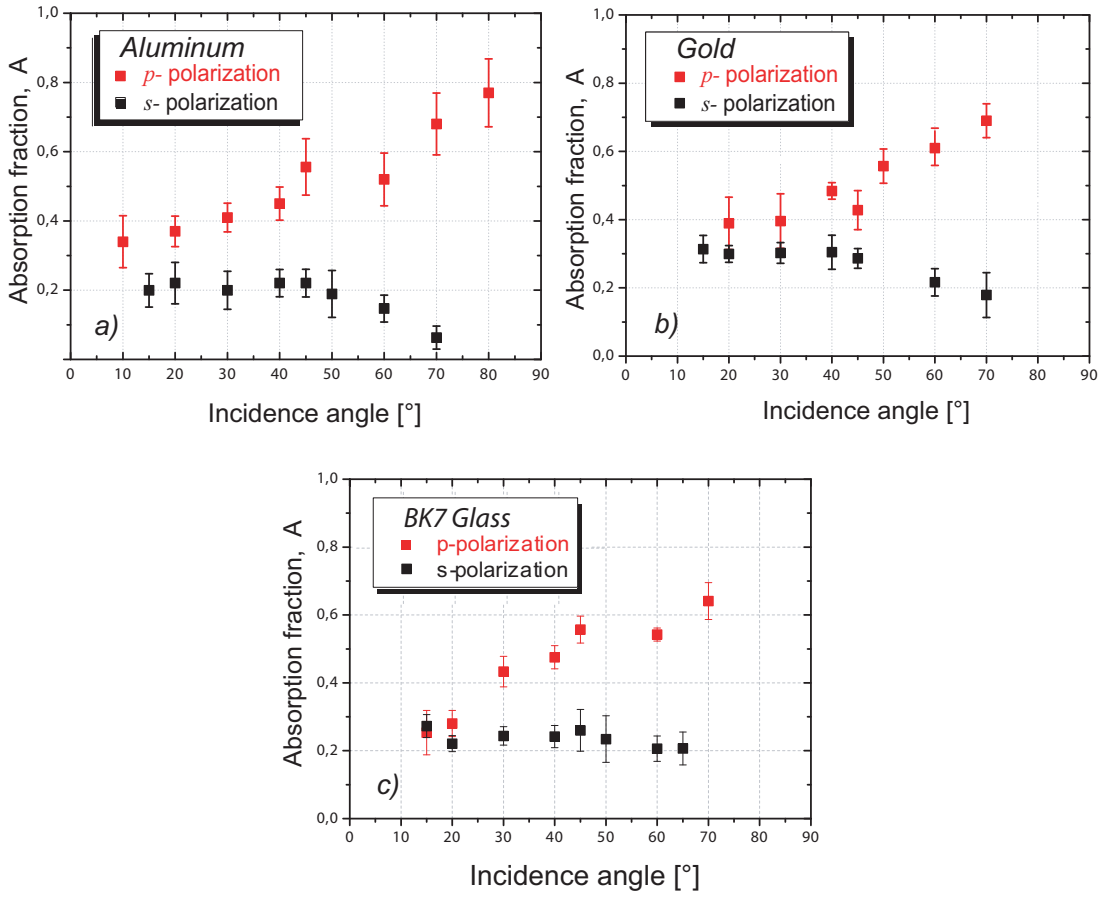

Figure 5.1: Experimental angular dependence of the absorbed energy fraction A of 8 fs, 790 nm laser pulses by different targets: *a*) *Aluminum*, *b*) *Gold*, *c*) *BK7 Glass*. The data points correspond to an average intensity of $5 \cdot 10^{16}\,\mathrm{W/cm^2}$ (in the best laser focus). The experimental results for both p- and s-polarization are displayed for each target material. The standard deviation of the data points is in the range of $15 - 20\%$

fer in the s-polarization geometry is governed by the collisional processes while in the p-polarization case both contributions, of collisional and collisionless processes, have to be considered. In order to calculate the contribution of the collisionless absorption, collisional absorption for s-polarization, A_s, was subtracted from the corresponding fraction A_p of the p-polarized beam. As mentioned above, in the code only the binary collisions are included which are described by their collision frequency $\nu_{ei} \propto Zn_e/T_e^{3/2}$ (equation 3.20). The target ionization is induced by the laser electric field. The collisional ionization module was not included in the simulations and, although the contribution of the impact ionization might be negligible for 10 fs interaction time [32, 57], the plasma's degree of ionization inferred from the simulation can be smaller than predicted by the theory (see paragraph 3.2). Nevertheless, the collisionless absorption fraction $A_p - A_s$ analyzed in the following paragraphs is assumed to be independent on the collisional processes. This assumption is supported in addition by detailed simulation tests where results of simulations have been compared the with and without the binary collision module included. Similar results were obtained with identical initial conditions. The target was obliquely oriented relative to the laser pulse over an angular range from 10° to 70°. Grazing incidence angles were not considered due to the finite dimension of the virtual target and lateral cut of the laser pulse, prior to reach the focal position.

In the following the simulation results for *Aluminium*, *Gold* and *BK7 Glass* targets will be presented and will be compared with the experimental data. At the vacuum-target interface various density scale lengths L of 2 nm, 10 nm, 20 nm, 200 nm and 500 nm were considered. For each target material and each plasma profile simulations in p- and s- polarization geometry were performed. From the simulation results the collisionless absorption fraction $A_{collisionless} = A_p - A_s$ was determined. In the figure 5.2 the angular dependences of the collisionless absorption for *Aluminium*, *Gold* and *BK7 Glass* targets at different plasma scale lengths are shown. The experimental points shown in the graphs represent the values of similar substraction of the s-absorption from the p-absorption fraction at a laser intensity of $2 \times 10^{16}\,\mathrm{W/cm^2}$. The experimental data are well reproduced for profiles in range of $L = 10 - 20$ nm for all target materials. The small values of these plasma profiles, of the order of $\approx 1\%$ of the laser wavelength confirm the hypothesis of the laser pulse interaction with the overdense plasma suggested by the laser pulse parameters (contrast and duration) and by spectroscopic plasma investigations [144] (refer to paragraph 6.1.2). The results emphasize that the laser pulse is able to deposit its

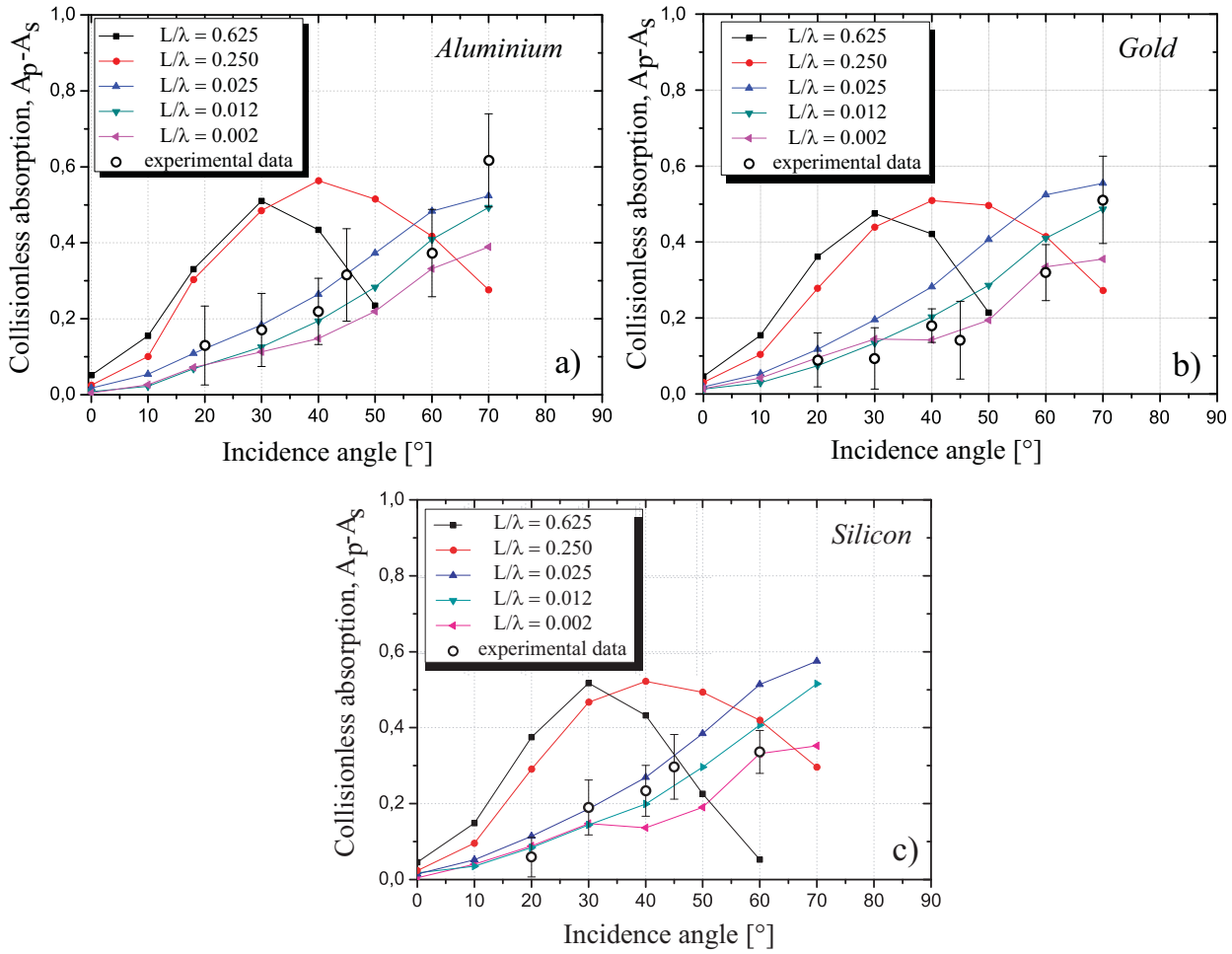

Figure 5.2: The contribution of the collisionless absorption on p polarization expressed as difference between absorbed fraction on p- and s-polarization for (a) *Aluminum*, (b) *Gold* and (c) *Silicon* targets interacting with a laser pulse of an average laser intensity $I = 2 \times 10^{16}\,\mathrm{W/cm^2}$ and wavelength $\lambda = 800\,\mathrm{nm}$. The experimental data are presented with open symbols. The *PIC* simulations results in the same laser condition and different pre-plasma scale lengths L/λ are shown with filled symbols.

energy in a significant fraction (up to $\approx 50\%$ at 70° incidence angle) via collective processes on the target of a density close to the solid. Additional simulations were performed for higher resolutions up to 120 cells per μm, but the results were not sensitive to the increased resolution.

The simulation results confirm the experimental observations regarding the similar angular dependence shown by conductor (*Al*, *Au*) and dielectric (*Glass*) targets. In the experiment, the prepulse may determine a local preheating of the target on a

picosecond and nanosecond time scale which may overcome the atomic binding energy ε_b for the target materials analyzed but no significant hydrodynamic expansion is expected (refer to the analysis in paragraph 3.1). Therefore, in the simulations the target was modeled in the solid state accounting only for the atomic density, atomic mass and the ionization potential of isolated atoms without including the lattice/neighbor ions influence (like potential lowering). The target was primarily ionized by optical field ionization according to *ADK* model [160] included in the code. For example, in the *Aluminum* target case the electron density and the average ionization state observed in the simulation were, respectively: $n_e \approx 2\times10^{23}\,\mathrm{cm}^{-3}$ and $Z^* \approx 3.5$ (in agreement with previous analytical estimations [84]).

Special attention was paid to the modeling of dielectric targets. *BK7 Glass* is a dielectric compound (borosilicate glass) having as the main constituents silicon and boron oxide ($Si \approx 30\%$, $O \approx 50\%$, $B \approx 5\%$) with the average atomic density of $n_n \approx 6 \times 10^{22}\,\mathrm{cm}^{-3}$ and a mass density of $\rho \approx 2,23\,\mathrm{g/cm}^3$. The first ionization potentials of these elements are 8.1 eV and 13.6 eV for *Si* and *O*, respectively. Different simulations have been performed modeling a *Silicon* and an *Oxygen* target. The absorbed fraction calculated for these two different targets leads to similar values within an average deviation up to $\approx 20\%$. In figure 5.2 c) the simulation results for a *Silicon* target are represented showing a good agreement with the experimental data at steeper target profiles with $L/\lambda \approx 1 - 2\%$ in a similar range of values as in the conductor target case.

Figure 5.3 shows the electron density spatial distribution in an *Aluminum* target of profile $L/\lambda = 0.012$ irradiated by a p-polarized laser pulse under 40° incidence angle. In the simulation box, the electron density right after the end of the laser pulse interaction with the target (which corresponds to $t = 90\,\mathrm{fs}$ from the start of simulation) is presented. In this case a maximum electron density of $1.8\times10^{23}\,\mathrm{cm}^{-3}$ was observed. The target coordinates are attached to the simulation box. In the right side plot the electron density distributions along z_t axis at different moments of the interaction are shown: at the laser peak ($t = 70\,\mathrm{fs}$), at the end of the interaction ($t = 90\,\mathrm{fs}$) and after the pulse left the simulation box ($t = 110\,\mathrm{fs}$). The electron density is normalized to the critical density $n_{cr} \approx 1.7 \times 10^{21}\,\mathrm{cm}^{-3}$ for 800 nm wavelength. In general, for all materials investigated the ionization processes lead to a target state of about 100 times overdense.

The agreement of the simulated absorption angular dependence with the experiment data occurs for a plasma scale length in the order of the skin depth of the

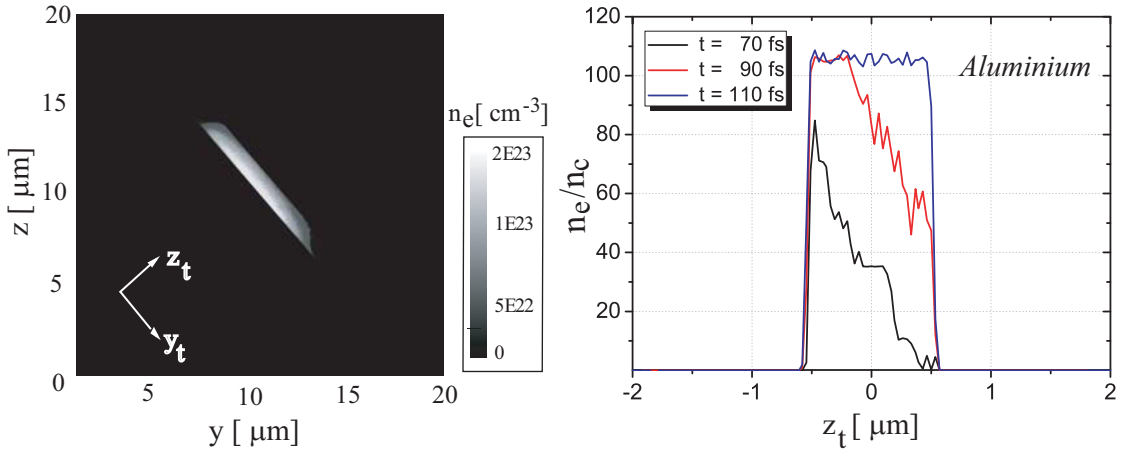

Figure 5.3: Electron density spatial distribution during the interaction with 10 fs laser pulses incident under 40° onto an *Aluminium* target with a profile $L/\lambda = 0.012$. *Left*: the snapshot of the simulation box in the *0yz* plane after the interaction with the laser pulse. *Right*: The normalized electron density along the direction perpendicular on the target at different times.

studied materials. Using the formula 3.1 one may estimate the skin depth in solid state in the order of $l_{s,Al} \approx 10\,\text{nm}$ for *Aluminum* and $l_{s,Au} \approx 5\,\text{nm}$ for the *Gold*. The expansion of the target estimated as Δz_t along the axis perpendicular to the vacuum-target interface during the interaction with the 10 fs laser was below the spatial resolution considered in the simulations indicating a negligible hydrodynamic rarefaction of the front layers of the target.

The simulation results led to the conclusion that the angular dependence on the collisionless energy absorption is independent on the initial state of the target as conductor or dielectric at the laser intensity of $5 \times 10^{16}\,\text{W/cm}^2$. As an effect of ultrafast field-ionization and energy transfer, the interaction of the 10 fs laser pulse takes place with an overdense target with an electron density in the range of $1 - 2 \times 10^{23}\,\text{cm}^{-3}$ irrespective of the initial state of the material. The high contrast laser pulse and ultrashort interaction time scale leads to an insignificant plasma expansion of few a percents from the laser wavelength, proved by simulations for all targets.

5.3 Absorbed fraction *vs* laser intensity

5.3.1 Experimental results

Theoretical models and numerical simulations predict a specific dependence for different absorption mechanisms on the laser intensity, like collisional absorption [2, 61], vacuum heating [79, 86] or collisionless skin effect [93, 97, 99]. In the experimental investigations, these dependencies have been considered as "signatures" for the particular mechanisms (e.g. [62, 108, 136]). In the experiments presented in this thesis, the variation of the absorption with the laser intensity was investigated performing z-scan measurements along the laser propagation axis using the procedure described in the paragraph 4.2.2. The metallic targets investigated in this experiment (Al, Au) present similar dependence function of the absorption fraction *vs* the laser intensity I_L and similar threshold behavior for the significant increase of the absorption. The relevant experimental results are shown in figure 5.4 a) - d). The intensity scan covered 4 orders of magnitude, from $5 \times 10^{12}\,\mathrm{W/cm^2}$ up to $5 \times 10^{16}\,\mathrm{W/cm^2}$. In the high intensity regime ($5 \times 10^{14} - 5 \times 10^{16}\,\mathrm{W/cm^2}$) distinct scaling laws could be inferred depending on the polarization geometry. These specific dependencies and behaviors can be described for different laser polarizations as follows:

- *P-polarization.* Firstly, in the low intensity regime, the absorption fraction is almost constant over the intensity range ($5 \times 10^{12}\,\mathrm{W/cm^2}$ - $1 \times 10^{14}\,\mathrm{W/cm^2}$), at the same absorption level as in cold conditions (see figure 8.1). The onset of the absorption takes place at $\approx 1 \times 10^{14}\,\mathrm{W/cm^2}$ and increases with the laser intensity indicating a more efficient energy transfer process. From the positive slope of the graph, one may determine a characteristic scaling law $A_p \sim (I_L \cdot \lambda)^{\alpha_p}$ of the absorption fraction in the $p-$polarization case, A_p, where $I_L \cdot \lambda$ is defined as the laser irradiance. The value of the exponent $\alpha_p \approx 0.11 \pm 0.05$ indicated a weak dependence of the absorption fraction on the laser intensity, irrespective of the angle of incidence or conducting material.

- *S-polarization.* In this polarization case, for both conducting targets, a similar threshold behavior was identified around the intensity value of $\approx 1 - 3 \times 10^{14}\,\mathrm{W/cm^2}$. In the same manner as for the p-polarization case, the linear fit of the experimental data over 2 orders of magnitude of the intensity range reveal a specific scaling law which reads as: $A_s \sim (I_L \cdot \lambda)^{\alpha_s}$. The average value of exponent α_s was found $\approx 0.20 \pm 0.04$.

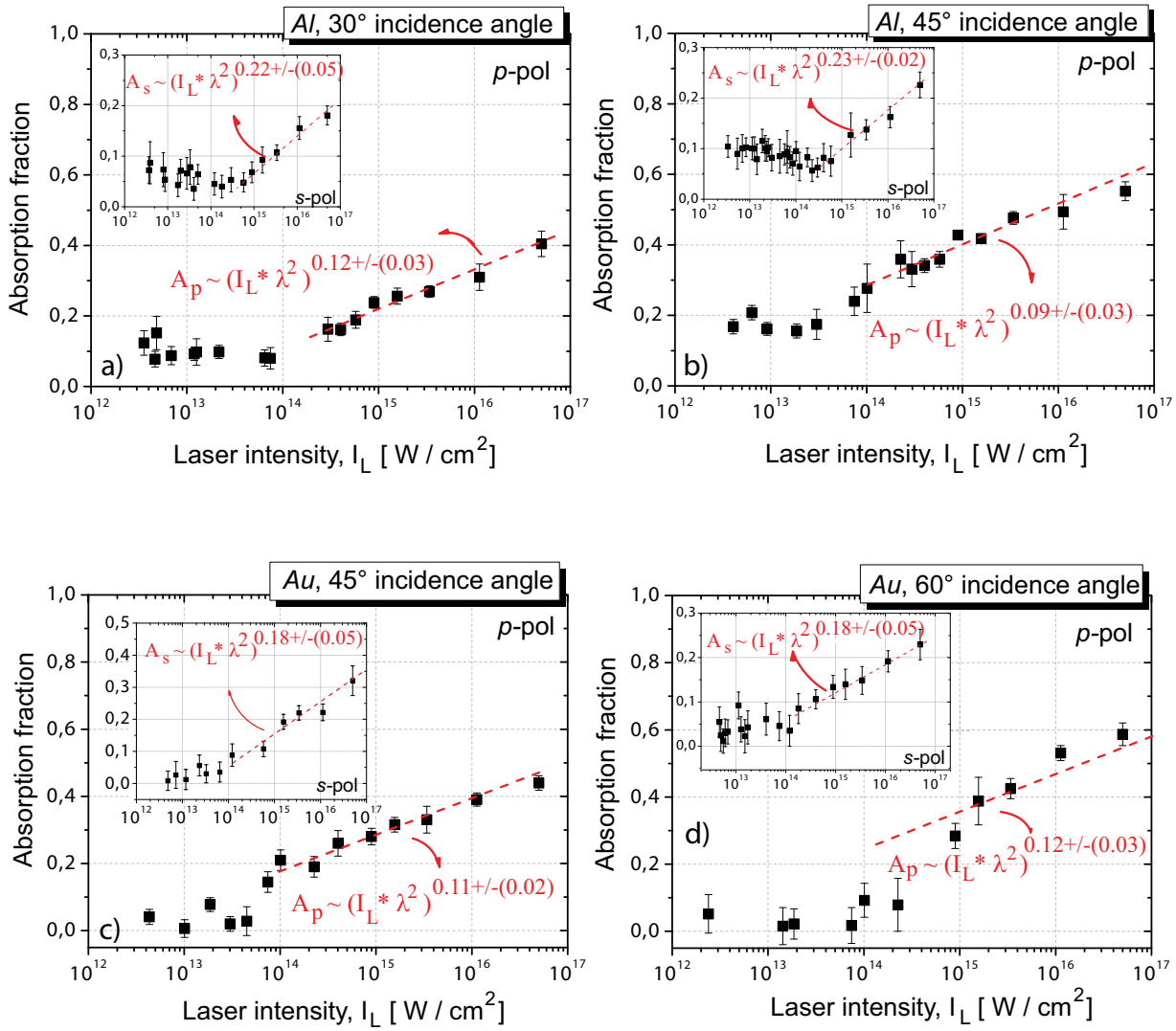

Figure 5.4: Experimental results of the absorption fraction dependence on the laser intensity of 8 fs laser pulses obliquely incident onto conducting targets. In the plots a) and b) the experimental data for an *Aluminium* target are shown and the plots c) and d) correspond to a *Gold* target. In the main frame the results obtained in *p*-polarization geometry at 30° and 45° incidence angles for the *Aluminium* target and respectively, at 45° and 60° for the *Gold* target are presented. In the insets, the corresponding experimental data are presented for *s*-polarization at the same incidence angles. For each case, the linear fit of the data points in the high intensity range ($5 \times 10^{14} - 5 \times 10^{16}$ W/cm^2) is presented by the dashed line. The scaling laws determined for the absorption fraction dependence on the laser intensity are shown for each fit.

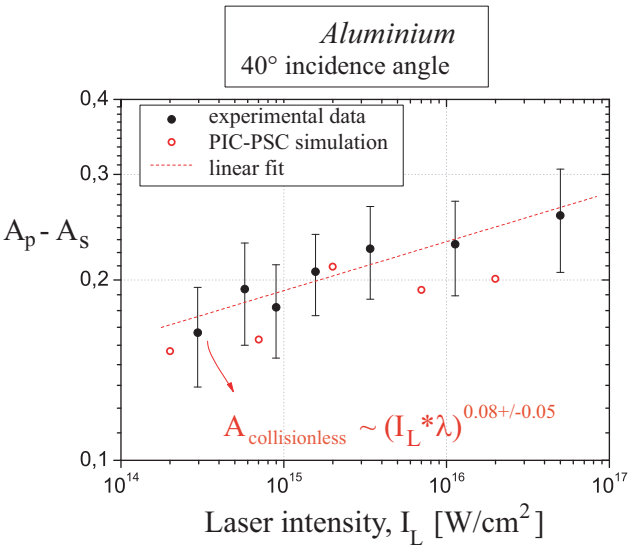

Figure 5.5: The dependence of the collisionless absorption fraction $(A_p - A_s)$ on the intensity of the laser pulse for an *Aluminium* target and 40° oblique incidence. The experimental data are shown with the filled circle symbols while the simulations are plotted with open symbols. The linear fit of the experimental data is represented by dash line.

5.3.2 Simulation results of the collisionless absorption *vs* laser intensity

The simulations performed using the *PSC* code allowed to investigate the dependence of the collisionless absorption level on the laser intensity in conditions similar to the experiment. The simulation box geometry and the input parameters were identical with those mentioned in Appendix B.1, except the laser input intensity which was modified in steps of $5\,\mathrm{W/cm^2}$. The angular dependence of the collisionless absorption contribution on the laser intensity I_L estimated from the experimental data $(A_p - A_s)$ is in good agreement with the simulation results. In figure 5.5 an example of this agreement for the *Aluminium* target at 40° incidence angle is presented. The collisionless absorption fraction shows a weak dependence on the laser intensity over the intensity interval analyzed. An arbitrary scaling dependence can be determined in the form $(A_p - A_s) \sim (I_L \cdot \lambda)^{\alpha}$, where $\alpha = 0.08 \pm 0.05$. The simulations were limited to the intensity range from $2 \times 10^{14}\,\mathrm{W/cm^2}$ up to $2 \times 10^{16}\,\mathrm{W/cm^2}$. In the interaction regime of the laser intensities $I_L < 1 \times 10^{14}\,\mathrm{W/cm^2}$, the simulation results might become questionable due to the physical model of the hot plasma considered in *PIC* codes. At lower intensities, the target is much colder and the initial distribution function of the charged particles (Maxwell-Boltzmann) included in the code becomes invalid to describe the binary interactions. In a cold solid target, the electrons, which are in the degenerated states interact with the lattice or with the phonons and are better described by a Fermi distribution [115, 140].

The experimental investigations reveal similar dependencies of the absorption

fraction on the laser intensity for *p*- and *s*- polarization respectively, in the range of moderate to high intensity ($5 \times 10^{12} - 5 \times 10^{16}\,\mathrm{W/cm^2}$) for *Aluminium* and *Gold* targets, regardless on the incidence angle, and the simulations confirm these observations. In [136], Price and co-workers have reported an experimental investigation of the reflectivity of a large variety of targets (conductors and dielectrics) irradiated by 120 fs laser pulse at normal incidence, over the laser intensity range between 10^{13} and $10^{18}\,\mathrm{W/cm^2}$. Above the intensity $\approx 2 \times 10^{14}\,\mathrm{W/cm^2}$ a similar dependence of target reflectivity on the laser intensity was observed for all materials investigated. This observation was explained by the collisional absorption process on an universal "plasma-mirror" state achieved by each target with a sharp interface. The collisional absorption is the main absorption mechanism, in the case of the experiment in [136] at normal incidence. The present experimental results, extended to the large oblique incidence angle, are in agreement with the results reported in [136] (refer to figure 5.4). In addition, the experiments confirm that the collisionless absorption works with the similar efficiency in the investigated laser intensity range ($5 \times 10^{14} - 5 \times 10^{16}\,\mathrm{W/cm^2}$) for both conductor targets.

5.4 Interpretation of collisionless absorption of sub-10 fs

In the following, the validity of different proposed collisionless absorption mechanisms in the present experimental conditions will be analyzed in the light of the simulation results. As was previously emphasized (paragraph 3.3.2), in the presence of a preformed plasma shelf of profile $L/\lambda > 1$, the absorption of a *p*- polarized laser pulse is often attributed to the mechanism of *linear resonance absorption*. Moreover, it has been shown that linear resonance absorption increases with shortening of the density scale length L and increasing angle of incidence [161]. The *PIC* simulation results presented in the figure 5.2 indicate the shift of the incidence angle for the optimum absorption towards to higher angles with the profile steepening. The results confirm the experimental observations of optimum angle with a value larger than 70°. In the case of longer profiles, the well known linear resonance absorption (*RA*) behavior is reproduced with an optimum absorption angle at intermediate values. The angular absorption for profiles of $L/\lambda = 0.25$ and $L/\lambda = 0.5$ emphasize that the code reproduces the particular characteristic of the *RA* in *WKB* approximation [71] for the optimum angle described by the relation: $\theta_{opt} = \arcsin[0.8(kL)^{-1/3}]$. The

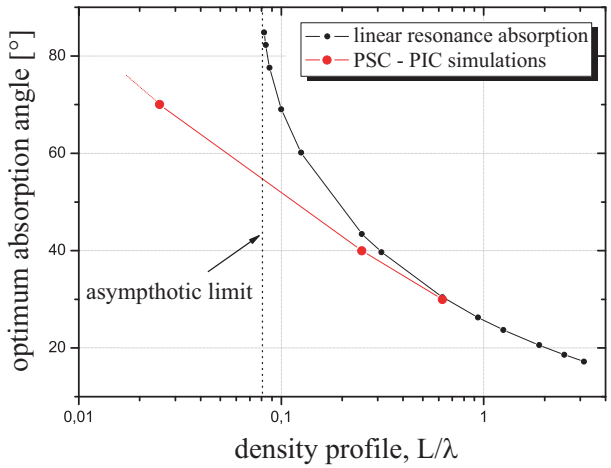

Figure 5.6: The comparison between the calculation of the incidence angle at the optimum absorption depending on the normalized plasma density profile L/λ from the linear theory of the resonance absorption and the *PIC* simulation results. For details regarding the asymptotic limit of the linear theory, see in the text.

comparison between the results of the *PIC* simulation and the resonance absorption prediction of the optimum angle is shown in the figure 5.6. The slight difference observed for the profile $L/\lambda = 0.25$ might be explained by the profile shape which is assumed to be linear in the *RA* theory while in the simulations the profile is described by the function 8.11. The linear theory has an asymptotic limit at a profile of about $L/\lambda \approx 0.08$ which corresponds at grazing optimum angle ($\theta_{opt} \rightarrow 90°$); below this value the resonance absorption fails to reproduce the experimental observation. This aspect was previously mentioned by different experimental groups [68, 113, 135] and nonlinear processes occurring in the plasma resonance region [157, 158] or other collisionless mechanisms have been considered involved in the laser energy transfer process [79, 93, 99]. The value of the density profile $L/\lambda \approx 1\%$ which results from the agreement with the experimental data does not corresponds to the linear regime of the resonance absorption. Moreover, the interaction region, over a thickness in order of the skin depth ($5 - 10\,\text{nm}$), is highly overdense and the shelf at the critical density plane is too thin for a resonant coupling of the laser to the plasma.

In the nonlinear regime, the model of *anharmonic resonance absorption* offers a possible explanation of the efficient coupling of the laser pulse energy to the overdense targets [72]. Although it is a new model and, partially, theoretical aspects are still to be worked out, the anharmonic resonance mechanism shows a couple of physical characteristics and properties which allow a comparison with our experimental regime and results. The absorption processes proposed by this model is more efficient, as all collisionless mechanisms, in p-polarization geometry and by, its amplitude-dependence resonance condition (3.31), allows the resonant laser coupling in target regions where the classical, linear resonant process is not valid. The thresh-

old behavior predicted by the anharmonic resonance model on the laser intensity for the process onset can be estimated only for a particular condition of one oscillating layer using the formula $I_L^{th} = (\varepsilon_0 c\omega_{p0}/2) \cdot \sqrt{m_e d/4e}$ (compare relations 2.15 and 3.32). Assuming a plasma frequency in the overdense state of $\omega_{p0} = 2 \times 10^{16}\,\mathrm{s}^{-1}$ and a layer thickness of $d = 0.12\,\mathrm{nm}$, the laser intensity threshold is about $10^{15}\,\mathrm{W/cm^2}$. In the experiment a similar threshold behavior was found, but this value is one order of magnitude larger than the corresponding value of $\approx 1 \times 10^{14}\,\mathrm{W/cm^2}$ experimentally found. This estimated threshold is expected to be lower when one consider the more realistic case of many oscillating layers, but an analytical approach of this case in not available and consequently a comparison with the experiment is not possible at the moment.

Another collisionless process analyzed in the context of the present experimental regime and results is *vacuum heating*. The laser energy is transferred to electrons while they are accelerated out of the target during one optical cycle and returned back to the target. The process is effective when the plasma profile is smaller than the electron quiver amplitude $x_q = eE/m\omega_L^2$ (2.17). The vacuum heating was identified as contributor or dominant absorption process in different experimental works in a similar intensity range with the present experiment [89, 108, 111]. In the present experimental conditions and according to the simulation results, one can assume a plasma profile of $L \approx 10\,\mathrm{nm}$. At the laser peak intensity, the electrons may achieve an excursion amplitude in the laser field larger than this value. In [86] a detailed analysis of the vacuum heating mechanism and its dependence on the plasma profile, L was performed via *PIC* simulations. For a laser intensity of $1 \times 10^{16}\,\mathrm{W/cm^2}$ and a plasma profile of $L/\lambda = 0.01$, the contribution of the vacuum heating process to the laser absorption was found to be very small, with a maximum of $\approx 10\%$ at 45° incidence angle. This value is smaller than the collisionless absorption determined in our experiment by a factor of $2 - 3$ for the investigated targets. The small contribution of this absorption mechanism, in conditions similar with present experiments, predicted by *PIC* simulations in [86] was explained in the context of the steep plasma profile by the small penetration of the laser field in the target and consequently, by the reduced number of electrons available for acceleration in the laser field. Moreover, vacuum heating presents a couple of characteristics resulting in specific scaling laws which are different from the corresponding ones found in our experiment. For example, in the context of the vacuum heating model, the absorption fraction scales with the laser irradiance as $A_{VH} \propto (I_L \cdot \lambda^2)^{0.5}$ ([79, 86]) while

from the present experimental results a dependence $(A_p - A_s) \propto (I_L \cdot \lambda^2)^{0.10\pm0.05}$. This mismatch between the specific vacuum heating scaling laws and our experimental results, leads us to the conclusion that vacuum heating is not the dominant mechanism in the present experiment. Moreover, worthwhile to emphasize is the effect of ultrashort pulse duration of our pulse ($\approx 8\,\mathrm{fs}$) compared with the previously mentioned experiments ($\tau_L > 100\,\mathrm{fs}$). In our case, the condition $L < x_q$ occurs for intensities above $5 \times 10^{15}\,\mathrm{W/cm^2}$ which corresponds to an interaction time of only $\pm 2.5\,\mathrm{fs}$ thus reducing to about one cycle pulse the interaction time in the vacuum heating conditions. Consequently, this model's contribution might be expected to be small and was it not possible to be distinguishable from our experimental results.

When the thermal effects on the plasma skin layer becomes important, the transfer of the laser energy to the target is explained by one of the collisionless skin effects, namely *anomalous skin effect* (*ASE*) and the *sheath inverse bremsstrahlung* (*SIB*). The validity domains of these models are defined by the relationship between the mean thermal excursion length of the electrons during one laser cycle and the skin depth (3.1), namely $\omega_L^2 c^2 \ll \omega_p^2 v_e^2$ for *ASE* and $\omega_L^2 c^2 \gg \omega_p^2 v_e^2$ for *SIB*. Let us consider this condition for the interaction of $5 \times 10^{16}\,\mathrm{W/cm^2}$ laser pulse with an *Aluminum* target. The physical parameters of the target considered in the following estimations are $\approx 1.8 \times 10^{23}\,\mathrm{cm^{-3}}$, $Z^* = 3$ and $T_e = 200\,\mathrm{eV}$ and they are determined from the data analysis of *PIC* simulations and emission spectra evaluations. Accounting for these parameters values, $(\omega_p/\omega_L)^2(v_e/c)^2 = 0.01$ indicating that the interaction regime lays in the domain of the sheath inverse bremsstrahlung process. Assuming the plasma parameters mentioned above, the contribution of the *SIB* process is smaller than 5% according to the formula 3.36. The *PIC* simulation results from [94, 95] confirm this estimations.

Summarizing, we analyzed the absorption mechanisms proposed up to date for the interaction regime of the ultrashort laser pulses with overdense, steep gradient plasma and the following conclusions can be mentioned. Accounting for their validity criteria and analytical estimations, different absorption mechanisms have been identified which may contribute to the energy transfer process, like the vacuum heating and sheath inverse bremsstrahlung. In both cases their estimated contributions were found to be too small compared to the experiment. In the vacuum heating case, its contribution to the total level of absorption and the specific scaling law of this mechanism are not clearly identified in the experimental results. The angular dependence of collisionless absorption fraction, experimentally determined, shows

an optimum absorption angle larger than 70°. This behavior is similar to the angular dependence in the case of resonance energy transfer process but in the present experimental conditions (a steep gradient $L/\lambda \approx 1\%$ of highly overdense plasma) the linear regime of this model in not valid. The model of the anharmonic resonance absorption extended the theoretical approach of the resonance absorption to the nonlinear regime. Although the theoretical analysis is currently in progress, we recognize the potential of this model to offer an alternative of the resonance coupling of the laser to the overdense plasma absorption in the nonlinear regime.

5.5 Collisional absorption in overdense plasmas with steep profiles

The experimental data performed in s-polarization geometry indicates the contribution of collisional absorption level in our interaction regime. The collisional absorption process depends on the plasma parameters, like electron density, temperature, and the plasma profile. In a general way, the collisional absorption fraction for a certain interaction regime can be determined solving the Helmholtz wave equations (3.24) for inhomogeneous plasma profiles, as it was shown in paragraph 3.3.1. In the long pulses regime and/or long plasma profile, the laser pulse loses its energy by collisional absorption propagating though underdense plasmas up to the critical surface. In this case, the *WKB* approximation is valid and the absorption fraction can be estimated analytically assuming particular plasma profiles (e.g. for an exponential profile, equation 3.30). In contrast, in steep plasma gradients the laser field penetrates only in the skin layer. For very steep plasma profile ($L/\lambda \ll 1$), the absorption fraction calculated from a solution of the wave equation is approximated by the Fresnel's coefficients (8.6) with an accuracy better than 5% (figure 3.1). The experimental data were compared with the collisional absorption fraction resulting in a solution of the wave equation by help of the *Wave-Solver (HS)* code [112]. The electromagnetic wave interacts with an overdense plasma and the results analyzed below were obtained considering the following plasma parameters: the electron density $n_{e0} = 75 \cdot n_{cr}$, electron temperature $T_e = 200\,\mathrm{eV}$ and the electron-ion collision frequency $\nu_{ei} = 2 \times \omega_L = 4.7 \times 10^{15}\,\mathrm{s}^{-1}$. The values are in agreement with the *PIC* simulation results. The calculations have been performed considering an exponential decay of the electron density $n_e(x) = n_{e0} exp(-x/L)$ for different scale lengths. In figure 5.7 the results for the normalized profiles L/λ of 0.003, 0.01 0.02 and 0.1

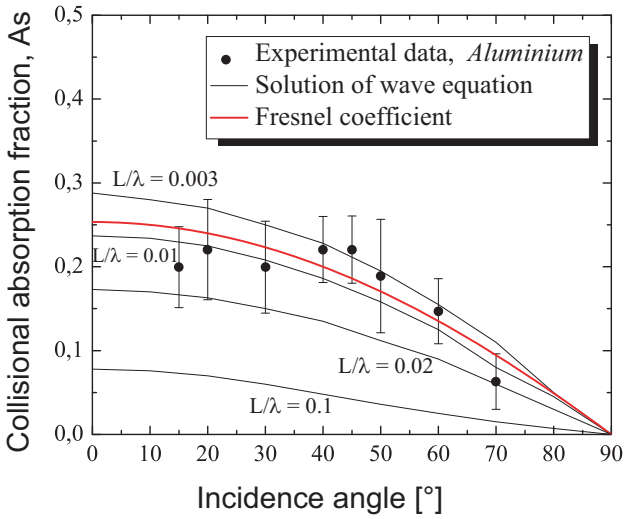

Figure 5.7: Angular dependence of collisional absorption. The experimental data (filled symbols) are plotted together with curves representing the solutions of the wave equation for the plasma parameters $n_{e0} = 75 \cdot n_{cr}$, $\nu_{ei} = 2 \cdot \omega_L$ and $T_e = 200\,\mathrm{eV}$. Different plasma profiles have been considered. For comparison, the calculated absorption fraction from Fresnel equations on abrupt plasma profile assuming similar plasma parameters is shown.

are shown. A good agreement with the experimental results, within the error bars was found for $L/\lambda \lesssim 0.02$.

For these plasma parameters and at these steep profiles, the Fresnel approach for the reflectivity of solid targets with an abrupt interface applies [68, 113]. We calculated the angular dependence of the absorbed fraction as the solution of the Fresnel equations for a flat surface accounting for different values of the complex refractive index (8.4). According to the formula 8.5, the refractive index depends on the normalized parameters as the collision frequency $\nu^* = \nu_{ei}/\omega_L$ and the electron density $n_e^* = n_e/n_{cr}$. The best agreement with the experimental data was found for a complex refractive index $\tilde{n} = 3.8 + i \cdot 6$ as shown in figure 5.7. In the *Aluminum* case, the target can be considered 3 times ionized at solid density which corresponds to an electron density of $n_e \approx 2 \times 10^{23}\,\mathrm{cm}^{-3}$. Consequently, the normalized collision frequency is $\nu^* = 2$, in good agreement with the input parameters on the *HS* code. Both theoretical estimations confirm the collisional absorption by targets in the highly overdense state. The plasma gradient is in agreement with the estimation from the *PIC* simulation.

In these calculation, the electron-ion collision frequency was accounting only for the thermal energy of the electrons (equation 3.20). If one takes into account the quiver energy of the electrons in addition,, the collision frequency decreases and, accordingly, the absorbed fraction. The code may account for this energy but only as a constant parameter neglecting its temporal dependence (see equation 2.12). It is expected that the collisions become less effective due to the increased kinetic energy for intensities above $1 \times 10^{15}\,\mathrm{W/cm^2}$ and a quiver velocity $v_q/c > 0.02$. Below

this limit, the effect of the quiver energy in the absorption fraction is lower than 5%. Consequently, one may expect that the *HS* code overestimates the absorption fraction. However, the absorbed fraction measured experimentally in the s-polarization geometry is expected to be larger than for purely collisional absorption. There are several effects which may lead to a non-zero electric field component perpendicular to the target surface, like the effect of laser pulse focusing, target roughness and critical surface rippling. Therefore, one may expect a p-polarization absorption in s-polarized beam geometry but its contribution is difficult to distinguish.

All the materials investigated (*Al*, *Au*, *BK7 Glass*) show a similar level of s-polarization absorption within the error bars at each incidence angle (see figure 5.1). In the calculations above no physical constants have been considered and the target was modeled as ionized matter characterized only by its density and temperature. Therefore, the agreement between the calculation and the experimental results are available for all overdense, ionized materials of steep density gradients and with similar plasma parameters.

5.6 Target surface quality and its influence on the laser absorption process

The influence of vacuum-plasma interface morphology on the efficiency of the absorption processes was recognized in the experiments with long pulses. Assuming a rippled critical surface, different experimental works [147, 148] reported results which show either an enhancement of the absorption fraction over the value predicted by the theoretical models or a modification on the angular dependence of the absorption fraction. The modulation of the critical surface was attributed to instabilities developed at the critical surface (in the case of moderate intensity and long pulses) or to laser radiation pressure (at higher laser intensity), and theoretical models confirm the experimental observations [150, 151]. The enhancement of the absorbed laser energy was also observed in the case of randomly rough surfaces of thin films irradiated by laser pulses below the damage threshold of the material [152]. At high laser intensities, the role of the target surface with random roughness or manufactured structures was considered in explaining the increased soft [154] and hard X-ray yield [155] or enhanced hot electron production [156].

The experimental results presented in this paragraph show a significant enhancement of the laser energy fraction absorbed by rough targets under certain conditions.

These results allow the analysis of the influence of the target roughness on the total level of absorption of sub-10 fs laser pulses. For this purpose, the behavior of the absorbed laser energy fraction was studied and compared for two different types of targets: mirror-flat *Gold* metallic layers and compact solid *Boron Nitride* ceramic. The experimental set-up and conditions were similar to those presented in paragraph 4.2. The angular dependence of the absorbed energy fraction by *Gold* target shows a distinct behavior for p- and s- polarization geometries with a significant preponderance of the absorption of the p-polarized pulse (figure 5.1). In contrast, in the case of *Boron Nitride* target, the absorption fraction is approximatively constant within the error bars, in the range of $50 - 65\%$ over the whole angular range ($15° - 70°$) without a notable distinction between the laser polarization cases (figure 5.8). The experimental data show a significant enhancement of the absorption in $s-$ polarization case compared to the results obtained in similar geometry for flat surface targets where the absorption was not higher than 30% (for all flat targets investigated, see paragraph 5.2). In $p-$ polarization case, the angular curve loses its strong trend towards higher angles specific to the targets with mirror-flat surface. In figures 5.9 a) - b) the experimental results of the absorption fraction dependence on laser intensity for both polarization cases are shown. The absorbed energy fraction increases from its low value in cold conditions at an intensity of about $1 \times 10^{13}\,\mathrm{W/cm^2}$ and has a maximum of $\approx 80\%$ at an intensity value of $\sim 1 - 5 \times 10^{14}\,\mathrm{W/cm^2}$. After the peak value, the absorption decreases weakly with increasing intensity. The behavior of the absorption in the high intensity range allows to explain the slight increase of the absorption fraction in the angular interval ($50° - 70°$). In the case of these high incidence angles, the laser spot at the target surface decreases and, accordingly, the incident laser intensity decreases by a factor of $\cos\theta$. Therefore, the average laser intensity incident on the target surface in the best focus decreases from its value on the normal direction of $5 \times 10^{16}\,\mathrm{W/cm^2}$ to $\approx (1 - 3) \times 10^{16}\,\mathrm{W/cm^2}$. According to the experimental data presented in figure 5.9, this corresponds to an increase of the absorption fraction of about $(5 - 10)\%$ consistent with the angular behavior observed at high incidence angle (figure 5.8). It is interesting to note that similar values of the total amount of the absorbed fraction were observed, irrespective to the incidence angle and polarization over the whole intensity range considered in these experiments ($5 \times 10^{14} - 5 \times 10^{16}\,\mathrm{W/cm^2}$) within the error bars (figure 5.9).

The main physical parameter which differentiate these two categories of targets is the surface flatness. The surface quality derive from the manufacturing procedure.

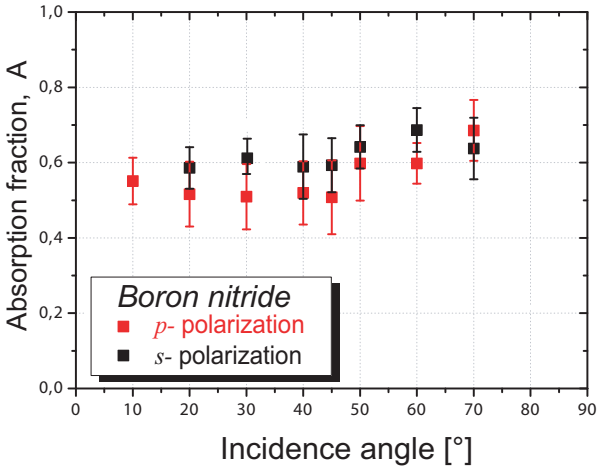

Figure 5.8: Experimental angular dependence of the absorbed energy fraction A of 8 fs, 790 nm laser pulses by a rough *Boron Nitride*. The data points correspond at average intensity of $5 \cdot 10^{16}\,\mathrm{W/cm^2}$ (in the best laser focus) for both polarization geometry, p and s. The standard deviation of the data points is in the range of $(20 - 25\%)$

The metallic targets have been obtain by thermal evaporation in ultrahigh vacuum conditions with a thickness of 300 nm while the boron nitride target was manufactured as hot-pressed compact powders. The non-uniformities of the surface are described by the roughness, $\bar{\sigma}$, defined as $\bar{\sigma} = \sqrt{\frac{1}{n}\sum_{i=1}^{n} h_i^2}$, where $h_i = z_{max,i} - z_{min,i}$ is the distance "peak-valley" of the surface deviations. A target surface is considered rough relative to the laser wavelength obliquely incident if its non-uniformities are larger then $\lambda/(4\pi\cos\theta)$ [64, 149], where λ is the laser wavelength and θ is the incidence angle. Accounting for this criterion, for $\lambda = 800\,\mathrm{nm}$, a surface roughness of $\approx 60\,\mathrm{nm}$ may affect the target reflectivity. The surface imagines of *Gold* and *BN* targets recorded using an atomic force microscope (see figure 5.10) allow to estimate the average roughness as $\bar{\sigma}_{Gold} \approx 2.5\,\mathrm{nm}$ and $\bar{\sigma}_{BN} \approx 500\,\mathrm{nm}$.

There are several effects of the target roughness which may explain the different dependencies found experimentally for rough and flat targets. A first effect is the possibility of the laser pulse to suffer multiple reflections on the walls of the granulations. These may lead to a significant increase of the total amount of absorption [153]. The second effect derives from the fact that the target morphology or the scattering processes on the target may lead to a local variation of the incidence angle which affects in principle the polarization geometry of the incident laser pulse. As direct consequence, the difference between the $p-$ and $s-$ polarization is canceled and the interaction geometry is converted into a mixture between both polarization cases. In the *Gold* target case, the surface flatness allows locally the preservation of the angular and the polarization geometry. On the contrary, the roughness of the *BN*

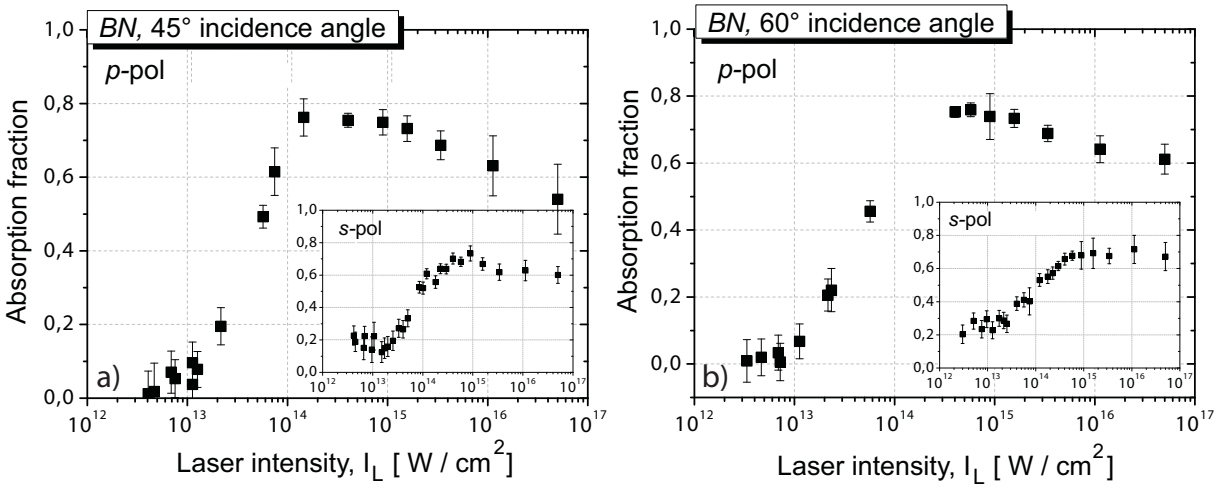

Figure 5.9: Experimental results of the absorption fraction on the laser intensity of sub-10 fs laser pulses obliquely incident at a rough *Boron Nitride* target. In the main frames of plots a) and b) the experimental data obtained in p-polarization geometry at incidence angle of 45° and 60° are shown respectively. In the insets, the corresponding experimental data are presented for s-polarization at the same incidence angles.

target, which is in the order of the laser wavelength, determines a random spread of incidence angle and leads to the loss of geometrical distinction of the radiation polarization over the laser focal spot. Regarding the contribution of the different absorption mechanisms, at small incidence close to the normal incidence angles, the dominant mechanism is the collisional absorption (inverse bremsstrahlung) for both polarization cases. In contrast with the flat *Gold* targets where the absorbed fraction at these small angles is about 30%, for BN rough target is in order of 55% (compare figures 5.1 b) and 5.8). This significant increase can be attributed to the contribution of the collisionless processes effective in $p-$ polarization geometry (see paragraph 3.3.2). This geometry is facilitated by the macroscopic non-uniformities and local depolarization of the incident radiation. Moreover, it is worth to recall that both collisional (inverse bremsstrahlung) or collisionless absorption processes presents specific angular and polarization dependencies (see paragraphs 3.3.1 and 3.3.2). In the case of BN target the lack of these dependencies does not allow to distinguish the individual contribution of energy transfer processes and can be interpreted as a mixed contribution of these categories of processes. Other effects which may lead to morphological non-uniformities and consequently, to the depolarization

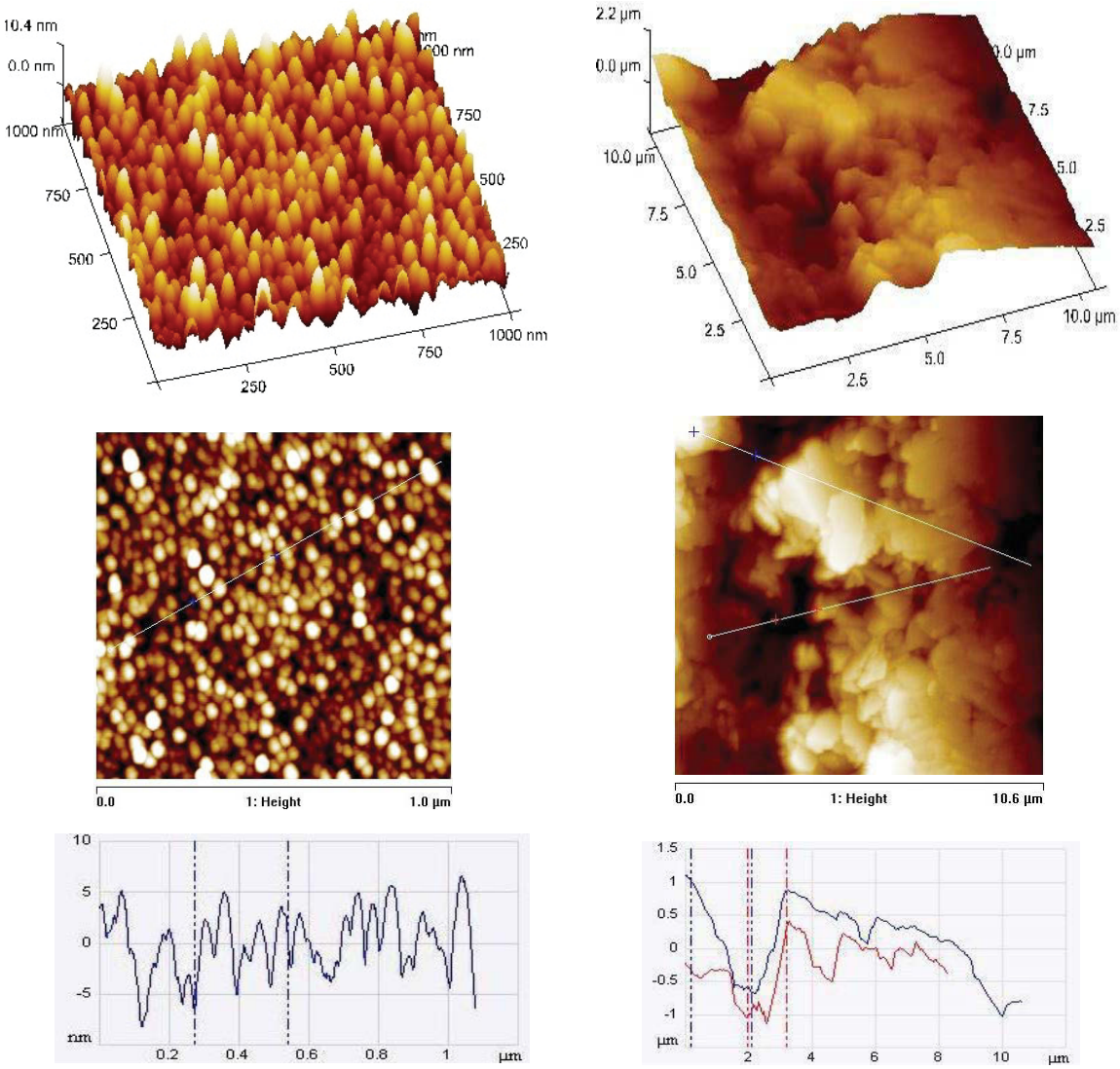

Figure 5.10: AFM images in 3-D and 2-D snapshots of: (*Left*) the smooth *Gold* target surface of a roughness $\bar{\sigma} \approx 2.5\,\text{nm}$ and (*Right*) unpolished *Boron Nitride* target surface with an average roughness $\bar{\sigma} \approx 500\,\text{nm}$. In the plots the 1-D profiles for both surfaces are shown[1].

[1]By courtesy of *Institut für Experimentelle Physik der kondensierten Materie*, Heinrich-Heine University, Düsseldorf

of the laser radiation like critical surface rippling or hydrodynamic instabilities can be neglected in the case of steep plasma profiles and ultrashort laser pulses [150].

The experimental observations in the case of *BN* target are in agreement with the previous experimental results of X-ray emission and hot electrons production by the interaction of high intensity laser pulses with rough solid targets [155, 156]. In particular, Rajeev *et al.* [156] reported an almost constant temperature of hot electrons $T_{hot} = 6.1\,\mathrm{keV}$, irrespective of the polarization state of the incident laser and incidence angle. The hot electrons were produced by rough copper targets irradiated by 100 fs laser pulses in an intensity range of $(10^{15} - 10^{16}\,\mathrm{W/cm^2})$. In [155] a significant enhancement (by a factor ≈ 4) of the bremsstrahlung yield emitted by a rough target compared with a polished one was reported, at the normal incidence. The observation was explained by the contribution of a p-polarized component in the normally incident laser pulse which induces the resonance process. The experimental results presented above are in qualitative agreement with these observations.

Chapter 6

Soft X-ray emission of dense plasmas

The extremely fast heating process of a solid target by an ultrashort, sub-10 fs laser pulse, leads to the formation of a thin, hot and dense plasma layer. During the heating, this layer has a thickness in order of the skin depth (equation 3.1) where the laser deposits its energy and has a negligible expansion on a femtosecond time scale. These characteristics are confirmed by *PIC* simulations described in the paragraph 5.2.2. The front layers start to expand and to cool down while the thermal energy is transported by the electrons to the deeper target layers. The created plasma is in the same time a highly radiative matter. As discussed in paragraph 3.4, spectroscopic investigations of plasma emission can offer valuable information regarding the plasma state during the emission and the physical effects associated with it. In this paragraph the experimental results of time integrated spectra emitted by plasmas created by ultrashort, sub-10 fs and high contrast laser pulses will be presented (paragraph 4.1.1). In addition, spectroscopic investigations on dense plasma with inhibited hydrodynamic expansion, created in coated targets have been carried out. In these experiments, an average intensity of about $5 \times 10^{16}\,\mathrm{W/cm^2}$ was achieved in the focus. As will be shown, laser pulses focused with this intensity onto low-Z targets are able to create highly ionized plasma including hydrogen-, helium-, lithium-like ionization stages and consequently, the emission spectra are expected to contain resonance spectral lines from the K-shell. For elements with atomic numbers $2 \leq Z \leq 9$ the K-shell emitted radiation is in range of X-ray and soft X-ray range ($1 - 100\,\mathrm{nm}$).

In the experiments discussed in this paragraph, two sorts of solid targets were used: *Lithium Fluoride* (LiF, $Z_{Li} = 3$, $Z_F = 9$) and *Boron Nitride* (BN, $Z_B = 5$, $Z_N = 7$). There were also studied LiF targets coated with *Aluminium* layers with different thicknesses. The emission spectra have been recorded with the high resolution XUV spectrometer described in paragraph 4.3.

6.1 Emission spectra of low-Z bulk targets in XUV range

6.1.1 Experimental time integrated spectra

In figure 6.1 typical spectra of a LiF plasma recorded on two different detectors: CCD camera (spectrum a)) and on IPs (spectrum b)) are shown. In the spectrum recorded on CCD camera the resonance lines of *Lithium* He-like ion are observed: He_α $1s^2 - 1s2p$ (199.28 Å), He_β $1s^2 - 1s3p$ (178.01 Å) and He_α $1s^2 - 1s4p$ (171.58 Å). Due to the aluminium filter attached to the CCD camera, the spectral emission with wavelengths below the absorption L_{II} edge of aluminium ($\lambda < 171$ Å) is not detected by the camera. In the experiment, the laser pulses have been focused onto the target with 1 kHz repetition rate while the target was vertically translated with 250 $\mu m/s$. The spectra have been time integrated over about 10^5 shots.

Additional information on LiF plasma emission are contained in the spectra recorded on IPs although with a poor resolution (figure 6.1 b)). The spectral range corresponding to the resonance lines of Li H-like ion is accessible in the case of this detector. From this series, only the H_α line $1s - 2p$ (134.99 Å) is observed while the higher series lines of the H-like ion are missing. For example, at 113.9 Å the H_β line $1s - 3p$ is predicted but not observable in the recorded spectrum. The observation about higher line series suppression is consistent with previous experiments where the similar effect was reported for other low Z-elements like *Carbon* and *Boron* [144, 145]. For the spectra recorded on IPs, $6 \cdot 10^5$ shots per spectrum have been accumulated.

Spectra presented in figure 6.1 contain a number of low intensity spectral features which have been identified as contribution of *Flourine* ion emission. Spectral lines of ions with a ionization degree $Z \leq +5$ are labeled as follows: the resonance lines of F IV, F V and F VI ions are indicated in the spectra with numbers (1-5) and summarized in the table 6.1; there are spectral features (labeled with roman numbers I-VI) which have been identified as spectral emission contribution of different double-excited states of F IV and F V ions. According to the tables [49], these structures may represent overlaps between different lines with close energies. For example, in the spectral range $162 - 163.6$ Å corresponding to the structure I, more than 10 transitions are listed as radiative decays of F V ion from double-excited states.

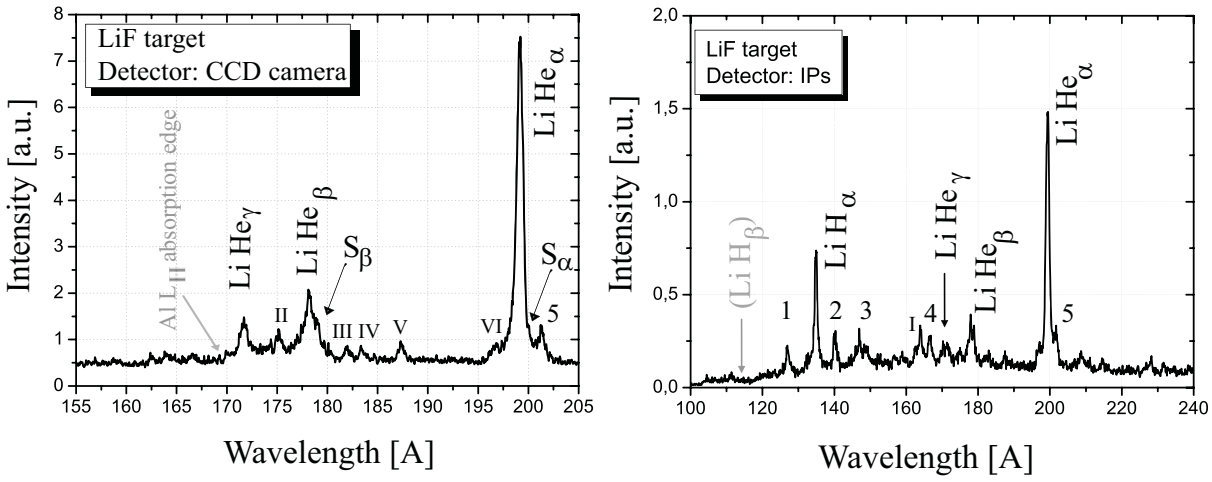

Figure 6.1: Soft X-ray spectral emission of a *LiF* plasma produced by 8 fs laser pulse. A typical spectrum recorded on CCD camera is presented in plot a). *Lithium* K-shell resonance lines of *He*-like ion were observed. *Fluorine* lines (labeled with 1-5 and I-VI) and satellite lines features of *Lithium* lines (S_α and S_β) were recorded (for details, see text). In plot (b), a *LiF* spectrum recorded on *IPs* is presented where, in addition, the H_α line is observed. The higher series lines of the H-like Li ion are suppressed by pressure ionization.

Table 6.1: List of *Fluorine* resonance spectral line on the LiF emission spectra (figure 6.1 a)-b))

Label	Spectral line	Wavelength [Å]
1	F VI $1s^22s^2 - 1s^22s3p$	126.9
2	F V $1s^22s^22p - 1s^22s^24s$	140.2
3	F V $1s^22s^22p - 1s^22s2p3p$	147.9
4	F V $1s^22s^22p - 1s^22s^23d$	165.9
5	F IV $1s^22s^22p^2 - 1s^22s^22p3d$	201.0

The resonance lines of Lithium, He_α and He_β, present asymmetric wings and the contribution of dielectronic satellites in the high wavelength side of the lines can be employed (S_α and S_β). The individual lines structures are not resolved: for example, according to [49], in the spectral range $(199.28 - 200.32)$ Å of S_α, 9 dielectronic *Li*-like satellites may contribute to the structure.

Similar investigations have been performed on the emission spectra of a BN plasma. A typical spectrum recorded on IPs is shown in figure 6.2. In the investigated spectral range, the resonance lines of *Nitrogen* ions, N VI and N VII, have been observed. The K-shell transitions of the *He*-like recorded in the spectrum are: He_α $1s^2 - 1s2p$ (29.08 Å), He_β $1s^2 - 1s3p$ (24.89 Å) and He_α $1s^2 - 1s4p$ (23.77 Å).

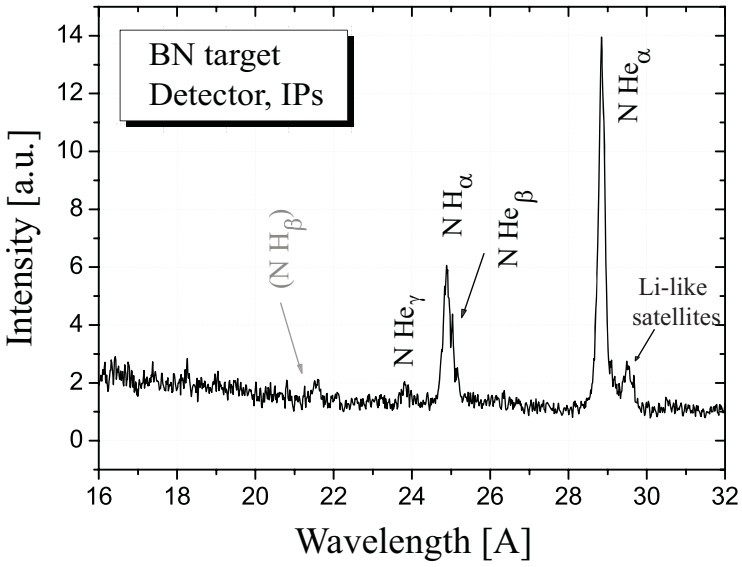

Figure 6.2: Soft X-ray emission spectrum of a *BN* plasma produced by 8 fs laser pulse. Resonance lines of *H*- and *He*-like *Nitrogen* ions have been observed. A series limit of the H-like ions is detected.

For the *H*-like series, the single line recorded is H_α line $1s-2p$ (24.77 Å) and, similar to the Li plasma emission, the effect of series limit can be observed. On the red side of He_α line *Li*-like dielectronic satellites were recorded. The spectrum was corrected accounting for the gold reflectivity dependence on the radiation wavelength for the interesting spectral range (figure 4.8).

6.1.2 Interpretation of the dense plasma XUV emission

After the rapid heating process, plasmas created by ultrashort, 8 fs laser pulses starts to expand into the vacuum. During this expansion, the plasma is highly transient (in time and space) and evolves from hot and dense up to cold and diluted states with important spatial and temporal variations of plasma parameters (n_e, T_e, average ionization degree). In time integrated spectra are accumulated the contributions of the plasma emission during its whole expansion time when the emissivity proprieties change significantly.

One of the most important observation in the experimental spectra is the *series limit* of the H-like like ions in low Z plasmas. This effect was attributed to the *pressure ionization* (see paragraph 3.4). The influence of the plasma density on the energetic levels and consequently, on the emission spectra can be analytically estimated using the formula 3.37. In the figure 6.3 the ionization potential lowering ΔE is presented in the case of lithium ions Li III (H-like) and Li II (He-like) as func-

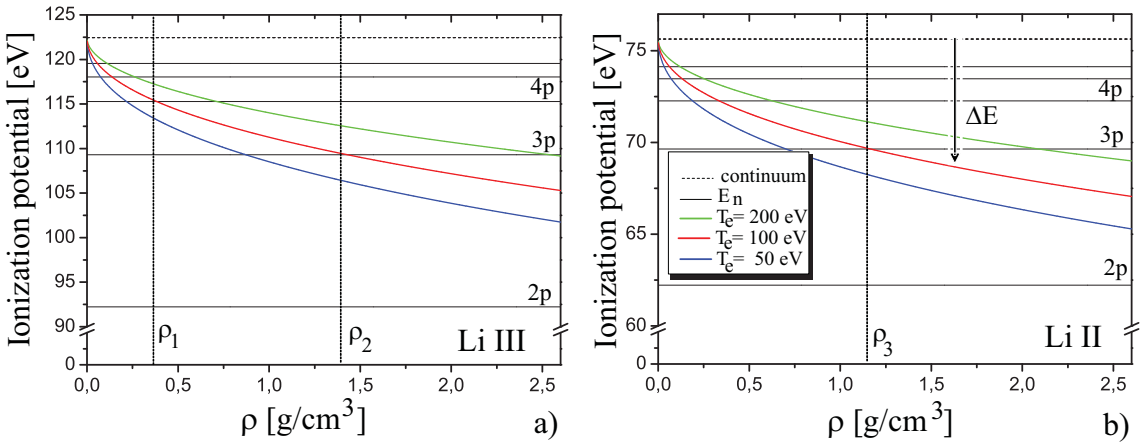

Figure 6.3: The effect of pressure ionization on the atomic bound levels is estimated by the ionization potential lowering dependence on the mass density. Plots a) and b) present the atomic levels and the ionization potential for H-like and He-like lithium ions, respectively. The calculations have been performed for three electron temperatures.

tion of mass density. The calculation accounts for an average ionization charge of $Z^* = 5$ and for different relevant electron temperature: $T_e = 50\,\mathrm{eV}$, $T_e = 100\,\mathrm{eV}$ and $T_e = 200\,\mathrm{eV}$. For both ions, Li II and Li III, over the entire density range and at considered temperatures, the atomic level $2p$ is not affected by the pressure ionization and the emission of H_α and He_α resonance lines are expected at any density value. In the case of Li III ions in a dense, moderate hot plasma ($T_e = 100\,\mathrm{eV}$), the continuum level is lowered below the atomic level $3p$ for mass densities $\rho > \rho_2 = 1.4\,\mathrm{g/cm^3}$. All the atomic levels with ionization potential larger than $E_{3p} = 109.3\,\mathrm{eV}$ are effectively free at a plasma temperature $T_e = 100\,\mathrm{eV}$. Consequently, the high frequency resonant lines cannot be emitted in this density range and the series of Li III ion is limited only to the H_α line. Theoretically, the plasma expansion and the density decrease enable the emission of H_β lines for $\rho < \rho_1 = 0.34\,\mathrm{g/cm^3}$. As will be shown below, the plasma expansion is accompanied by a fast cooling process and the population of Li III ions drops significantly. In case of Li II ions, the emission of the He_β lines corresponds to $\rho > \rho_3 = 1.1\,\mathrm{g/cm^3}$ at a plasma temperature of $T_e = 100\,\mathrm{eV}$. The detection of the series limit on an experimental emission spectrum is an indication of a high density plasma state. For high transient plasmas as are those created by ultrashort laser pulses, the variation of the plasma parameters (n_e and T_e) in time and space has to be included in the analysis [36].

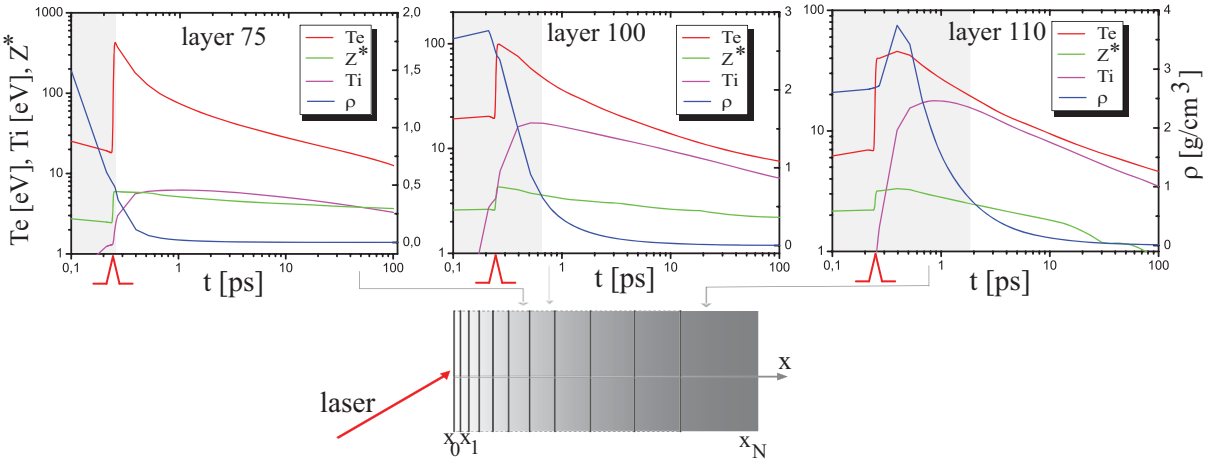

Figure 6.4: The target configuration in 1D hydrodynamic simulation using *MULTI-fs* code (below). The temporal evolution of physical plasma parameters in three LiF target layers (N=75, 100 and 110) during the expansion is shown. The shaded regions emphasize the time interval when the pressure ionization suppress the discrete atomic levels with $n \geq 3$ in a Li III ion.

In order to analyze the dependence of the plasma parameters on the emitted radiation combined simulation using the hydrocode *MULTI-fs* with the collisional-radiative code suite *FLY* have been performed. A description of both codes and the simulation conditions are presented in Appendix B. The plasma expansion on a picosecond time scale was simulated hydrodynamically with the *MULTI-fs* code. The code was extensively used to model the evolution over long time plasmas created by short laser pulses [135, 140]. The XUV emission of the expanding layers was simulated by help of *FLY* codes. The temporal evolution of physical parameters of each plasma layer resulting from hydrodynamic simulation were included in the *FLY* code. The time-dependent collisional-radiative atomic kinetic calculations determined the emissivity and opacity of each layer and the dynamics of ion populations during the plasma expansion. In the following, simulation results for LiF and BN plasmas will be presented and compared with the experimental spectra.

In figure 6.4, the configuration of a solid target in 1D geometry considered in the simulations is schematically represented. The target is divided into a number of $N = 160$ layers. The laser pulse at an intensity of $3 \times 10^{16}\,\mathrm{W/cm^2}$ is incident at 45° onto a plasma with a profile of few nm. The expansion of three layers of a LiF target is presented in detail, showing the temporal evolution of the plasma

parameters (electron and ion temperature, T_e and T_i, average ion charge, Z^* and mass density, ρ) over a temporal range of 100 ps. The laser peak corresponds to the time moment $t_p = 0.25$ ps and this moment is marked on the plots. In the target configuration, the layers considered in figure 6.4 occupied the position N=75, 100 and 110 and their original coordinates were $x_{75} = 3.75$ nm, $x_{100} = 5$ nm and $x_{110} = 65$ nm, respectively. Accounting for the full time description of the plasma layer parameters during the hydrodynamic expansion, the effect of the ionization potential depression can be analyzed now in time. For example, in the case of Li III ion, one can investigate the time interval when the discrete bound states with quantum number $n \geq 3$ are suppressed by pressure ionization (PI). These intervals are marked on the plots of figure 6.4 for each analyzed layer. For layer $N = 75$, PI suppresses the atomic levels with $n \geq 3$ up to the time of $t \approx 0.24$ ps, close to the laser peak. After this time, when the plasma is at high temperature and moderate density, the level $n = 3$ becomes bound. For layers found deeper into the target with higher density and lower temperature, the PI effect on these levels is longer effective in times up to $t \approx 0.65$ ps for layer $N = 100$ and $t \approx 2$ ps for layer $N = 110$. Thus, the higher series lines cannot be emitted during the high density plasma phase when the mass density is close to solid density. According to the simulation results, during the expansion, this effect occurs in time around the laser peak and can last for deeper layers up to few ps after the heating process.

Hydrodynamic simulations performed for a BN plasma showed a similar effect of PI for atomic levels of the H-like Nitrogen ions (N VII). Regarding the effect of PI on $3p$ level of the N VII ions, it was found that the time interval when the PI acts for suppressing this level is shorter by a factor of about 2 compared to LiF plasma for deeper layers. This can be explained by accounting for the speed of plasma expansion (equation 2.1) which depends on the ion mass and, in the case of compounds, is controlled by the heavier ion. Thus, a BN plasma will expand faster than a LiF one and the high density plasma phase in a BN plasma will last shorter.

For simulating the time integrated spectra, the FLY code was used to obtain the time-dependent populations dynamics and the emission spectra for each layer of the target. The atomic kinetics calculations of the FLY code provide the emissivities ε_ν and the opacities κ_ν of the layers. The time integrated spectrum was obtained using the integration method described in [145]. The emission contribution of each layer was calculated by solving the radiation transfer equation and spatially integrating it over the whole target. In the final spectrum, the calculated intensities of each indi-

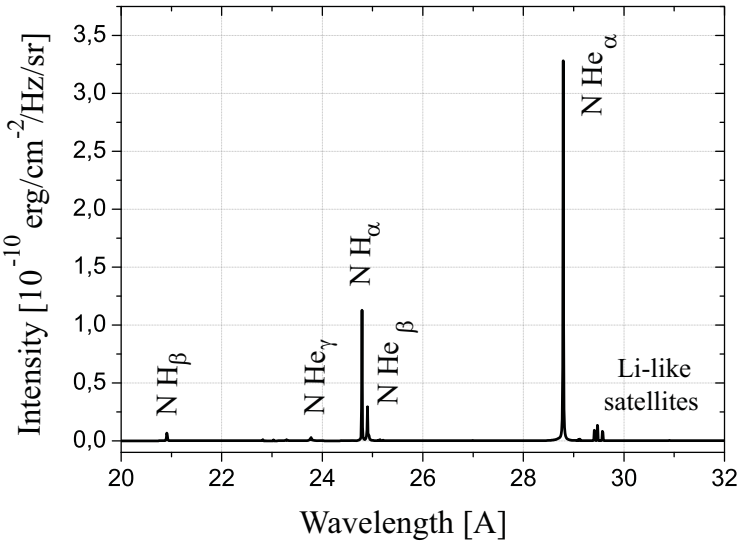

Figure 6.5: Soft X-ray emission spectrum of a *BN* plasma produced by an 8 fs laser pulse. Resonance lines of *H*- and *He*-like *Nitrogen* ions have been observed. A series limit of the H-like ions is detected.

vidual layer are summed for each time step. The results of this integration method will be illustrated and discussed in the following for a BN plasma. In the figure 6.5, the XUV synthetic spectrum for a BN plasma is presented. The dominant spectral lines in the spectrum are the H_α and He_α lines and the ratio of their intensities was found $H_\alpha/He_\alpha = 0.33$. The value is in good agreement with the one found experimentally of 0.29 within the experimental error of about 20%. The effect of pressure ionization on suppressing the higher orders of the *H*-like and *He*-like series is observed. In the simulated spectrum, a small contribution of the H_β line is calculated corresponding to a intensity ratio $H_\beta/H_\alpha = 0.06$. The value is in the range of the noise in the experimental spectrum and therefore, a distinct contribution of this line was not distinguished in the recorded spectrum. He_β and He_γ lines are also calculated with a very small contribution of the last one and their intensities relative to He_α line were found to be : $He_\beta/He_\alpha = 0.2$ and $He_\gamma/He_\alpha = 0.01$. The emission of the *Li*-like satellites is as well reproduced in the red side of the He_α line.

The temporal contribution of different spectral lines during the emission cannot be distinguished from time integrated spectra which accumulate the plasma emission during the whole life time. Investigating the results of the combined simulations *MULTI-fs* and *FLY* a temporal physical scenario of target layers emission proprieties can be determined. In the heating phase, the front target layers reach temperatures up to few hundreds of eV and expands very fast. The emission contribution of these layers in the total spectrum is very low. For example, the time integrated He_α line intensity of a layer found originally at the coordinate $x = 1\,\text{nm}$ is by a factor of 10^5 smaller compared with the same line from a deeper layer ($x' = 3\,\text{nm}$). The main

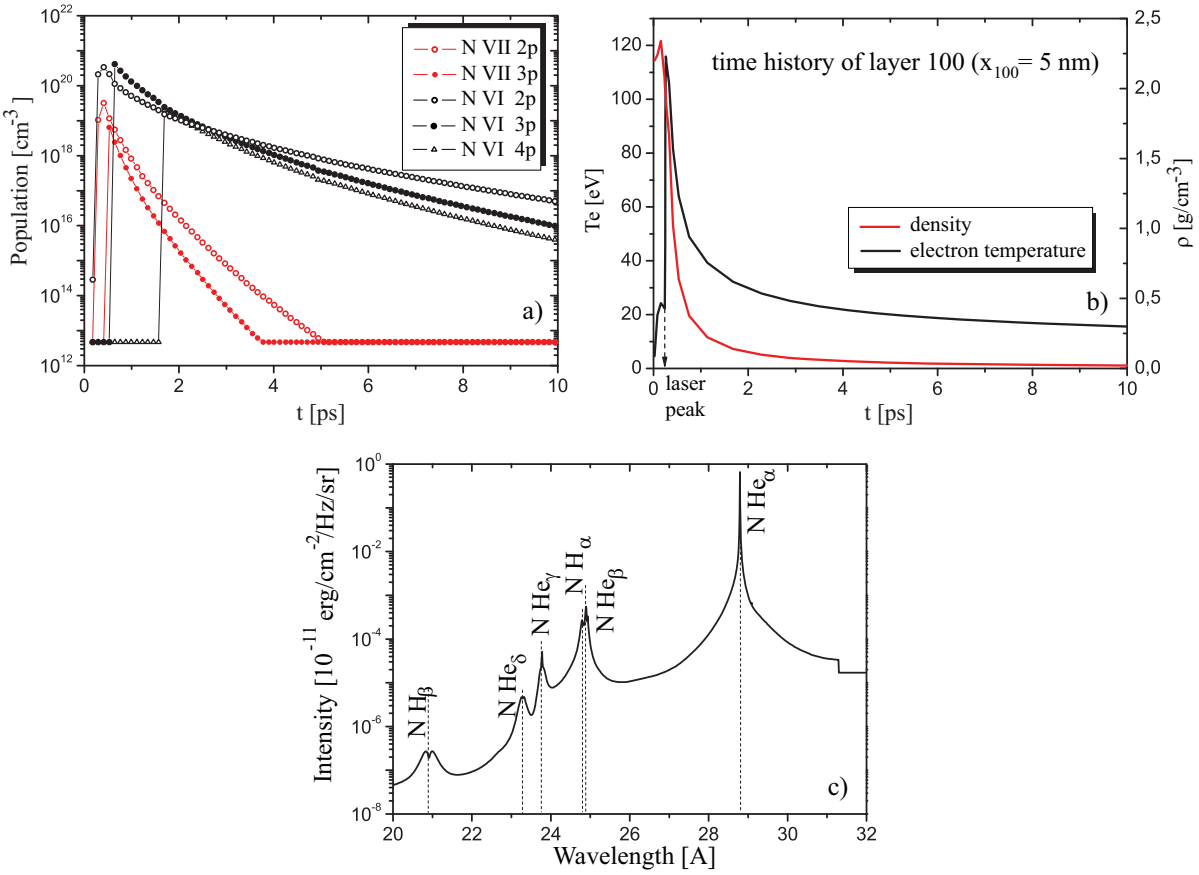

Figure 6.6: Computer simulations of the ion populations, plasma parameters and emission spectrum of the layer N=100. In plot a), *FLY* simulation results for the temporal dependence of the N VII (*H*-like) and N VI (*He*-like) ions' populations in different excited states relevant for the *K*-shell emission are shown. The time history of the mass density and electron temperature of the layer are plotted in graph b). The time integrated emission spectrum of the layer is presented in plot c), as time-dependent solution of *FLY* simulation.

contribution to the spectrum is coming from the layers found behind the rarefaction front target. The observable intensity of the spectral lines depends on the ions populations on the ground and excited states corresponding to a certain transition. Thus, a good indication regarding the plasma emissivity is offered by the temporal dynamics of the ion population within each target layer. In the figure 6.6 a), the time dependence of the N ion population in different excited states corresponding to the upper levels in the resonance transitions of the *H*-like and *He*-like are shown. The results correspond to the layer $N = 100$ ($x_{100} = 5\,\mathrm{nm}$). For comparison, the temporal evolution of the plasma parameters (density and temperature) in the same

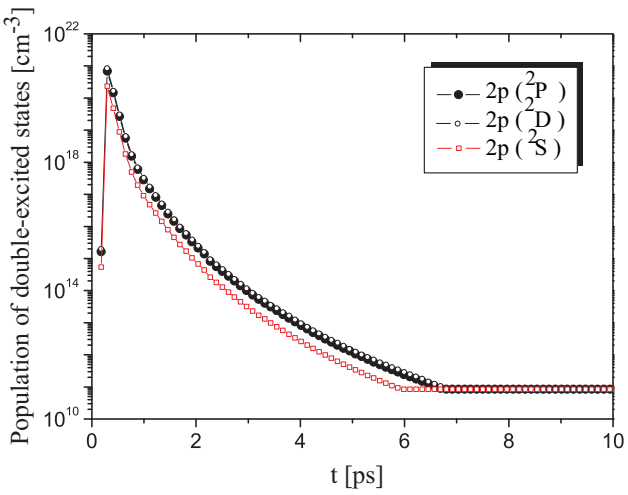

Figure 6.7: *FLY* simulation results for the temporal dependence of the double excited state populations of *Li*-like N ions in the layer N=100.

layer is plotted in figure 6.6 b). The ion populations increase sharply and reach their maximum values within a time interval of about 300 fs after the laser peak. In this interval, the plasma is in a high density state ($\rho/\rho_{solid} = 50\% - 90\%$) and its temperature is between 65 eV and 115 eV. For the considered layer, the effect of PI on the higher excited states N VII 3p and N VI 4p is observed for time intervals of 300 fs and 1.5 ps, respectively. The populations of excited states in the *H*-like N ions (N VII 2p and 3p) decrease fast, with a time constant of about 100 fs while the corresponding time constant for *He*-like ion population (N VI 2p, 3p and 4p) is an the order of 500 fs. Note that the population of N VII 3p is smaller than the population N VII 2p by a factor of 10 indicating a very weak emission of the H_β spectral line. The time integrated spectrum shown in the figure 6.6 c) represents the contribution of the analyzed layer to the total spectrum. The most intense spectral lines are He_α, He_β and H_α while the higher order spectral lines have a very small contribution. Similar analysis can be performed for each target layer identifying the temporal plasma emission properties. Thus, the combined hydrodynamic and radiative simulations indicate that the main emission of the *H*- and *He*-like resonance lines recorded experimentally originates from time intervals when the plasma is in the high density state. This is demonstrated by the ion population dynamics during the plasma expansion. The simulation results show as well the effect of pressure ionization in the early plasma stages.

The *Li*-like dielectronic satellites observed experimentally near to He_α line corresponds to the transition $1s^2n'l' - 1s2pn'l'$ and could represents an overlap of many individual satellites lines. Although there is a large number of combinations for the quantum numbers $(n'l')$, in dense plasmas, the pressure ionization effect

reduces the number of highly excited ionic levels that could be occupied by the spectator electron. *FLY* simulations have been employed for calculating the populations of auto-ionizing (double-excited) states with a spectator electron captured on the energy level $2p$ and having the following atomic configurations: $1s2p^2(^2P)$, $1s2p^2(^2D)$ and $1s2p^2(^2S)$. The temporal evolution of these states population in the layer N=100 as a time-dependent solution of the *FLY* is shown in the figure 6.7. The simulation results show that the double excited states are highly populated in the time intervals corresponding to the high plasma density. The populations decay fast afterwards with a time constant of about 200 fs while plasma expand and cool down (compare with figure 6.6 b)). These observations indicate that the satellite lines are emitted preponderantly in dense plasma stages. The simulated spectra for a LiF target and the analysis of *Li*-like satellites emission leads to similar conclusions.

Summarizing, the *K*-shell emission spectra recorded in these experiments of low-Z laser produced plasma contain spectral features which indicate that dense, emissive plasmas are created by ultra-short laser. The synthetic spectra calculated by the help of the combination between hydrodynamic and collisional radiative atomic codes are in good agreement with experimental results. Time dependent calculations of the plasma emissivity and ion populations within target layers allow to unfold the temporal evolution of the plasma.

6.2 XUV emission spectra of coated targets

The fast local deposition of the laser energy onto very thin solid layer induces strong temperature gradients at the boundary region between the hot plasma and the rest bulk target, cold and at solid density. In the same time, the rapid expansion of front heated layers induces a shock wave into the bulk target. After the heating phase, the absorbed laser energy is carried into the target in principal by the electrons. If the electron mean free path λ_e is much smaller than the temperature scale length $L_T = |\nabla T_e/T_e|^{-1}$, the energy transport through the target is caused by a diffusive heat wave which propagates hydrodynamically inside the target [2]. In the diffusive approximation, the energy transport is described within Spitzer-Härm model and the heat flux is given by [77]:

$$Q = -\frac{1}{3}\lambda_e v_e k_B \nabla T_e = \kappa \nabla T_e \tag{6.1}$$

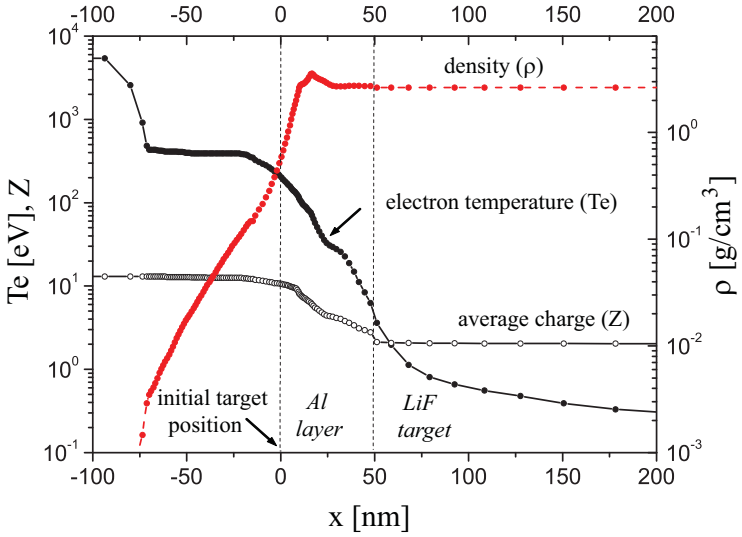

Figure 6.8: 1D hydrodynamic simulation of an ultrashort laser pulse (8 fs, 5×10^{16} W/cm^2) interaction with LiF target coated with 50 nm Al layer. The laser is incident from the left side. The plot represents a snapshot of the plasma parameters at 100 fs after the laser peak.

Here, κ is the electron thermal conductivity. In plasmas produced by ultra short laser pulses, steep temperature gradients are created and the condition of $\lambda_e/L_T \ll 1$ is no longer satisfied. For $\lambda_e/L_T > 10^{-2}$, the diffusion approximation overestimates the heat transport predicting a heat flux larger than the free steaming flux of the electrons ($Q_F = n_e v_e k_b T_e$), which is an unphysical result [2, 71]. To model the reduced energy transport in this situation, in the hydrodynamic calculations one accounts for an inhibition factor defined as: $f = Q/Q_{SH}$. Here, Q is the corrected heat flux in a steep temperature gradient and Q_{SH} is the heat flux predicted by the diffusion approximation. In hydrodynamic calculations reported previously for modeling laser plasma interaction values of the factor f between 0.6 and 0.001 have been considered depending on specific experimental conditions (laser parameters, 2D and 3D energy transport effects, target type)(e.g. [140, 145, 146]).

The energy propagation inside of a cold solid leads to *isochoric heating* of matter in the high density state. The deeper layers of the solid target are less affected by the hydrodynamic expansion while they are traversed by the heat wave. The spectroscopic investigations of laser produced plasmas in coated targets is one of the experimental methods to determine the physical properties of dense, isochorically heated plasmas. The coating layer is the medium which supports the heat transport up to the target substrate and also inhibits the expansion of the substrate layers. The emission spectra of this type off target contain spectral lines of both materials, the coating and the substrate, but the radiation emitted by the last one originates, preponderately, from the high density state. In figure 6.8 on shows the spatial dependence of some physical parameters of a LiF target coated with 50 nm

Al layer, obtained from an 1D hydrodynamic simulation with the *MULTI-fs* code. The calculation corresponds to a time of 100 fs after the laser peak and the spatial coordinate represents the target layer initial position and indicates the thermal energy transport up to the plasma layers found at solid density or higher. The life time of these regions is of the order of few ps before expansion and cooling down rapidly.

In the experiments discussed in this paragraph specially prepared targets have been used consisting in a *Lithium Fluoride* substrate covered by an *Aluminium* layer with different thicknesses h_c between 30 nm and 200 nm. The emission spectra of these targets have been recorded using the flat-field spectrometer described in paragraph 4.3. Image Plates have been used in this case as detector. In the figure 6.9 the spectra emitted by LiF substrates covered with Al layers of thicknesses $h_c = 60, 80, 150$ and 180 nm are shown . For comparison, spectra of uncoated LiF and Al target are also shown. The main spectral features in the spectra are labeled. In these experiments the laser was operating in single-shot mode and for a recorded spectrum between 4000 and 6000 shots were accumulated. The spectra are normalized to the number of shots. In the emission spectra of Al target the contribution of spectral lines: Al IV $2p - 3s$ (160.07 Å), Al IV $2p - 3d(^3P^0)$ (131.64 Å) and Al IV $2p - 3d(^1P^0)$ (129.73 Å) were identified in principle. In the spectra of coated targets, both contributions of Li and Al ions are observed.

The incident laser pulse penetrates into the coated layer only over the skin depth, which in Al case is about 10 nm. Thus, as long as the laser cannot reach the LiF substrate, the radiation emitted by the Li ions represents a consequence of the heat transport into the target. The *energy penetration depth* δ can be defined as being the depth into the target where the plasma emission is $1/e$ of the maximum value in terms of line intensity. From the experimental spectra, one can estimate the energy penetration depths of about 80 mn and 120 mn for the spectral line $Li\ He_\alpha$ and $Li\ H_\alpha$, respectively. The extinction of the Li spectral lines occurs for a coating thickness $h_c > 180$ nm. The emission of the $Li\ H_\alpha$ requires a higher temperature than the $Li\ He_\alpha$ line. Consequently, due to fast decay of the temperature into the target's layers, it would be expected that the energy penetration depth of the $Li\ H_\alpha$ line to be smaller than that of $Li\ He_\alpha$. The experimental observation can be explained accounting for the pressure ionization effect in the heated LiF layers. Together with the heat flux in the target, a shock wave is propagates producing an increase of the matter density up to few times over the solid density (see figure 6.8).

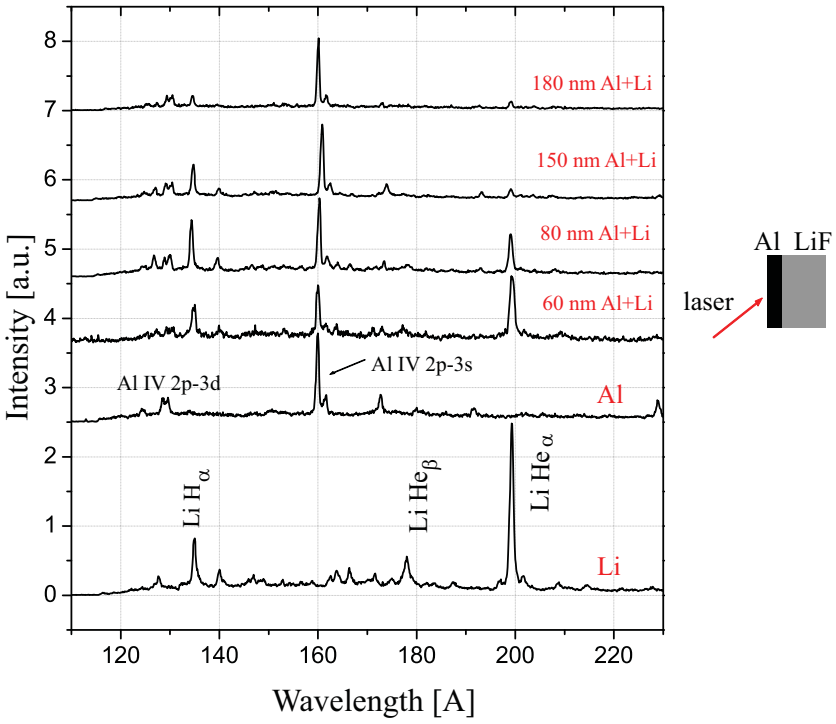

Figure 6.9: XUV spectra of the *LiF* target coated by an *Al* layer with different thicknesses. Reference spectra of *Al* and *LiF* bulk targets are shown. Spectra are plotted with offset for a better viewing.

In these very high density conditions, the ionization potential lowering (equation 3.37) is stronger for *He*-like Li ions than for the *H*-like ones. Accounting for reasonable plasma parameters indicated by the *MULTI-fs* simulations and the pressure ionization formula 3.37, at a temperature of 50 eV for example, the atomic level $n = 2$ of a *He*-like Li ion is shifted into continuum (no emission of the He_α line) for a density $\rho > 1.6 \cdot \rho_{solid}$ while in the *H*-like Li ion case the atomic level $n = 2$ is still bound up to $\rho \approx 3 \cdot \rho_{solid}$. Thus, the contribution of the Li He_α line in the spectra corresponding to coated targets is found to decay faster than the contribution of the Li H_α line indicating that the first line is over longer emission time limited. While the temperature decays and, accordingly, the population of the *H*-like ions, the plasma is still dense enough to suppress the He_α line. The lower the Z target number is, the stronger is this effect.

Figure 6.10 a) shows the dependence of intensity ratio of the Li H_α and Li He_α resonance lines on the coating layer thickness, h_c, determined form the experimental spectra. For the uncoated *LiF* target the ratio intensity is $H_\alpha/He_\beta = 0.28 \pm 0.07$

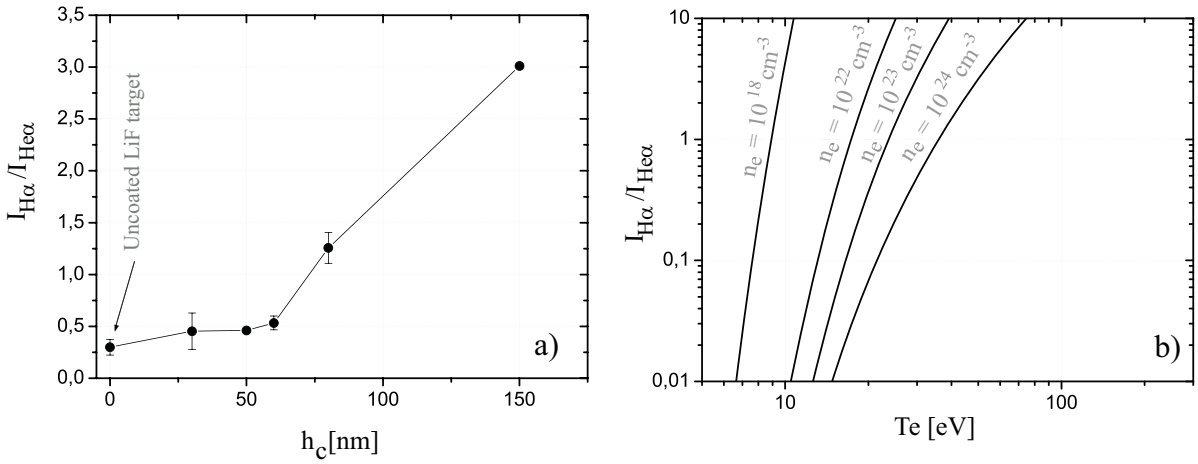

Figure 6.10: The intensity ratio of the Li H_α (199.28 Å) and Li He_α (134.99 Å) lines experimentally determined as function of Al layer thickness (plot a)). In plot b) the calculation results for the same intensity ratio using formula 6.2 are represented.

and it increases up to ≈ 3 at a thickness of $h_c = 150\,\mathrm{nm}$. The effect of the enhanced emission of the H_α in low-Z isochorically heated plasma was previously observed in different experiments (e.g. [8, 146]). The resonance lines intensity ratio of ions in successive ionization stages depends on the plasma temperature and density and thus, allows to estimate the physical parameters of the emitting plasma layers [32, 45]. In LTE approximation for the dense plasma, the ratio $I_{H_\alpha}/I_{H_\alpha}$ is given by [45]:

$$R = \frac{I_{H\alpha}}{I_{He\alpha}} = \left(\frac{\lambda}{\lambda'}\right)^3 \cdot \frac{f'g'}{fg} \cdot [4(\sqrt{\pi}a_0)^3 n_e]^{-1} \cdot \left(\frac{kT_e}{E_H}\right) \cdot \exp\left(-\frac{E' - E + E_\infty - \triangle E_\infty}{kT_e}\right). \tag{6.2}$$

The terms in the formula above are: λ-transition wavelength, f-the oscillator strength, g is the statistical weight of the upper transition level, E is the excitation energy, E_∞ is the ionization energy of the Li II ion and $\triangle E_\infty$ is its ionization potential depression; all prime terms refer to H_α line. Accounting for *MULTI-fs* simulation results, the plasma created in the LiF substrate has densities in the range of ($n_e = 10^{21} - 10^{23}\,\mathrm{cm}^{-3}$) and is highly collisional ($\nu_{ei} \approx 10^{16}\,\mathrm{s}^{-1}$). In dense plasmas, the LTE approximation is valid if the electron density satisfies the conditions 3.38 and 3.39. Thus, the conditions of LTE validity are fulfilled in the case of LiF plasma in temperature range of few hundreds of eV. The figure 6.10 b) represents the calculations of the intensity ratio Li H_α and Li He_α lines using the formula 6.2. The results show the dependence of the ratio R on a plasma parameters in terms of

density and temperature. For example, at a certain plasma density, the ratio is expected to increase with the plasma temperature. Synthetic spectra as LTE solution of *FLY* code indicate similar dependencies. These estimations should be regarded with care as long as they are valid under constant plasma parameters. The heat wave front propagating ahead into the targets determines temporal variations of the local temperature. Limited heat transport of the thermal electrons induces spatial gradients of the temperature. Consequently, spectral lines of the *H*- and *He*-like ions might originates from different target depths and have different emission moments and thus, deviations from LTE approximation can be expected.

The hot electrons and the radiation flux may have an important role in the ionization dynamics and energy deposition depth in the target layers [7, 87]. The collisionless absorption of the laser energy in the solid target will produce a certain fraction of superthermal electrons [72, 87] with energies in the range of few tens keV at laser intensities of about $10^{16}\,\mathrm{W/cm^2}$. The propagation of the hot electrons ahead of the thermal ones induces in the cold target processes like: radiation emission, ionization or local heating. The hot electrons are less collisional than the thermal electron population and deposit their energy deeper in the target. The free path of the hot electron is on the order of μm. Over target thicknesses in range of 100 nm, the main influence of the hot electrons is the fact that they represent an important source of X-ray radiation [109]. Thus, ionization and radiative processes balance are expected to be influenced. Further analysis of emission spectra using *FLYCKH* code [73] in the presence of hot electrons will aim to approach more realistically the emissivity of isochorically heated plasma layers.

Chapter 7

Summary and Outlook

In this thesis the interaction of high contrast, 8 fs laser pulse with high density plasmas generated on solid targets was studied. Starting from the main aim of understanding the fundamental physical processes which occurs when an ultrashort laser pulse is focused onto a solid surface, the experiments have been conducted in two investigation directions: absorption measurements and spectroscopic investigations of overdense plasmas. The experiments have been performed in a novel interaction regime benefiting from special laser pulse parameters. The very good laser contrast (10^8 on the ns time scale) assures the formation of a very small pre-plasma and the pulse interacts with the matter close to solid density. Due to extremely short duration, the expansion of the plasma is negligible during the main pulse interaction.

In the first part of this work the absorbed energy fraction was measured. The laser pulses were focused onto solid targets achieving within a focal spot of $\approx 3.2\,\mu$m diameter (FWHM) an average intensity of $5 \times 10^{16}\,\mathrm{W/cm^2}$. The absorbed energy fraction A was determined as $A = 1 - R$ where R is the reflected laser energy. The last one was measured by an Ulbricht sphere where the targets were enclosed during the interaction. The absorbed fraction may depend on several physical parameters like laser polarization and intensity, target type and surface roughness, laser incidence angle. In measurements these dependencies were taken into account.

The absorbed laser energy fraction by targets with a smooth surface (with roughnesses $\bar{\sigma}$ of about 2.5 nm) was investigated for two conductor targets, *Al* and *Au* and a dielectric one, *BK7 Glass*. For these targets the absorption of the p-polarized laser pulses significantly exceeds the s-polarization absorption. The experimental results proved that the energy of the ultra-short p-polarized laser pulses can be efficiently

absorbed up to 77% and the angle of maximum absorption is $\theta_{max} \geq 70°$. The dependence of the absorbed fraction on the laser intensity was also investigated for all targets types and angular incidence. These dependencies shows a threshold at an intensity of about $1 \times 10^{14}\,\mathrm{W/cm^2}$ corresponding to the plasma formation from where the absorption starts to increase with the laser intensity. From the experimental data the absorbed fraction scales with the laser irradiance as $A_p \sim (I_L \cdot \lambda)^{0.11\pm0.05}$ and $A_s \sim (I_L \cdot \lambda)^{0.20\pm0.04}$ for p- and s-polarized laser pulses, respectively. Assuming that the absorption of s-polarized laser pulses are preponderantly absorbed via collisional process and in the absorption of p-polarized laser pulses both, collisional and collisionless processes are involved, one can determine the collisionless contribution to the total absorption estimating the difference $A_p - A_s$. An important experimental observation was the fact that similar level of collisionless absorption have been measured within the error bars for all targets regardless of their type, conductor or dielectric at a certain laser intensity and incidence angle. This indicates that as soon as the solid target is ionized and the plasma is formed, the coupling of the laser energy is almost equally efficient for a certain geometry in the case of all investigated materials.

Similar measurements were performed for a BN target with rough surface ($\bar{\sigma} \approx$ 500nm) and the results were compared with corresponding ones of a smooth Au target. It was found that the absorbed energy fraction in BN case has an almost constant level of about $50-65\%$ independent of laser polarization and incidence angle. This was explained accounting for the target surface's non-uniformities which lead to a loss of angular and polarization geometry distinction over the focal spot. In this case, the measured absorption level represents an average over all incidence angles and linear polarization geometries. Thus, it was experimentally proved that rough targets absorb the laser energy more efficiently than a smooth one at angles close to normal incidence. The results are relevant for effects which rely on the absorbed energy fraction like hot electron and X-ray production by ultrashort laser pulses.

The interaction of the ultrashort laser pulses with solid targets was simulated using PSC PIC code. From the simulations it was aimed to calculate the absorbed energy fraction and the dependencies of the absorption on different parameters studied experimentally. A solid target was placed in the middle of a $2D$ simulation box. A 10 fs laser pulse at an intensity similar to the experiment was focused onto the target under different incidence angles. The field ionization was included in the code

and the binary collisions between macro-particles were considered. The preplasma was simulated by including a expanded target profile characterized by a certain scale length. The Poynting vector of the laser pulse was determined before and after the pulse being reflected by the target. Systematic simulations have been performed covering the angular and the intensity laser ranges from the experiments. Similar with the experimental data evaluation, the collisionless absorption level was determined from the simulation results for each incidence angle and laser intensity. The high level of about $50 - 60\%$ of the collisionless absorption at 70° was confirmed by the simulations in the case of steep plasma profiles. The good agreement of the simulation results with the experimental data for angular and laser intensity dependencies was found for a target profile $L/\lambda \approx 1\%$. The simulations indicate that, as effect of field ionization, the target is fast ionized reaching at the peak of the pulse an electron density of about 80 times larger than the critical density. During the pulse interaction the target is in overdense, the expansion is negligible and the laser interacts basically with matter at densities close to solid.

The validity of the proposed absorption mechanisms in the non-relativistic regime was analyzed accounting for the experimental and simulation results. The results of PIC simulation and previous experiments [134, 144, 145] indicate that in our interaction regime a preplasma with a very steep profile is created prior the main pulse. The classical model of *linear resonance absorption* [71] is not valid in these steep profiles as long the plasma frequency ω_p is much higher than the laser frequency ω. The contributions of different collisionless skin effects (*anomalous skin effect* (ASE) and *sheath inverse bremsstrahlung* (SIB)) were estimated and found very small, in order of a few percents. Due to moderate temperature of the plasma (estimated from the spectroscopic investigations in the order of few hundreds of eV) the skin layer is highly collisional during the main pulse interaction and thus, these processes are not so effective. The *vacuum heating (VH)* is considered one of the most efficient absorption mechanisms in plasmas with steep density gradients [79, 86, 108]. This process is characterized by some particular scaling laws manifested in specific dependencies on the incidence angle and laser intensity. Our experimental data does not reveal these dependencies and the condition required by this model, namely that the electron quiver amplitude to be larger than the plasma profile, is fulfilled only at the peak of the pulse, for about one laser cycle. Thus, without excluding the possibility that *VH* plays a role to the total amount of absorption, it was not possible to distinctly identified its contribution from the experimental data.

The new model of *anharmonic resonance absorption (ARA)* [72] is considered a favorable candidate which may explain the experimental observations. In the experimental regime where *ARA* is expected to occur, one has to ensure that the laser pulse is ultrashort (femtosecond) and has a good contrast so that the plasma profile is kept very small during the main interaction and the linear resonance absorption is prevented to occur. The model predicts an efficient coupling of the laser energy to overdense matter assuming a resonant laser energy transfer in a nonlinear regime. The threshold for the absorption onset found experimentally is predicted by the model and analytical estimations show an agreement with the experiment. The model development is currently in progress and additional experiments are planed to test quantitatively the theoretical predictions. For example, the threshold behavior predicted by the *ARA* model can be tested in the higher intensity regime. In addition, it is expected that experimental investigations of the absorption process of circular polarized laser pulses normally incident on steep gradient profiles can bring new information regarding the validity and the efficiency of the collisionless processes [72, 74].

In the second part of this work the *XUV* emission of the overdense plasmas was investigated. The ultrashort (8 fs) laser pulses with an average intensity of $5 \times 10^{16}\,\mathrm{W/cm^2}$ were focused onto low Z solid targets. At these laser intensities, high ionization states of light atoms are induced and K-shell emission of the ions in the *XUV* range is expected. In the experiments massive, solid targets (*LiF* and *BN*) and *LiF* substrates coated by *Al* layers of different thicknesses were employed. Time integrated emission spectra were recorded with a flat field, high resolution spectrometer built during this work. The analysis of the solid targets emission spectra reveals effects specific to plasmas at high density like higher series limit and dielectronic satellites emission. The lack of higher order resonance lines was explained by *pressure ionization*. Plasmas produced after an ultra fast laser heating process are highly transient and large temporal and spatial variation of its parameters occurs. The atomic process rates and balances depend on the plasma parameters and therefore, during the expansion the plasma emissivity changes significantly. In order to interpret the recorded spectra, the plasma expansion was simulated using the hydro-code *MULTI-fs*. The temporal evolution of the plasma parameters was further taken into account in the calculation of plasma emissivity and opacity performed with the atomic code *FLY*. The spectra calculated from simulations

where a preplasma of only few nm was included are in good agreement with the experimental ones. Synthetic spectra reproduce the main experimental observations namely, series limit of *H*- and *He*-like resonance lines, the intensity ratio of the resonance lines and emission of the satellites lines. Moreover, the simulation results indicate that the main contribution of the plasma emission in the time integrated spectra is coming from early, dense plasma stages. The temporal evolution of the ion population derived from collisional-radiative atomic calculations shows the effect of the pressure ionization in the ion population abundance in times intervals corresponding to dense plasma state. The investigation of a high density plasma was extended by generating isochoric heated plasmas in coated targets. Emission spectra of these targets allowed to estimated the *energy penetration depth* as a function of the coating layer thickness. The intensity ratio of the resonance lines corresponding to different thicknesses of the Al coating layer was calculated and compared with LTE calculations. The results indicate an increased density of the emitting plasma generated into the substrate. The effect of hot electrons on the energy deposition on the deeper target layers was discussed. Atomic calculations which accounts for the hot electron contributions in the plasma emissivity are further planed. This analysis is particular interesting for better understanding to the atomic physics in dense plasmas and ultrashort X-ray pulses production.

Chapter 8

Published Works

- J. Osterholz, F. Brandl, T. Fischer, D. Hemmers, M. Cerchez, G. Pretzler, O. Willi and R. J. Rose, *Production of Dense Plasmas with Sub-10-fs Laser Pulses*, Phys. Rev. Lett. **96**, 085002 (2006)

- M. Cerchez, R. Jung, J. Osterholz, T. Toncian, O. Willi, P. Mulser and H. Ruhl, *Absorption of Ultrashort Laser Pulses in Strongly Overdense Targets*, Phys. Rev. Lett. **100**, 245001 (2008)

- J. Osterholz, F. Brandl, M. Cerchez, T. Fischer, D. Hemmers, B. Hidding, A. Pipahl, G. Pretzler, S. Rose and O. Willi, *Extreme Ultraviolet Emission from Dense Plasmas Generated with sub-10 fs Laser Pulses*, Phys. Plasmas **15**, 103301 (2008)

- M. Cerchez, R. Jung, J. Osterholz, T. Toncian, O. Willi, P. Mulser and H. Ruhl, *Absorption of Ultrashort Laser Pulses in Overdense Targets*, Progress Report **No3** of the PHELIX theory group, GSI/Darmstadt, 38 (2008).

Appendix A:
Reflection coefficients. Fresnel equations

In this section, the characteristic reflectivity curves of the polarized electromagnetic radiation for relevant materials studied in the investigation of the absorption process are presented. The calculations summarize the theoretical considerations developed in [162] and determine the Fresnel formulas which represent the reflectivity and transmission coefficients. The results were used to calibrate indirectly the Ulbricht sphere in the experiment described in 4.2.2 and to analyze the collisional absorption process by steep plasma profiles.

The energy transported by the electromagnetic field $(\vec{E}(t), \vec{B}(t))$ while propagating through a dielectric medium with a refractive index n can be characterized by intensity radiation. Considering physical constants of the medium (dielectric permittivity $\varepsilon = \varepsilon_0 \cdot \varepsilon_r$ and permeability $\mu = \mu_0 \cdot \mu_r$), one can define the intensity of the radiation field as time-averaged of the energy flux (Poynting vector):

$$I = \left\langle \left| S(\vec{t}) \right| \right\rangle = \frac{c^2 \cdot \varepsilon}{n^2} \cdot < \vec{E}(t) \times \vec{B}(t) >= \frac{\varepsilon_0 \cdot c}{2} \sqrt{\frac{\varepsilon_r}{\mu_r}} E_0^2 \ , \tag{8.1}$$

where c is the speed of light in vacuum and E_0 is the amplitude of the electric field. The refractive index of the medium is defined as $n = \sqrt{\varepsilon_r \mu_r}$. For materials used in the absorption measurements discussed in the chapter 5, the relative permeability is $\mu_r \simeq 1$ and the refractive index can be expressed as $n \simeq \sqrt{\varepsilon_r}$.

Let us consider an electromagnetic radiation of intensity of $I^{(i)}$ incident under an angle θ_i onto an interface Σ of two dielectric media characterized by the permittivities ε_{ri} and ε_{rt}, and by the corresponding refractive indexes (n_i and n_t). The energy of the incident radiation field is divided in two parts, the reflected $I^{(r)}$ and the transmitted $I^{(t)}$ energy and the propagation of the reflected and transmitted radiation takes place under the angles θ_i and θ_t, respectively. *Fresnel equations* express the reflected $\mathcal{R}$ and the transmitted $\mathcal{T}$ energy fraction of the emergent radiation

associated with the polarization of the incident radiation. The Fresnel coefficients are determined solving the wave equation across the media interface for p- and s-components of the radiation independently. They are usually written as:

$$\left.\begin{aligned}
\mathcal{R}_p &= \frac{I_p^{(r)}}{I_p^{(i)}} = \left(\frac{n_t\cos\theta_i - n_i\cos\theta_t}{n_t\cos\theta_i + n_i\cos\theta_t}\right)^2 \\
\mathcal{R}_s &= \frac{I_s^{(r)}}{I_s^{(i)}} = \left(\frac{n_i\cos\theta_i - n_t\cos\theta_t}{n_i\cos\theta_i + n_t\cos\theta_t}\right)^2 \\
\mathcal{T}_p &= \frac{I_p^{(t)}}{I_p^{(i)}} = \left(\frac{2n_i\cos\theta_i}{n_t\cos\theta_i + n_i\cos\theta_t}\right)^2 \\
\mathcal{T}_s &= \frac{I_s^{(t)}}{I_s^{(i)}} = \left(\frac{2n_i\cos\theta_i}{n_i\cos\theta_i + n_t\cos\theta_t)}\right)^2
\end{aligned}\right\} \quad \textit{Fresnel equations for dielectric media} \tag{8.2}$$

Considering the response of the real materials at the incident electric field, the relative permittivity can be expressed [162], in a general way, as a complex number

$$\widetilde{\varepsilon_r} = \varepsilon + \imath\cdot\frac{\sigma}{\omega}\ , \tag{8.3}$$

where σ is the conductivity of the medium and ω is the angular frequency of the electric field. Therefore, the refractive index of a *real material* becomes a complex quantity

$$\widetilde{n} = n + \imath\cdot k\ , \tag{8.4}$$

where n and k are the real and the imaginary part of the complex refractive index, respectively. The real part, n, determines the wave phase velocity as $v = c/n$, while k is referred as attenuation coefficient and expresses the damping (absorption) of the radiation propagating through the material.

Accounting for the values of the electrical permittivity and conductivity one can distinguish different classes of materials. Materials known as *conductors* absorb strongly the electromagnetic radiation due to their good conductivity and this effect can expressed by $\frac{\sigma}{\omega} \gg \varepsilon$. Low-loss materials are known as *dielectrics*, where $\frac{\sigma}{\omega} \ll \varepsilon$. For an *ideal dielectric* (homogeneous and isotropic), the absorption process is negligible, it is perfect transparent, has no conduction properties (i.e. $\sigma = 0$ and $\varepsilon_r \in \mathbb{R}_+$) and it is characterized only by the real part of the refractive index. In all real materials, the losses due to the absorption of the radiation in the medium cannot be avoided and this process is expressed by a complex permittivity and a

complex refractive index, as shown in 8.3, 8.4.

The complex permittivity $\widetilde{\varepsilon_r}$ of a material was estimated by the *Drude model* [115] and was found to be dependent on the radiation frequency, ω, on the free electron density n_e and on the electron-ion collision frequency ν_{ei}. Consequently, one can establish a relationship between the optical constants n and k and the microscopic characteristic quantities of the medium, like n_e and ν_{ei}, as follows,

$$\widetilde{\varepsilon_r} = \widetilde{n}^2 = (n + \imath \cdot k)^2 = 1 - \frac{\omega_p^2}{\omega^2} \cdot \frac{1}{1 + \widetilde{\nu}^2} + \imath \cdot \frac{\omega_p^2}{\omega^2} \cdot \frac{\widetilde{\nu}}{1 + \widetilde{\nu}^2} \ , \tag{8.5}$$

where $\omega_p = \sqrt{e^2 n_e / \varepsilon_0 m_e}$ is the plasma frequency of the free electrons and $\widetilde{\nu} = \nu_{ei}/\omega$ (the physical constants e, ε_0 and m_e represent the electron electric charge, free space permittivity and the electron mass, respectively).

Considering the Fresnel equations presented above (8.2), one can derive similar reflection and transmission coefficients replacing the real refractive index with the complex one. In this case, the Fresnel coefficients become complex. The real part of the coefficients determine the energy fraction of the emergent radiation (reflected or transmitted) and from the imaginary part could be derived the phase change of the radiations while reflecting or transmitting.

In the geometry of the interface Σ between two media described above, let us consider a particular case relevant where the first medium is an ideal dielectric of refractive index $n_i = n_1$ (e.g. vacuum) and the second is a real medium of refractive index of $n_t = n_2 + \imath \cdot k_2$. Consequently, the formulas 8.2 become:

$$\left.\begin{aligned}
\widetilde{\mathcal{R}_p} &= (\rho_p e^{\imath\phi_p})^2 = \left[\frac{(n_2 + \imath \cdot k_2)\cos\theta_i - n_1 \cos\theta_t}{(n_2 + \imath \cdot k_2)\cos\theta_i + n_1 \cos\theta_t}\right]^2 \\
\widetilde{\mathcal{R}_s} &= (\rho_s e^{\imath\phi_s})^2 = \left[\frac{n_1 \cos\theta_i - (n_2 + \imath \cdot k_2)\cos\theta_t}{n_1 \cos\theta_i + (n_2 + \imath \cdot k_2)\cos\theta_t}\right]^2 \\
\widetilde{\mathcal{T}_p} &= (\tau_p e^{\imath\chi_p})^2 = \left[\frac{2n_1 \cos\theta_i}{(n_2 + \imath \cdot k_2)\cos\theta_i + n_1 \cos\theta_t}\right]^2 \\
\widetilde{\mathcal{T}_s} &= (\tau_s e^{\imath\chi_s})^2 = \left[\frac{2n_1 \cos\theta_i}{n_1 \cos\theta_i + (n_2 + \imath \cdot k_2)\cos\theta_t)}\right]^2
\end{aligned}\right\} \ . \tag{8.6}$$

After some algebra, separating the real part of the complex terms, one can evaluate the Fresnel coefficients for a particular geometry and for each polarization component

as:

$$\left.\begin{aligned}
\mathcal{R}_p = (\rho_p)^2 &= \frac{[(n_2^2-k_2^2)\cos\theta_i - n_1 u_2]^2 + [2n_2k_2\cos\theta_i - n_1 v_2]^2}{[(n_2^2-k_2^2)\cos\theta_i + n_1 u_2]^2 + [2n_2k_2\cos\theta_i + n_1 v_2]^2} \\
\mathcal{R}_s = (\rho_s)^2 &= \frac{(n_1\cos\theta_i - u_2)^2 + v_2^2}{(n_1\cos\theta_i + u_2)^2 + v_2^2} \\
\mathcal{T}_p = (\tau_p)^2 &= \frac{4(n_2^2+k_2^2)^2\cos^2\theta_i}{[(n_2^2-k_2^2)\cos\theta_i + n_1 u_2]^2 + [2n_2k_2\cos\theta_i + n_1 v_2]^2} \\
\mathcal{T}_p = (\tau_p)^2 &= \frac{(2n_1\cos\theta_i)^2}{(n_1\cos\theta_i + u_2)^2 + v_2^2}
\end{aligned}\right\}, \tag{8.7}$$

where the factors u_2 and v_2 are given by

$$\left.\begin{aligned}
u_2 &= \frac{1}{\sqrt{2}}\left[n_2^2 - k_2^2 - n_1^2\sin^2\theta_1 + \sqrt{(n_2^2-k_2^2-n_1^2\sin^2\theta_1)^2 + 4n_2^2k_2^2}\right]^{1/2} \\
v_2 &= \frac{1}{\sqrt{2}}\left[-n_2^2 + k_2^2 + n_1^2\sin^2\theta_1 + \sqrt{(n_2^2-k_2^2-n_1^2\sin^2\theta_1)^2 + 4n_2^2k_2^2}\right]^{1/2}
\end{aligned}\right\}. \tag{8.8}$$

In table 8.1 the optical constants (the real n and imaginary k part of the refractive index) at wavelength $\lambda = 800\ nm$ for a number of target materials are listed which were investigated in the energy absorption measurements. The optical constants (n, k) were determined from the experimental data of the reflectivity using Kramers-Kronig transformation (see references on the footnotes of table 8.1). For the *Aluminium* surface, at this wavelength and at room temperature, there are not significant differences between (n, k) values for evaporated metallic Al films (reference [1]) and bulk targets (reference [5]). In figure 8.1 the angular dependence of

Table 8.1: Values of the real n and imaginary k refractive index for solid materials used in the experiment at λ=800 nm.

	Aluminum [1],[5]	Gold [2]	Boron nitride [3]	Glass (BK7)[4]
n	2.8 (2.74)	0.18	1.607	1.5
k	8.45 (8.3)	5.125	0.17	$1.3 \cdot 10^{-8}$

[1] D.Y.Smith et al.,*Handbook of Optical Constants of Solids I*, Ed. by E. D. Palik, New York, Academic Press (1985)

[2] D.W.Lynch and W.R.Hunter, *Handbook of Optical Constants of Solids II*, Ed. by E. D. Palik, New York, Academic Press (1985)

[3] G.L.Doll, *Handbook of Optical Constants of Solids III*, New York, Ed. by E. D. Palik, Academic Press (1985)

[4] *Laser Components Data Sheets*

[5] E. Shiles et al, Phys. Rev. B **22** 1612 (1980)

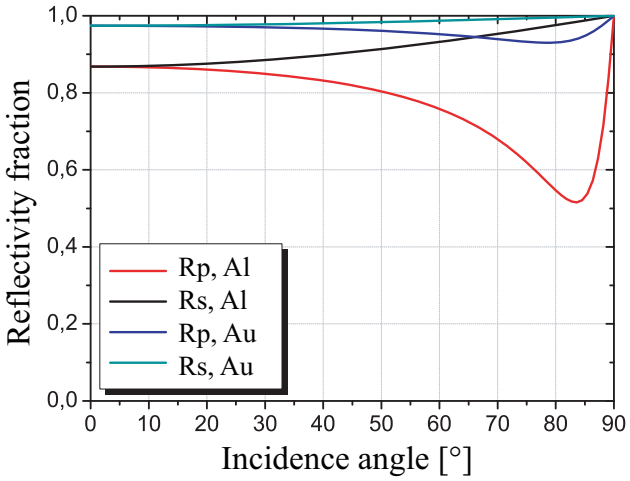

Figure 8.1: Angular dependence of the reflectivity fraction (Fresnel coefficients) R_p and R_s for p- and s-polarized radiation, respectively, at room temperature, for *Aluminum* and *Gold* targets.

reflectivity curves for conductors (Al and Au) are estimated using the Fresnel formulas (8.7 and 8.8) in the geometry described above. The calculations considered both polarization, p and s, of the incident radiation. For these target materials, the optical constants are characteristic for flat surfaces where polarization geometries are distinct and well defined. It is worth mentioning the special case of BN material which presents an inhomogeneous polycrystalline surface structure that leads to anisotropic optical properties. Due to the manufacturing procedure (hot-pressed powder) and mosaic spatial spread of the polycrystalline facets, it is difficult to make a distinction between the polarization geometries. Therefore, the optical constants (n, k) available in the literature for BN are derived from experimental data which contain a mixture of the polarizations (see reference [3] in the table 8.1 and the references therein).

Appendix B:

Numerical methods in modeling laser-plasma interaction

The laser produced plasmas characterized by dynamic changes in parameters and evolution are often numerically modeled, accounting for the particular interaction regimes, either by hydrodynamic (fluid) or kinetic codes. In hydro-codes the plasma is described by the fluid model which accounts for macroscopic quantities like density, temperature, pressure, mean velocity. The plasma parameters evolve accordingly with conservation laws of mass, momentum and energy in connection with Maxwell equations. Within hydro-codes it is assumed that plasma parameters are in a local thermodynamic equilibrium which can be a severe approximation when modeling rapidly changing states of plasma heated by ultrashort laser pulses [2]. The need for addressing non-linear, kinetic processes which accompany laser-plasma interaction (particles acceleration, collective plasma heating, etc.) gets an answer from the kinetic codes. Solving the equations for a large number of particles coupled by Maxwell's equations, the *Particle-in-Cell (PIC)* codes proved to be a suitable method for analyzing highly transient physical processes in the non-linear regime associated with ultrafast laser energy coupling to matter. [87, 157, 159].

B.1. Kinetic codes. The *PIC* Plasma Simulation Code (PSC)

In a kinetic approach, the plasma is an assembly of a large number of particles of different species: electrons, ions in different ionization stages and neutral atoms freely moving in the average microfields of charged particles in addition to the laser field.

In order to overcome the difficulty of modeling the dynamics of each single particle of a real systems, in the numerical technique proposed by *PIC* a large number of real particles are represented by a discrete *macro-* or *quasi-particle*. The dynamic of these macro-particles in the space phase are fully described in a *collisionless* approach by *Vlasov equation*:

$$\frac{\partial f_j}{\partial t} + \vec{v} \cdot \frac{\partial f_j}{\partial \vec{x}} + \frac{q_j}{m_j} \left(\vec{E} + \vec{v} \times \vec{B} \right) \cdot \frac{\partial f_j}{\partial \vec{v}} = 0 \tag{8.9}$$

combined with Maxwell's equations. In the equation 8.9, $f_j(t, \vec{x}, \vec{v})$ is the distribution function of the particles of specie j=e, i (as the particles are electrons or ions), t, $\vec{x}$ and $\vec{v}$ are respectively the time, the particle position and velocity in the phase space while $\vec{E}$ and $\vec{B}$ are the local fields. A basic *PIC* simulation cycle for one time step follows the stages summarized in the scheme 8.10 [71, 112].

$$\{\vec{r}_j, \vec{v}_j\} \xrightarrow[\text{the sources}]{\text{Calculate}} (\rho, \vec{J}) \xrightarrow[\text{on the grid}]{\text{Maxwell eq's}} (\vec{E}_g, \vec{B}_g) \xrightarrow[\text{interpolation}]{\text{Fields'}} (\vec{E}, \vec{B}) \xrightarrow[\text{coordinates}]{\text{New}} \{\vec{r}_j, \vec{v}_j\} \circlearrowleft \tag{8.10}$$

The positions and velocities of the particles are defined within a spatial grid at a moment of time. The charge density ρ and current $\vec{J}$ are derived from the particles local positions and velocities. In the next step, accounting for the sources calculated in the previous step and solving the Maxwell equation, one obtains the fields $\vec{E}_g$ and $\vec{B}_g$ in the grid points. The fields are further interpolated as local solutions in the particles positions. Including the fields in the particles' equation of motion, the new coordinates of the macro-particles are calculated and considered for the next simulation cycle. In a *collisional* approach one should consider that the distribution function obeys the *Vlasov-Boltzmann equation*. This represents the Vlasov equation 8.9 completed with a collisional term $(\frac{\partial f_{jk}}{\partial t})_c$ which is the rate of change of the distribution function f_j of the particle species j due to collisions with the k^{th} species particle [71].

The *PIC* Plasma Simulation Code (PSC)

The plasma model considered in the code accounts for a fully relativistic Vlasov-Boltzmann equation coupled with Maxwell equation for the fields. The code is structured in modules including Maxwell solver for the electromagnetic fields, Vlasov solver for particle distribution and the collisional module. The collisions are of key importance in modeling the high density plasmas and they are included in the code

as binary collisions using a numerical method known as Monte-Carlo Particle-in-Cell. To simulate the ionization processes and the dynamics of different ionization states, the code accounts for the field ionization of the neutrals and ions included through the *ADK* ionization rates [160].

Initial parameters of *2-D* simulation

The $3-D$ simulation box defined in a $(0xyz)$ coordinate system was set up with the dimensions $20\,\mu\text{m} \times 20\,\mu\text{m} \times 20\,\mu\text{m}$ and $200 \times 800 \times 800$ grid points. A cross-section of the simulation box in the $0yz$ plane is presented in the figure 8.2. It allows to visualize the interaction configuration and to set the parameters which will be detailed below. In the middle of the simulation box ($x_0, y_0, z_0 = 10\,\mu\text{m}$) was placed a parallelepipedic target with a length of $15\,\mu\text{m}$ and a width $1\,\mu\text{m}$, in $0yz$-plane and the height was $10\,\mu\text{m}$. The target was defined in its own coordinate system $(0x_t y_t z_t)$ having the same origin with the simulation box frame. Within the code an overlap of these two systems was used. For all the simulations reported here, the simulation grid was filled with 4 particles per cell and species. The neutral particles have been set with a density n_{n0} similar to the solid density of the investigated materials ($n_{n0,Al} = 6 \cdot 10^{22}\,\text{cm}^{-3}$ for *Aluminium*, $n_{n0,Au} = 5.9 \cdot 10^{22}\,\text{cm}^{-3}$ for *Gold*). The density profile of the target at the boundaries was given by

$$n_n(q) = \frac{n_{n0}}{(1 + \exp(-2x/L))} \tag{8.11}$$

where $L = |\nabla n/n_0|^{-1}$ is the density scale length which had the same value for all target coordinates (q=x_t, y_t, z_t). The density profile in the direction perpendicular to the target is shown in the plot *a*) of figure 8.2. Similar to the experimental conditions, the target was rotated in steps of 10° around the position of the maximum density slope located at the best focal position (i.e. corresponding to $n/n_0 = 1/2$). The target frame was co-rotating with the target keeping the density profile constant for any target angular orientation.

The laser pulse of a central wavelength $\lambda = 800\,\text{nm}$ was included by its electric field propagating along the z-axis. Both polarization geometries were simulated; the electric field was defined oscillating in y- or x-direction for the $p-$ or $s-$ polarized laser pulse, respectively. The focusing angle of the laser pulse was $\theta_{FF} = 9°$ and consequently, a focal spot with a diameter of $\approx 2\,\mu\text{m}$ ($FWHM$) (compare with the formula 4.10). The laser pulse is initialized at the simulation box boundary

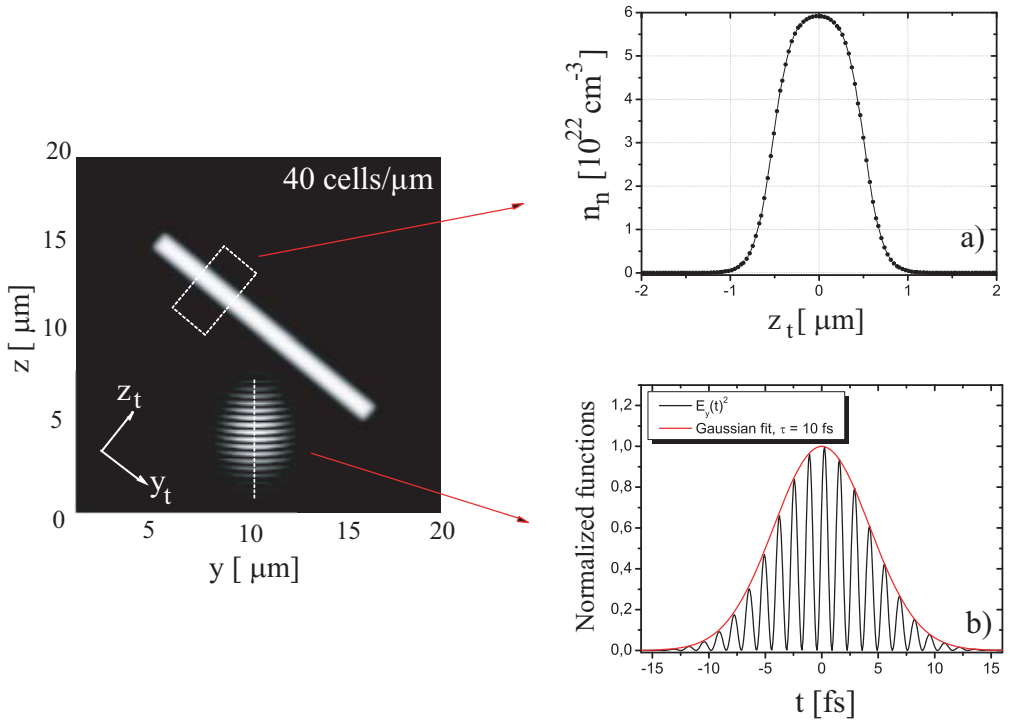

Figure 8.2: Simulation box geometry in (0yz) plane cross-section showing the target position and the 10 fs laser pulse propagating inside of the box. The target density profile is presented in the plot a); here, with a scale length $L = 200\,\mathrm{nm}$. In plot b) the temporal dependence of the normalized squared electric field of the laser pulse and the Gaussian envelope of the laser intensity are presented.

$(z = 0)$ with an average intensity of $1 \times 10^{16}\,\mathrm{W/cm^2}$ reaching in the focal position an intensity of $2 \times 10^{16}\,\mathrm{W/cm^2}$ (cycle average). In figure 8.2 *b*) the temporal shape of the normalized intensity of the laser pulse is shown. The Gaussian fit of the envelope reveals a pulse duration of $\triangle t = 10\,\mathrm{fs}$. In the simulations were considered radiative boundary conditions for the fields and particles in x- direction, while in y- and z- direction the radiating conditions for the fields and periodical for the particles were included.

B.2. Hydrodynamic codes. *MULTI-fs* code

Hydro-codes are able to model spatio-temporally the evolution of the macroscopic plasma parameters accounting for the collective behavior of the constituents (electron and ions). In principal, a hydrocode includes a number of equations based on the physical processes considered. They can be summarized as follows:

- *Hydrodymanics*. The fluid equations include the *mass*, *momentum* and *energy* conservation laws and can be considered for both plasma species: electrons and ions. The fluid equations for electrons and ions are coupled by a collisional term.

- *Ionization processes*. The ionization degree calculations are based on algorithms which include different atomic models (Thomas-Fermi, Debye-Hückel [32]) or ionization rate equations. Depending on the validity regime, the ionization rates can be treated in LTE, non-LTE or collisional-radiative approximation.

- *Transport processes*. The heat and thermal conduction processes in the plasma are most often described in the Spitzer-Härm approximation. The transport coefficients are derived considering a Maxwell distribution for the electrons, the main carriers in the transport processes. Different interpolation methods can be used for extending the transport models over larger domains of plasma states (strong gradients, degenerated states) (e.g. [140, 141]) .

- *Matter state*. The macroscopic fluid parameters (pressure, temperature, density) are coupled by equations of state (EOS). These equations are derived assuming different statistical models like ideal gas or Thomas-Fermi and are included in the codes in tabulated form.

- *Laser propagation*. In the most accurate hydro-codes, for the laser propagation, the Maxwell equations are solved by a wave-solver accounting for local plasma refractive index.

The hydro-codes have been widely used for describing the expansion of plasmas heated by long laser pulses (in *ps* and *ns* time regimes). In order to account for the specific phenomena of short laser pulse interaction with matter like fast heating processes or highly transient plasma parameters, in recent developed codes new

physical models and interpolation methods are included. One of these codes is *MULTI-fs* [140] described in the following section.

MULTI-fs code and simulation conditions

The *MULTI-fs* code is an 1D Langragian hydro-code and represents an optimized version of multigroup radiation hydrocode *MULTI* [142] extending the simulation regime from picosecond to femtosecond pulse duration. The main modifications considered in *MULTI-fs* for this purpose can be summarized as follows: *(i)* the laser propagation in an inhomogenous plasma is calculated by solving Maxwell's equations in a high resolution grid appropriate for calculating the laser propagation in steep plasma gradients; *(ii)* accounting for the rapidly changes on a solid target heated by ultrashort laser pulses, the electron-ion collision frequency is introduced as an interpolation over a larger plasma state range: from cold, solid state (where the electron-phonon collision frequency was taken into account) up to hot, low density plasma state (where the electron-ion collision frequency is given by Spitzer formula, see equation 3.20); *(iii)* more accurate tables of EOS's for electrons and ions are considered from SESAME library.

In 1D hydrodynamic simulations performed in this thesis to model the plasma expansion after been heated by 8 fs laser pulse the following simulation conditions have been considered. The target was divided in $N = 160$ Lagragian cells with thickness starting from 0.5 nm and increased linearly by a factor of 1.08-1.11 towards to inner cells of the target. The high spatial resolution of the front layers allows the accurate calculation of the steep plasma gradients. For the temporal resolution, times steps of $\Delta t_i = 1$ fs were chosen for time intervals near to the peak of the pulse, while larger times steps of $\Delta t_j = 100$ fs were considered for time intervals before and after the laser pulse. The laser pulse had a Gaussian shape in time with a duration of 8 fs (FWHM). Accounting for the previous experimental and simulation results for absorption measurements regarding the existence of a thin preplasma in front of the target, in the hydrodynamic simulations a prepulse was considered It deposited 1% of the main pulse energy onto the target prior to the peak interaction. Thus, a preplasma with a scale length of few nm was modeled. In the *MULTI-fs* simulations performed for interpreting the emission spectra in this thesis, a flux limiter of $f = 0.001$ was considered. The collisional absorption level of the laser energy is in agreement with the experimental results for solid targets.

B.3. Atomic physics code - *FLY*

FLY is a suite of 3 computer codes able to calculated the dynamics of the atomic processes in specific plasma conditions [47]. The codes (*FLY*, *FLYPAPER* and *FLYSPEC*) provide a variety of information about the hydrogen-, helium- and lithium-like ionic species of elements with atomic number from $Z = 2$ to $Z = 26$ and the most important outputs are the synthetic K-shell emission spectra.

The main code *FLY* is a collisional-radiative code which includes a large atomic datebase for the ion stages, like statistical weight and ionization potential. The code calculates the populations of the excited states as a function of temperature and density or time accounting for the rate coefficients of the collisional and radiative transitions. These calculations can be performed in three different kinetic models depending on the particular simulated plasma conditions: LTE, steady-state (s-s) or time-dependent. In time independent cases (LTE and s-s), the ionization stages are calculated by Saha equation, while the excited states are given by Boltzmann equation [32]. In the time-dependent calculations, the plasma parameters can be introduced into the code as a history of plasma temporal evolution and an iterative scheme is implemented for considering the opacity effects on the population distributions. Some specific effects of dense plasmas are included (see paragraph 3.4). The pressure ionization effect is taken into account in the rate equations for the ionization processes and the populations in double excitated states are calculated (that will be further used to calculate the emission of dielectronic satellites). The main input parameters are: the atomic number of the analyzed element, the initial condition (LTE or s-s) and the model for the population calculation (LTE, s-s or time dependent). For the later case, a temporal evolution file should be provided to be read by the code. The FLY code is commonly used in combination with hydrocodes which provide the "history" file of the plasma parameters' evolution. The population distribution results as code output and is further considered as input data in the two other codes of the suite.

The *FLYPAPER* calculates the ratio of spectral line intensities or population dependence on different simulation parameters like density, temperature or time. The synthetic spectra emitted in a specific plasma state (density, temperature) is calculated by *FLYSPEC*. In the case of time-dependent calculations, depending of the structure of the "history files" a synthetic spectra is produced at each time step and for each plasma layer. The detailed calculation of the spectral resonance line

profile is possible accounting for Stark and Doppler effect on line broadening. The dielectronic satellite line structures are not calculated in the version of the code used here. Note that the*FLY* code is a non-dimensional code but in combination with hydrocodes and particular post-processing procedures, one can for example, simulates the emission by a plasma in a 1D geometry integrating the contribution of each plasma layer to the total emission accounting for the radiation transport and opacity effects (refer to the paragraph 6.1.2 and spatial-temporal integration method described in [145]).

Bibliography

[1] P. Gibbon and E Förster, *Short-Pulse Laser-Plasma Interaction*, Plasma Phys. Control. Fusion **38**, 769 (1996).

[2] Shalom Eliezer, *The Interaction of High-Power Lasers with Plasmas*, Institute of Physics Publishing, Bristol and Philadelphia (2002).

[3] T. H. Maiman, *Stimulated Optical Radiation in Ruby*, Nature **187**, 493 (1960).

[4] T. Feder, *Petawatt Laser Probes Nature at Texas University*, Physics Today **10**, 27 (2008).

[5] M. Tabak, J. Hammer, M. E. Glinsky, W. L. Kruer, S. C. Wilks, J. Woodworth, E. M. Campbell and M. D. Perry, *Ignition and High Gain with Ultrapowerful Lasers*, Phys. Plasmas **1**, 1626 (1994).

[6] J. D. Kmetec, C. L. Gordon, III, J. J. Macklin, B. E. Lemoff, G. S. Brown, and S. E. Harris, *MeV X-Ray Generation with a Femtosecond Laser*, Phys. Rev. Lett. **68**, 1527 (1992).

[7] U. Teubner, I. Uschmann, P. Gibbon, D. Altenbernd, E. Förster, T. Feurer, W. Theobald, R. Sauerbrey, G. Hirst, M. H. Key, J. Lister, and D. Neely, *Absorption and Hot Electron Production by High Intensity Femtosecond UV-Laser Pulses in Solid Targets*, Phys. Rev. E **54**, 4167 (1996).

[8] A. Saemann, K. Eidmann, I. E. Golovkin, R. C. Mancini, E. Andersson, E. Förster, and K. Witte, *Isochoric Heating of Solid Aluminum by Ultrashort Laser Pulses Focused on a Tamped Target*, Phys. Rev. Lett. **82**, 4843 (1999).

[9] S. J. Rose, *High-Power Laser-Produced Plasma and Astrophysics*, Laser Part. Beams **4**, 864 (1991).

[10] C. S. Grigoropoulos, *Lasers, Optics and Thermal Considerations in Ablation Experiments* in *Laser Ablation and Desorption*, J. C. Miller and R. F. Haglund (ed.), Academic Press, San Diego (1998).

[11] S. Amoruso, R. Bruzzese, N. Spinelli and R. Velotta, *Characterization of Laser-Ablation Plasmas*, J. Phys. B: At. Mol. Opt. Phys. **32**, 131-172 (1999).

[12] S. Amoruso, *Modeling of UV Pulsed-Laser Ablation of Metallic Targets*, Appl. Phys. A **69**, 323 (1999).

[13] E. G. Gamaly, A. V. Rode, B. Luther-Davies and V. T. Tikhonchuk, *Ablation of Solids by Femtosecond Laser: Ablation Mechanism and Ablation Thresholds for Metals and Dielectrics*, Phys. Plasmas **9**, 949 (2002).

[14] A. M. Komashko, M. D. Feit, A. M. Rubenchik, M. D. Perry and P. S. Banks, *Simulation of Material Removal Efficiency with Ultrashort laser pulses*, Appl. Phys. A **69**, S95-S98 (1999).

[15] B. N. Chichkov, C. Momma, S. Nolte, F. von Alvensleben and A. Tünnemann *Femtosecond, Picosecond and Nanosecond Laser Ablation of Solids*, Appl. Phys. A **63**, 109, (1996).

[16] P. P. Pronko, S. K. Dutta, D. Du and R. K. Singh *Thermophysical Effects in Laser Processing of Materials with Picosecond and Femtosecond Pulses*, J. Appl. Phys. **78**, 6233 (1995).

[17] K. B. Wharton, C. D. Boley, A. M. Komashko, A. M. Rubenchik, J. Zweiback, J. Crane, G. Hays, T. E. Cowan, and T. Ditmire, *Effects of Non-ionizing Prepulses in High-Intensity Laser-Solid Interactions*, Phys. Rev. E **64**, 025401 (2001).

[18] K. B. Wharton, J. M. Kim and B. C. Stuart, *Effects of Nanosecond-Duration Laser Prepulses on Solid Targets*, J. Appl. Phys. **97**, 103303 (2005).

[19] B. Le Drogoff, F. Vidal, Y. von Kaenel, M. Chakel, T. W. Johnson, S. Laville, M. Sabsabi and J. Margot, *Ablation of Aluminum Thin Films by Ultrashort Laser Pulses*, J. Appl. Phys. **89**, 8247, (2001).

[20] L. Kubicar, V. Vretenar and U. Hammerschmidt *Thermophysical Parameters of Optical Glass BK7 Measured by the Pulse Transient Method*, International Journal of Thermophysics **26**, 507 (2005).

[21] S. Preuss, A. Demchuk and M. Stuke, *Sub-picosecond UV Laser Ablation of Metals*, Appl. Phys. A **61**, 33-37 (1995).

[22] W. Kautek, J. Krüger, M. Lenzner, S. Sartania, C. Spielmann and F. Krausz, *Laser Ablation of Dielectrics with Pulses Duration between 20 fs and 3 ps*, Appl. Phys. Lett. **69**, 3146 (1996).

[23] J. C. Gauthier, *Dense Ultrafast Plasmas* in *Atoms, Solids and Plasmas in Super-Intense Laser Fields*, edited by D. Batani et al., Kluwer Academic/Plenum Publishers, New York (2001).

[24] L. V. Keldysh, *Ionization in the Field of a Strong Electromagnetic Wave*, Sov. Phys. JETP Lett. **20**, 1307 (1965).

[25] X. Liu and D. Umstadter, *Competition between Ponderometive and Thermal Forces in Short-Scale-Length Laser Plasmas*, Phys. Rev. Lett. **69**, 1935 (1992).

[26] S. C. Wilks, W. L. Kruer, M. Tabak and A. B. Langdon, *Absorption of Ultra-Intense Laser Pulses*, Phys. Rev. Lett. **69**, 1383 (1992).

[27] A. J. Kemp, R. E. W. Pfund and J. Meyer-ter-Vehn, *Modeling Ultrafast Laser-Driven Ionization Dynamics with Monte Carlo Collisional Particle-in-Cell Simulations*, Phys. Plasmas **11**, 5648 (2004).

[28] R. E. W. Pfund, *Inelastische Prozesse in Ultra-Kurtzer Laser-Materie-Wechselwirkung*, Dissertation, TU Berlin, Berlin (1999).

[29] B. M. Penetrante and J. N. Bardsley, *Residual Energy in Plasmas Produced by Intense Subpicosecond Lasers*, Phys. Rev. A **43**, 3100 (1991).

[30] T. Brabec and F. Krausz, *Intense Few-Cycle Laser Fields: Frontiers of Nonlinear Optics*, Reviews of Modern Physics **72**, 545 (2000).

[31] K. Burnett, V. C. Reed and P. L. Knight, *Atoms in Ultra-Intense Laser Fields*, J. Phys. B: At. Mol. Opt. Phys. **26**, 561-598 (1993).

[32] D. Salzmann, *Atomic Physics in Hot Plasmas*, Oxford University Press, New York (1998).

[33] M. Nantel, G. Ma, S. Gu, C. Y. Côté, J. Itatani, and D. Umstadter, *Pressure Ionization and Line Merging in Strongly Coupled Plasmas Produced by 100-fs Laser Pulses*, Phys. Rev. Lett. **80**, 4448 (1998).

[34] J. C. Stewart and K. D. Pyatt, Jr., *Lowering the Ionization Potentials in Plamas*, Astrophys. J. **144**, 1203 (1966).

[35] R. M. More, *Electronic Energy-Levels in Dense Plasma*, J. Quant. Spectrosc. Radiat. Transfer **27**, 345 (1982).

[36] A. Maksimchuk, M. Nantel, G. Ma, S. Gu, C. Y. Côté, D. Umstadter, S. A. Pikuz, I. Yu. Skobelev, A. Ya. Faenov, *X-Ray Radiation from Matter in Extreme Conditions*, J. Quant. Spectrosc. Radiat. Transfer **65**, 367 (2000).

[37] H. F. Berg, A. W. Ali, R. Lincke and H. R. Griem, *Measurement of Stark Profiles of Neutral and Ionized Helium and Hydrogen Lines from Shock-Heated Plasmas in Electromagnetic T Tubes*, Phys. Rev. **125**, 199 (1991).

[38] O. Renner, E. Krousky, F. B. Rosmej, P. Sondhauss, I. Uschmann, E. Förster, M. P. Kalachnikov and P. V. Nickles *Overcritical Density Plasma Diagnosis inside Laser-Produced Craters*, Appl. Phys. Lett. **79**, 177 (2001).

[39] A. H. Gabriel and S. Volonte, *Measurement and Interpretation of Plasma Polarization Shift for Members of the Resonance Series of Ionized Helium*, J. Phys. B **6**, 2684 (1973).

[40] A. H. Gabriel and T. M. Paget, *Measurement and Interpretation of Dielectronic Recombination Satellites Line Intensities*, J. Phys. B. **5**, 673 (1972).

[41] Y. T. Lee, *A Model for Ionization Balance and L-Shell Spectroscopy of non-LTE Plasmas*, J. Quant. Spectrosc. Radiat. Transfer **38**, 131 (1987).

[42] U. Andiel, K. Eidmann, P. Hakel, R. C. Mancini, G. C. Junkel-Vives, J. Abdallah and K. Witte, *Demonstration of Aluminum K-Shell Line Shifts in Isochorically Heated Targets Driven by Ultrashort Laser Pulses*, Europhys. Lett. **60**, 861 (2002).

[43] K. Eidmann, A. Saemann, U. Andiel, I. E. Golovkin, R. C. Mancini, E. Andersson and E. Förster, *Generation of Hot Plasma at Solid Density by High-Contrast Ultra-Short Laser Pulses*, J. Quant. Spectrosc. Radiat. Transfer **65**, 173 (2000).

[44] F. B. Rosmey, A. Ya. Faenov, T. A. Pikuz, I. Yu. Skobelev, A. E. Stepanov, A. N. Starostin, V. S. Rerikh, V. A. Makhrov, F. Flora, S. Bollanti, P. Di Lazzaro, T. Letardi, K. Vigli-Papadaki, A. Nottola, A. Grilli, L. Palladino, A. Reale, A. Scafati and L. Reale, *Dominant Role of Dielectronic Satellites in the Radiation Spectra of a Laser Plasma near the Target Surface*, JETP Lett. **65**, 709 (1997).

[45] H. R. Griem, *Principles of Plasma Spectroscopy*, Cambridge University Press (1997).

[46] H. R. Griem, *Plasma Spectroscopy*, McGraw-Hill, New York (1964).

[47] R.W. Lee and J.T. Larsen, *A Time-Dependent Model for Plasma Spectroscopy of K-Shell Emitters*, J. Quant. Spectrosc. Radiat. Transfer **56**, 535 (1996).

[48] D. Salzmann and H. Szichman, *Density Dependence of the Atomic Transition Probalilities in Hot, Dense Plasmas*, Phys. Rev. A **35**, 807 (1987).

[49] L. Kelly, *Atomic and Ionic Spectrum Lines below 2000 Angstroms: Hydrogen through Krypton*, J. Phys. Chem. Ref Data, **16**, Suppl.1 (1987).

[50] M. Göppert-Mayer, *Elementary processes with two quantum jumps*, Ann. Physik **9**, 273 (1931).

[51] P. Audebert, P. Renaudin, S. Bastiani-Ceccotti, J.-P. Geindre, C. Chenais-Popovics, S. Tzortzakis, V. Nagels-Silvert, R. Shepherd, I. Matsushima, S. Gary, F. Girard, O. Peyrusse and J.-C. Gauthier, *Picosecond Time-Resolved X-Ray Absorption Spectroscopy of Ultrafast Aluminum Plasmas*, Phys. Rev. Lett. **94**, 025004 (2005).

[52] P. Agostini, F. Fabre, G. Mainfray, G. Petite, and N. Rahman, *Free-Free Transitions Following Six-Photon Ionization of Xenon Atoms*, Phys. Rev. Lett. **42**, 1127 (1979).

[53] S. Augst, D. Strickland, D.D. Meyerhofer, S.L. Chin, and J.H. Eberly, *Tunneling Ionization of Noble Gases in a High-Intensity Laser Field*, Phys. Rev. Lett. **63**, 2212 (1989).

[54] M. V. Ammosov, N. B. Delone and V. P. Krainov, *Tunnel Ionization of Complex Atoms and of Atomic Ions in an Alternating Electromagnetic Field*, Sov. Phys. JETP Lett. **64**, 1191 (1986).

[55] W. Lotz, *An Empirical Formula for the Electron-Impact Ionization Cross-Section*, Z. Physik **206**, 205 (1967).

[56] W. Lotz, *Electron-Impact Ionization Cross-Sections and Ionization Rate Coefficients for Atoms and Ions from Hydrogen to Calcium*, Z. Physik **216**, 241 (1968).

[57] A. Kaiser, B. Rethfeld, M. Vicanek and G. Simon, *Microscopic Processes in Dielectrics under Irradiation by Subpicosecond Laser Pulses*, Phys. Rev. B **61**, 11437 (2000).

[58] V. R. Bhardwaj, P. P. Rajeev, P. B. Corkum and D. M. Rayner, *Strong Field Ionization inside Transparent Solids*, J. Phys. B: At. Mol. Opt. Phys. **39**, 397 (2006).

[59] N. M. Bulgakova, R. Stoian, A. Rosenfeld, and I. V. Hertel and E. E. B. Campbell, *Electronic Transport and Consequences for Material Removal in Ultrafast Pulsed Laser Ablation of Materials*, Phys. Rev. B **69**, 054102 (2004).

[60] J. F. Ready, *Effects due to Absorption of Laser Radiation*, J. Appl. Phys. **36**, 462 (1965).

[61] S. C. Wilks and W. L. Kruer, *Absorption of Ultrashort, Ultra-Intense Laser Light by Solid and Overdense Plasmas*, IEEE Jornal of Quantum Electronics **33**, 1954 (1997).

[62] H. M. Milchberg, R. R. Freeman, S. C. Davey and R. M. More, *Resistivity of a Simple Metal from Room Temperature to* 10^6 *K*, Phys. Rev. Lett. **61**, 2364 (1988).

[63] O. L. Landen, D. G. Stearns, and E. M. Campbell, *Measurement of the Expansion of Picosecond Laser-Produced Plasmas Using Resonance Absorption Profile Spectroscopy*, Phys. Rev. Lett. **63**, 1475 (1989).

[64] R. P. Godwin, *Absorption in Laser-Produced Plasma Experiments: A Personal View*, Appl. Opt. **18**, 3555 (1979).

[65] J. C. Kieffer, P. Audebert, M. Chaker, J. P. Matte, H. Pépin, T. W. Johnston, P. Maine, D. Meyerhofer, J. Delettrez, D. Strickland, P. Bado, G. Mourou, *Short-Pulse Laser Absorption in Very Steep Plasma Density Gradients*, Phys. Rev. Lett. **62**, 760 (1989).

[66] P. Mora, *Theoretical Model of Absorption of Laser Light by a Plasma*, Phys. Fluids **25**, 1051 (1982).

[67] R. Fedosejevs, R. Ottmann, R. Sigel, G. Kühnle, S. Szatmari and F. P. Schäfer, *Absorption of Femtosecond Laser Pulses in High-Density Plasma*, Phys. Rev. Lett. **64**, 1250 (1990).

[68] R. Fedosejevs, R. Ottmann, R. Sigel, G. Kühnle, S. Szatmari and F. P. Schäfer, *Absorption of Subpicoseconds Ultraviolet Laser Pulses in High-Density Plasma*, Appl. Phys. B **50**, 79 (1990).

[69] N. G. Denisov, *On a Singularity of the Field of an Electromagnetic Wave Propagated in an Inhomogeneous Plasma*, Sov. Phys. - JETP **4**, 544 (1957).

[70] V. L. Ginzburg, *The Properties of Electromagnetic Waves in Plasma*, Pergamon, New York (1964).

[71] W. L. Kruer, *The Physics of Laser Plasma Interactions*, Westview Press, Oxford (2003).

[72] P. Mulser, D. Bauer and H. Ruhl, *Collisionless Laser-Energy Conversion by Anharmonic Resonance*, Phys. Rev. Lett. **101**, 225002 (2008).

[73] H. K. Chung, W. L. Morgan and R. W. Lee, *FLYCHK: an Extension to the K-shell Spectroscopy Kinetics Model FLY*, J. Quant. Spectrosc. Radiat. Transf. **81**, 107 (2003).

[74] V. I. Berezhani and N. L. Shatashvili, *On the "Vacuum Heating" of Plasma in the Field of Circulary Polarized Laser Beam*, Europhys. Lett. **76**, 70 (2006).

[75] J. Dawson and C. Oberman, *High-Frequency Conductivity and the Emission and Absorption Coefficients of a Fully Ionized Plasma*, Phys. Fluids **5**, 517 (1962).

[76] F. Wooten, *Optical Properties of Solids*, Academic Press, New York (1972).

[77] Ya. B. Zel'dovich and Yu. P. Raizer, *Physics of Shock Waves and High-Temperature Hydrodynamic Phenomena*, edited by W. D. Hayes and R. F. Probstein, Dover Publications, New York (2002).

[78] http://www.fz-juelich.de/zam/files/splim.

[79] F. Brunel, *Not-So-Resonant, Resonant Absorption*, Phys. Rev. Lett. **59**, 52 (1987).

[80] S. Kato, B. Bhattacharyya, A. Nishiguchi and K. Mina *Wave Breaking and Absorption Efficiency for Short Pulse P-Polarized Laser Light in a Very Steep Density Gradient*, Phys. Fluids B **5**, 564 (1993).

[81] W. L. Kruer and K. Estabrook, $\vec{J} \times \vec{B}$ *Heating by Very Intense Laser Light*, Phys. Fluids **28**, 430 (1985).

[82] J. P. Freidberg, R. W. Mitchell, R. L. Morse and L. I. Rudsinski, *Resonant Absorption of Laser Light by Plasma Targets*, Phys. Rev. Lett. **28**, 795 (1972).

[83] P. Mulser, S. Pfalzner, and F. Cornolti, *Plasma Production with Intense Femtosecond Laser Pulses* in *Laser Interaction with Matter*, Ed. G. Velarde et al., World Scientific, Singapore, p. 142 (1989).

[84] P. Mulser, *Theory of Plasma Wave Absorption*, in *Laser Interaction with Atoms, Solids and Plasmas*, R. M. More (ed.), Plenum Press, New York, p. 383 (1994).

[85] P. Mulser and M. Kanapathipillai, *Collisionless Absorption in Clusters out of Linear Resonance*, Phys. Rev. A **71**, 063201 (2005).

[86] P. Gibbon and A. R. Bell, *Collisionless Absorption in Sharp-Edged Plasmas*, Phys. Rev. Lett. **68**, 1535 (1992).

[87] P. Gibbon, *Efficient Production of Fast Electron from Femtosecond Laser Interaction with Solid Targets*, Phys. Rev. Lett. **73**, 664 (1994).

[88] J. Denavit, *Absorption of High-Intensity Subpicoseconds Lasers on Solid Density Targets*, Phys. Rev. Lett. **69**, 3052 (1992).

[89] Q. L. Dong, J. Zhang and H. Teng, *Absorption of Femtosecond Laser Pulses in Interaction with Solid Targets*, Phys. Rev. E **64**, 026411 (2001).

[90] H. B. Cai, W. Yu, S. P. Zhu, C.-Y. Zheng, L.H. Cao and W.-B. Pei, *Vacuum Heating in the Interaction of Ultrashort, Relativistically Strong Laser Pulses with Solid Targets*, Phys. Plasmas **13**, 063108 (2006).

[91] H. B. Cai, W. Yu, S. P. Zhu and C.-Y. Zheng, *Short-Pulse Laser Absorption via $\vec{J} \times \vec{B}$ Heating in Ultrahigh Intensity Laser Plasma Interaction*, Phys. Plasmas **13**, 113105 (2006).

[92] D. Bauer and P. Mulser, *Vacuum Heating versus Skin Layer Absorption of Intense Femtosecond Laser Pulses* Phys. Plasmas **14**, 023301 (2007).

[93] P. J. Catto and R. M. More, *Sheath Inverse Bremsstrahlung in Laser Produced Plasmas*, Phys. Fluids **20**, 704 (1977).

[94] T.-Y. Brian Yang, William L. Kruer, Richard M. More, and A. Bruce Langdon, *Absorption of Laser Light in Overdense Plasmas by Sheath Inverse Bremsstrahlung*, Phys. Plasmas **8**, 3146 (1995).

[95] T.-Y. Brian Yang, William L. Kruer, A. Bruce Langdon and T. W. Johnston, *Mechanisms for Collisionless Absorption of Light Waves Obliquely Incident on Overdense Plasmas with Steep Density Gradients*, Phys. Plasmas **3**, 2702 (1996).

[96] E. S. Weibel, *Anomalous Skin Effect in a Plasma*, Phys. Fluids **10**, 741 (1967).

[97] W. Rozmus and V. T. Tikhonchuk, *Skin Effect and Interaction of Short Laser Pulses with Dense Plasmas*, Phys. Rev. A **42**, 7401 (1990).

[98] W. Rozmus and V. T. Tikhonchuk, *Heating of Solid Targets by Subpicosenconds Laser Pulses*, Phys. Rev. A **46**, 7811 (1992).

[99] A. A. Andreev, E. G. Gamalii, V. N. Novikov, A. N. Semakhin and V. T. Tikhonchuk, *Heating of a Dense Plasma by an Ultrashort Laser Pulse in the Anomalous Skin-Sffect Regime*, Sov. Phys. JETP **74**, 963 (1992).

[100] P. Kirkpatrick and A. V. Baez, *Formation of Optical Images by X-Rays*, J. Opt. Soc. Am. **38**, 766 (1948).

[101] A. G. Michette, *Optical Systems for Soft X Rays*, Plenum Press (New York) (1986).

[102] E. Jourdain, W. Biel, D. Lepère, J. Serre, A. Liard, A. Greiche and R. Burhenn, *VUV and Soft X-Ray Spectroscopy Using a Toroidal Grating Spectrograph* in *X-Ray Lasers*, Proceedings of the 10th International Conference, 517 (2006).

[103] http://www.jobinyvon.de - *The Optics of Spectroscopy* (tutorial).

[104] B. Hidding, *En Route: Elektronenbeschleuniger der nächsten Generation auf Laser-Plasma-Basis*, Dissertation, Heinrich-Heine-Universität, Düsseldorf (2008)

[105] H. Ruhl and P. Mulser, *Relativistic Vlasov Simulation of Intense fs Laser Pulse-Matter Interaction*, Phys. Rev. A **205**, 388 (1995).

[106] D. D. Meyerhofer, H. Cheq, J. A. Delettrez, B. Soom, S. Uchida, and B. Yaakobi, *Resonance Absorption in High-Intensity Contrast, Picosecond Laser-Plasma Interactions*, Phys. Fluids B **5**, 2584 (1993).

[107] C. T. Hansen, S. C. Wilks, and P. E. Young, *Spectral Evidence for Collisionless Absorption in Subpicosecond Laser-Solid Interactions*, Phys. Rev. Lett. **83**, 5019 (1999).

[108] M. K. Grimes, A. R. Rundquist, Y. S. Lee and M. C. Downer, *Experimental Identification of "Vacuum Heating" at Femtosecond-Laser-Irradiated Metal Surfaces*, Phys. Rev. Lett. **82**, 4010 (1999).

[109] U. Teubner, J. Bergmann, B. van Wonterghem, F. P. Schäfer, and R. Sauerbrey, *Angle-Dependent X-Ray Emission and Resonance Absorption in a Laser-Produced Plasma Generated by a High Intensity Ultrashort Pulse*, Phys. Rev. Lett. **70**, 794 (1993).

[110] M. Fraenkel, A. Zigler, Z. Henis, S. Eliezer, and N. E. Andreev, *Measurement of the Energy Penetration Depth into Solid Targets Irradiated by Ultrashort Laser Pulses*, Phys. Rev. E **61**, 1899 (2000).

[111] L. M. Chen, J. Zhang, Q. L. Dong, H. Teng, T. J. Liang, L. Z. Zhao, and Z. Y. Wei, *Hot Electron Generation via Vacuum Heating Process in Femtosecond Laser Solid Interactions*, Phys. Plasmas **8**, 2925 (2001).

[112] P. Gibbon, *Short Pulse Laser Interactions with Matter*, Imperial College Press, London (2005).

[113] A. B. Langdon, *Nonlinear Inverse Bremsstrahlung and Heated-Electron Distribution*, Phys. Rev. Lett. **44**, 575 (1980).

[114] M. Sherlock, A. R. Bell and W. Rozmus, *Absorption of Ultra-Short Laser Pulses and Particle Transport in Dense Targets*, Laser and Particule Beams **24**, 231 (2006).

[115] N. W. Ashcroft and N. D. Mermin, *Solid State Physics*, Saunders (1976).

[116] R. Sauerbrey, J. Fure, S. P. Le Blanc, B. van Worterghem, U. Teubner and F. P. Schäfer, *Reflectivity of Laser-Produced Plasmas Generated by a High Intensity Ultrashort Pulse*, Phys. Plasmas **1**, 1635 (1994).

[117] D. Strickland and G. Mourou, *Compression of Amplified Chirped Optical Pulses*, Op. Commun. **56**, 219 (1985).

[118] P. Maine, D. Strickland, D. Bado, M. Pessot and G. Mourou, *Generation of Ultrahigh Peak Power Pulses by Chirped-Pulse Amplification*, IEEE Journal of Quantum Electronics **24**, 389 (1988).

[119] P. F. Moulton, *Spectroscopic and Laser Characteristics of* $Ti - Al_2O_3$, J. Opt. Soc. Am. B- Optical Physics **3**, 125 (1986).

[120] O. Svelto, *Principles of Lasers* 4th ed., Plenum Press, New York (1998).

[121] A. E. Siegman, *Lasers*, University Science Book, Sausalito (1986).

[122] G. Prezler, Lecture notes

[123] T. Brabec, Ch. Spielmann, P. F. Curley and F. Krausz, *Kerr Lens Mode Locking*, Opt. Lett. **17**, 1292 (1992).

[124] D. E. Spence, P. N. Kean and W. Sibbett, *60-fsec Pulse Generation from a Self-Mode-Locked Ti:Sapphire Laser*, Opt. Lett. **16**, 42 (1991).

[125] C. Rulliere (Ed.), *Femtosecond Laser Pulses*, 2^{nd} Edition, Springer (2003).

[126] R. Szipöcs, K. Ferencz, C. Spielmann and F. Krausz, *Chirped Multilayer Coating for Broadband Dispersion Control in Femtosecond Lasers*, Opt. Lett. **19**, 201 (1994).

[127] A. Stingl, M. Lenzner, Ch. Spielmann, F. Krausz and R. Szipöcs, *Sub-10-fs Mirror-Dispersion-controlled Ti:Sapphire Laser,* Opt. Lett. **20**, 602 (1995).

[128] P. Tournois, *Acousto-Optic Programmable Dispersive Filter for Adaptive Compensation of Group Delay Time Dispersion in Laser Systems*, Opt. Commun. **140**, 245 (1997).

[129] M. Nisoli, S. DeSilvestri and O. Svelto, *Generation of High Energy 10 fs Pulses by a New Pulse Compression Technique*, Applied Physics Letters **68**, 2793 (1996).

[130] S. Sartania, Z. Cheng, M. Lenzner, G. Tempea, Ch. Spielmann, F. Krausz and K. Ferencz, *Generation of 0.1-TW 5-fs Optical Pulses at a 1-kHZ Repetition Rate*, Opt. Lett **2**, 1582 (1997).

[131] J. Etchepare, G. Grillon and A. Orszag, *Third Order Autocorrelation Study of Amplified Subpicosecond Laser Pulses*, IEEE Journal of Quantum Electronics **19**, 775 (1983).

[132] E. D. Hirleman and W. H. Stevenson, *Intensity Distribution Properties of a Gaussian Laser Beam Focus*, Applied Optics **17**, 3496 (1978).

[133] F. Brandl, *Elektronenbeschleunigung und Erzeugung von Röntgenstrahlung bei der Wechselwirkung hochintensiver few-cycle Laserpulse mit Festkörpern*, Dissertation, Heinrich-Heine-Universität Düsseldorf (2006).

[134] R. Jung, *Laser-Plasma Interaction with Ultra-Short Laser Pulses*, Dissertation, Heinrich-Heine-Universität Düsseldorf (2007).

[135] K. Eidmann, R. Rix, T. Schlegel and K. Witte, *Absorption of Intense High-Contrast sub-Picosecond Laser Pulses in Solid Targets*, Europhys. Lett. **55**, 334 (2001).

[136] D. F. Price, R. M. More, R. S. Walling, G. Guethlein, R. L. Shepherd, R. E. Stewart and W. E. Witte, *Absorption of Ultrashort Laser Pulses By Solid Targets Heated Rapidly to Temperatures 1-1000 eV*, Phys. Rev. Lett. **75**, 252 (1995).

[137] D. W. Forslund, J. M. Kindel, Kenneth Lee, E. L. Lindman, and R. L. Morse, *Theory and Simulation of Resonant Absorption in a Hot Plasma*, Phys. Rev. A **11**, 679 (1975).

[138] K. Estabrook and W. L. Kruer, *Properties of Resonantly Heated Electron Distributions*, Phys. Rev. Lett. **40**, 42 (1978).

[139] M. Borghesi, A. J. Mackinnon, R. Gaillard, O. Willi and D. Riley, *Absorption of Subpicosecond UV Laser Pulses During Interaction with Solid Targets*, Phys. Rev. E **60**, 7374 (1999).

[140] K. Eidmann, J. Meyer-ter-Vehn, T. Schlegel, S. Hüller, *Hydrodynamic Simulation of Subpicosecond Laser Interaction with Solid-Density Matter*, Phys. Rev. E **14**, 1202 (2000).

[141] Y. T. Lee and R. M. More, *An Electron Conductivity Model for Dense Plasmas*, Phys. Plasmas **27**, 1273 (1984).

[142] R. Ramis, R. Schmalz and J. Meyer-ter-Vehn, *Multi-a Computer Code for One-Dimensional Multigroup Radiation Hydrodynamics*, Computer Physics Communications **49**, 475 (1988).

[143] M. Cerchez, R. Jung, J. Osterholz, T. Toncian, O. Willi, P. Mulser and H. Ruhl, *Absorption of Ultrashort Laser Pulses in Strongly Overdense Targets*, Phys. Rev. Lett. **100**, 245001 (2008).

[144] J. Osterholz, F. Brandl, T. Fischer, D. Hemmers, M. Cerchez, G. Pretzler, O. Willi and R. J. Rose, *Production of Dense Plasmas with Sub-10-fs Laser Pulses*, Phys. Rev. Lett. **96**, 085002 (2006).

[145] J. Osterholz, F. Brandl, M. Cerchez, T. Fischer, D. Hemmers, B. Hidding, A. Pipahl, G. Pretzler, S. J. Rose, and O. Willi, *Extreme Ultraviolet Emission from Dense Plasmas Generated with sub-10-fs Laser Pulses*, Phys. Plasmas **15**, 103301 (2008).

[146] A. Zigler, P. G. Burkhalter, D. J. Nagel, M. D. Rosen, K. Boyer, G. Gibson, T. S. Luk, A. McPherson and C. K. Rhodes, *Measurement of Energy Penetration Depth of Subpicoseconds Laser Energy into Solid Density Matter*, Appl. Phys. Lett **59**, 534 (1991).

[147] D. R. Bach, D. E. Casperson, D. W. Forslund, S. J. Gitomer, P. D. Goldstone, A. Hauer, J. F. Kephart, J. M. Kindel, R. Kristal, G. A. Kyrala, K. B. Mitchell, D. B. van Hulsteyn, and A. H. Williams, *Intensity-Dependent*

Absorption in 10.6 μm *Laser-Illuminated Spheres*, Phys. Rev. Lett. **50**, 2082 (1983).

[148] H. Nishimura, K. Mima, Y. Yanase, N. Banjoya, H. Fujita, K. Iba, M. Matoba, S. Nakai and C. Yamanaka, *Resonance Absorption and Surface Instability at a Critical Density Surface of a Plasma Irradiated by a CO_2 Laser*, Phys. Plasmas **22**, 69 (1980).

[149] P. Beckmann and A. Spizzichino, *The Scattering of Ellectromangnetic Waves from Rough Surfaces*, Pergamon Press, Oxford (1970).

[150] J.J. Thomson, W.L. Kruer, A.B. Langdon, C.E. Max and W.C. Mead, *Theoretical Interpretation of Angle- and Polarization-Dependent Laser Light Absorption Measurements*, Phys. Fluids **21**, 707 (1978).

[151] R. A. Cairns *Resonance Absorption at a Rippled Critical Surface*, Phys. Plasmas **20**, 991 (1978).

[152] J. F. Young, J. E. Sipe, and H. M. van Driel, *Laser-Induced Periodic Surface Structure. III. Fluence Regimes, the Role of Feedback, and Details of the Induced Topography in Germanium*, Phys. Rev. B **30**, 2001 (1984).

[153] L. K. Ang, Y. Y. Lau, R. M. Gilgenbach, and H. L. Spindler, *Analysis of Laser Absorption on a Rough Metal Surface*, Appl. Phys. Lett. **70**, 696 (1997).

[154] T. Nishikawa, H. Nakano, N. Uesugi, M. Nakao and H. Masuda, *Greatly Enhanced Soft X-Ray Generation from Femtosecond-Laser-Produced Plasma by Using a Nanohole-Alumina Target*, Appl. Phys. Lett. **75**, 4079 (1999).

[155] P. P. Rajeev, S. Banerjee, A. S. Sandhu, R. C. Issac, L. C. Tribedi, and G. R. Kumar, *Role of Surface Roughness in Hard-X-Ray Emission from Femtosecond-Laser-Produced Copper Plasmas*, Phys. Rev. A **65**, 052903 (2002).

[156] P. P. Rajeev and G. R. Kumar, *Polarization Independent Hot Electron Production from Modulated Solid Surfaces*, Opt. Comm. **222**, 9 (2003).

[157] S. V. Bulanov and N. M. Naumova and F. Pegoraro, *Interaction of an Ultrashort, Relativistically Strong Laser with an Overdense Plasma*, Phys. Plasmas **1**, 745 (1993).

[158] A. Bergmann, S. Hüller, P. Mulser and H. Schnabl, *Resonance Absorption by Nonlinear Electron Plasma Waves*, Europhys. Lett. **14**, 661 (1991).

[159] R. Lichters, J. Meyer-ter-Vehn, and A. Pukhov, *Short-Pulse Laser Harmonics from Oscillating Plasma Surfaces Driven at Relativistic Intensity*, Phys. Plasmas **3**, 3425 (1996).

[160] M. V. Ammosov, N. B. Delone and V. P. Krainov, *Tunnel Ionization of Complex Atoms and of Atomic Ions in an Alternating Electromagnetic Field*, Sov. Phys. JETP Lett. **64**, 1191 (1986).

[161] H.-J. Kull, *Linear Mode Conversion in Laser Plasmas*, Phys. Plasmas **26**, 1881 (1983).

[162] M. Born and E. Wolf, *Principles of Optics*, fourth edition, Pergamon Press, Oxford (1970).

[163] M. Kundu, *Energy Absorption, Ionization, and Harmonic Emission in Laser-Irradiated Atomic Clusters*, Dissertation, University of Heidelberg (2007).

[164] A. Horn, *Zeitaufgelöste Analyse der Wechselwirkung von ultrakurz gepulster Laserstrahlung mit Dielektrika*, Dissertation, Rheinisch-Westfälischen Technischen Hochschule Aachen (2003).

Acknowledgement

There are many people who supported me during these years. I thank them all.

Prof. Oswald Willi gave me this great chance to work in his group and entrusted me from the very beginning with this unequivocally interesting project. I take this opportunity to express my gratitude for his careful supervision doubled by his endless moral support when the burden seemed too heavy. His vast knowledge and experience in the field helped keeping the balance on the thin line between self made luck and hard work. I am also grateful to Prof. Peter Mulser for inspiring me with thoughtful suggestions. He was a source of knowledge of inestimable importance for this thesis by shedding a new light on the interpretation of the results. I wish to thank Prof. Georg Pretzler for his constant interest and good will for my work. I would also like to thank Prof. Hartmut Ruhl for his support in the numerical simulations performed for this thesis and for valuable discussions.

I am grateful to Jens Osterholz for his continuous scientific support, patience and for creative collaboration. We shared many ideas and our discussions revealed both solutions and new problems. My colleagues Ralph Jung and Toma Toncian were careful guides in my initiation in the secrets of simulation of the plasma processes. The discussions we had were always helpful. Their effort and kind support are highly appreciated.

I would like to acknowledge the support and useful knowledge I received from Dirk Hemmers in operating the laser system during the experiments. I thank also Christoph Bolten, Helmut Borrmann for their excellent technical assistance. The kind support of the mechanical workshop team in the experimental setups is acknowledged. I would like to address special thanks to Mr. Manfred Rosemann for his kindness and his technical solutions which were similar to those of a chess player; always saw two moves in advance. He was also my first unofficial German language teacher in the group.

Renate ter Horst and Claudia Dingle were always there to help through the never-ending bureaucratic documents that are sometimes hard to understand by Physicists. They have opened their hearts and their doors, supplying me always with a little extra-energy in rainy days.

Last but not least I would like to thank my family and my friends for being there for me. Mihai, your encouragement and patience sustained me over all these years to go further.

I dedicate this thesis to my son Andrei. It took almost half of his life.

Die hier vorgelegte Dissertation habe ich eigenständig und ohne unerlaubte Hilfe angefertigt. Die Dissertation wurde in der vorgelegten oder in ähnlicher Form noch bei keiner anderen Institution eingereicht. Ich habe bisher keine erfolglosen Promotionsversuche unternommen.

Düsseldorf, 15.12.2008

(Mirela Cerchez)